November 2016

Eulerian CFD Modeling of Multiphase Internal Injector Flow and External Sprays

Eli T. Baldwin
University of Massachusetts - Amherst

EULERIAN CFD MODELING OF MULTIPHASE INTERNAL INJECTOR FLOW AND EXTERNAL SPRAYS

A Dissertation Presented

by

ELI T. BALDWIN

Submitted to the Graduate School of the
University of Massachusetts Amherst in partial fulfillment
of the requirements for the degree of

DOCTOR OF PHILOSOPHY

September 2016

Mechanical and Industrial Engineering

EULERIAN CFD MODELING OF MULTIPHASE INTERNAL INJECTOR FLOW AND EXTERNAL SPRAYS

A Dissertation Presented

by

ELI T. BALDWIN

Approved as to style and content by:

David P. Schmidt, Chair

Blair Perot, Member

Michael Henson, Member

Sundar Krishnamurty, Department Head
Mechanical and Industrial Engineering

ACKNOWLEDGMENTS

First, I would like to thank my advisor, Professor David Schmidt. His passion for teaching and his care for students is evident in the way he conducts himself. Over the course of my dissertation, he provided me with a wonderful balance of both freedom and guidance. He also went out of his way to ensure that my work would remain constantly and adequately funded. I am thankful for Professor Blair Perot whom I had as an instructor for turbulence and computational fluid dynamics. These classes helped provide me with a strong foundational understanding on which I conducted my research. I would also like to acknowledge and thank Professor Mike Henson, as well as Professor Perot for serving on my committee.

I would like to thank my wife. Her friendship and companionship has been a constant source of rest, and her work in the home has allowed for me to better focus my energies on research. She is a blessing and I love her with all my heart. I am thankful for my children, whom I love so dearly. Watching them learn, laugh, and delight in the world brings me unexplainable joy. I am also thankful for my parents and sisters, who have been a constant source of wisdom, love, and encouragement.

Additionally, I am thankful for the support of many fellow students over the years, including Maija, Kyle, Maryam, Brad, Michael, Pavan, Barnali, Nate, and Sampath. Much assistance was provided by many of you in helping me get acquainted with OpenFOAM. In the midst of hours on end of running cases and debugging code, there was often a good sense of comradery found in the lab, and it was never hard to find someone willing to take a break to talk about something unrelated to work.

Finally, I would like to acknowledge the financial support provided by General Motors, as well as the financial support from the Spray Combustion Consortium coordinated by Sandia National Lab.

ABSTRACT

EULERIAN CFD MODELING OF MULTIPHASE INTERNAL INJECTOR FLOW AND EXTERNAL SPRAYS

SEPTEMBER 2016

ELI T. BALDWIN

B.S., UNIVERSITY OF MASSACHUSETTS AMHERST

M.S., UNIVERSITY OF WASHINGTON SEATTLE

Ph.D., UNIVERSITY OF MASSACHUSETTS AMHERST

Directed by: Professor David P. Schmidt

The improvement of combustion systems which use sprays to atomize liquid fuel requires an understanding of that atomization process. Although the secondary break up mechanisms for the far-field of an atomizing spray have been thoroughly studied and well understood for some time, understanding the internal nozzle flow and primary atomization on which the far-field spray depends has proven to be more of a challenge. Flow through fuel injector nozzles can be highly complex and heavily influenced by factors such as turbulence, needle motion, nozzle imperfections, nozzle asymmetry, and phase change. All of this occurs within metallic injectors, making experimental characterization challenging.

A review of computational studies in literature shows a trend towards engineering models based on the Eulerian description of the fluid, rather than the Lagrangian.

With this approach, the internal and external flow can be simulated together. This allows for the influence of nozzle geometry on the spray to be captured.

Developments and advancements applicable to these Eulerian solvers are discussed. This includes a new constraint on the turbulent mixing model, as well as the inclusion of a vaporization model and a non-equilibrium phase change model. Additionally, issues regarding thermodynamic and hydrodynamic consistency of compressible flows using a segregated solution approach are addressed, as are issues regarding dynamic mesh motion in a compressible solver. Finally, an efficient way of accounting for high pressure thermodynamic properties is presented.

Applied case studies of diesel direct injection are then described. The single-field Eulerian approach is shown to perform very well at the high Reynolds and Weber numbers present in diesel DI conditions, capturing spray characteristics such as density distribution, penetration, and velocity profiles with a moderate level of accuracy. While transient needle motion is shown to cause interesting internal flow features, in converging, axisymmetric diesel DI nozzles, modeling of the internal flow is shown to only marginally benefit the solution.

Finally, applied case studies of gasoline direct injection are presented, first with a parameter study varying counterbore depth, pressure drop, and the P_a/P_s ratio. The significant influence of flash-boiling under a low P_a/P_s is shown. Next, a detailed analysis of internal nozzle and near-field flow in flashing and non-flashing multi-hole injection is presented. Excellent agreement to experimental rate of injection is achieved with transient needle motion and qualitative agreement to experimental imaging in the near-field is shown. Complex internal nozzle flow is analyzed and shown to result in string flash-boiling, perturbations and expansions of the spray angle, and oscillation in the ROI.

Single-field multiphase Eulerian modeling is a useful tool for understanding and designing DI atomizers. The next generation of spray models will rely heavily on this

approach to better understand and predict the influence of internal and near-field flow on the combustion system.

CONTENTS

LIST OF TABLES

Table **Page**

LIST OF FIGURES

Figure **Page**

CHAPTER 1

INTRODUCTION

1.1 Background

In a world with a finite supply of fossil fuels and a growing concern over pollution and climate change, there is great interest in developing cleaner and more efficient means of power generation. Globally, liquid fuels account for around 34% of the world's energy consumption [195]. This is the largest single source of energy and the U.S. Energy Information Administration predicts it will continue to dominate until as far out as 2040. Of this 34%, over half is consumed in the transportation sector by internal combustion engines [195].

Although these engines have undergone over a century of development, there is still a lot of work to be done. Operating under ideal loading conditions, the efficiency of a modern gasoline engine is around 30% and that of a modern diesel engine is around 40% [190]. Under typical real world loading conditions, their overall efficiencies are much lower. In addition to this, the problem of nitrogen oxides (NOx), unburned hydrocarbons (UHC), soot, and carbon monoxide (CO) emissions persists, especially for direct injection (DI) engines. As the cost of liquid fuel continues to climb and emissions and fuel economy regulations continue to tighten, automakers are working hard to develop cleaner and more efficient engines.

This effort is centered around the design of the combustion system. An important step in such a design is understanding the precise distribution and characteristics of fuel and air in the chamber throughout the combustion cycle. This is especially true in DI engines where the atomization of the fuel plays a critical role in the combustion

process. Unfortunately, it is very difficult to experimentally obtain an accurate three-dimensional characterization of the combustion chamber because the spray is optically dense, length scales are small (injector diameters can be less than 100 μm), time scales are short (at 6000 rpm, one stroke takes only 5 ms), temperatures and pressures are high (300 MPa injection into a 6 MPa, 900 K chamber for a diesel DI), and geometries are complex (multiple valves per cylinder, multi-hole injectors, swirling inlet flow, piston heads with swirl cavities for GDI engines). For this reason, computational fluid dynamics (CFD) has become an important step in engine design.

1.2 Computational Fluid Dynamics

CFD is the numerical simulation of systems involving fluid flow, heat transfer, and/or chemical reactions. These systems are all governed by fundamental laws such as the conservation of mass, energy, and momentum which can be described by partial differential equations. Due to the non-linear nature of these equations and the size of the systems in question, analytical solutions are almost always unattainable. However, computers are capable of producing a numerical solution by discretizing the domain, linearizing the governing partial differential equations, and solving for the evolution of the system with the appropriate numerical methods.

Over the past few decades, CFD has developed into a large field that reaches across many industries. In the automotive industry, CFD is extensively used for analyzing exterior aerodynamics, internal climate control, heat management in the engine, internal nozzle flow, spray development, and combustion modeling of the fuel in the cylinder.

1.3 Direct Fuel Injection in Internal Combustion Engines

Two of the promising technologies to which automakers are turning to meet these demands are DI diesel and GDI engines. As both of these technologies utilize common

rail direct injection and both face the challenge of the combustion of a stratified fuel spray, there is significant overlap in the challenges facing their future development.

1.3.1 The Diesel Engine

The diesel engine is an internal combustion engine that uses the heat generated during the compression stroke to ignite its fuel. Fuel injection occurs late in the compression stroke, just before the cylinder reaches top dead center. This means that pre-ignition of the fuel is not an issue and compression ratios can be higher. The high compression ratio increases the temperature of the gas in the cylinder beyond the autoignition point of the fuel, causing the fuel to spontaneously ignite upon injection.

The higher compression ratio also increases the theoretical peak efficiency of the cycle. This is because it allows for the same combustion temperature to be reached with less fuel, while at the same time giving a longer expansion cycle through which work is done. This longer expansion cycle results in lower exhaust temperatures and thus less energy wasted as heat. Automotive diesel engines have thermal efficiencies in the range of 40% and low speed industrial diesels can have thermal efficiencies that exceed 50% [114, 190].

One of the big challenges in designing diesel engines is making a combustion system that will thoroughly and properly burn the injected fuel. As the stratified charge of diesel fuel mixes with the air and burns in the cylinder, there are inherently non-uniform combustion conditions across the charge. For instance, the outer regions can burn hot and lean, producing NOx emissions, and the inner core can burn rich, producing soot emissions. These problems are especially significant in older diesel engines that still use indirect injection [5].

Thankfully, significant progress has been made in fuel injection technology which has dramatically increased the cleanliness of diesel engines. The most notable innovation in fuel injection technology is common rail direct fuel injection [5], in which

a high-pressure fuel rail feeds individual valves. Modern third-generation systems feature precise piezoelectric valve actuation and very high injection pressures, with some systems reaching 300 MPa [92]. This enhances fuel atomization and allows for flexibility in operation over a range of engine loads and speeds. As a result, the modern diesel is both relatively clean and highly efficient, and its adoption by the automotive industry is vast. Diesel engines account for roughly 50% of the European car market and a continually increasing share of the U.S. market [205].

1.3.2 Gasoline Direct Injection Engine

A GDI engine is a spark ignited, direct injection engine that operates in multiple distinct combustion modes. Under moderate to high loading conditions, fuel is injected during air intake to a stoichiometric or near stoichiometric ratio. Mixing then occurs throughout the intake and compression strokes, generating a relatively homogeneous charge and combustion behavior similar to that of a traditional port fuel injection (PFI) gasoline engine. Under low load conditions, some GDI engines operate in a mode in which injection occurs near the end of the compression stroke. In this mode, a stratified charge of fuel burns in a localized region near the spark plug. This means that the overall mixture can be ultra lean and the need for throttling the air intake is reduced or negated altogether. This reduces fuel consumption during idle by almost 40% [157].

GDI technology is promising and gaining significant traction. When the second generation Ford EcoBoost GDI engine was launched in 2009, it boasted a 20% increase in fuel economy [82]. Moreover, the technology has already been implemented in numerous production vehicles made by more than a dozen different automakers. Many in the automotive industry expect it to be adopted as the new standard for gasoline internal combustion engines [13, 112, 169].

1.4 Overview of This Work

The focus of this dissertation is the use of single-field Eulerian CFD modeling to better understand multiphase internal nozzle and external sprays in direct injection engines. It consists of a literature review and analysis of relevant works in the field, a detailed description of the Eulerian modeling approach taken, and an in-depth analysis of both diesel DI and GDI systems.

Chapter 2 of this work concerns the characteristics of sprays, starting with a description of relevant dimensionless numbers and nozzle coefficients. Spray regimes are then defined and described, followed by a detailed description of the regions of a typical atomizing spray.

Next, in chapter 3, popular and promising experimental techniques are summarized and common experimental observations are reviewed. Experimental techniques related to fuel injection and sprays have come a long way in the past ten years and their work is an important piece of understanding DI sprays.

Chapter 4 concerns computational approaches to multiphase modeling, beginning with a description of high-fidelity, sharp interface methods. This includes direct numerical simulation (DNS) and large eddy simulation (LES) approaches and the popular multiphase modeling methods required to resolve a sharp interface. Next, various statistical and phenomenological modeling approaches are described, including Lagrangian-Eulerian, Eulerian-Eulerian, Eulerian Quadrature-Based Moment Models, and finally the single-field diffuse interface Eulerian approach.

Chapter 5 covers developments and advancements made for single-field diffuse interface Eulerian modeling. A new constraint on the turbulent mixing model commonly used in this approach is presented, and the inclusion of a local homogeneous flow vaporization model and a non-equilibrium flash-boiling/cavitation model is described.

Then, in chapter 6, several diesel injection case studies are described. This consists of both published in-progress work, external only, as well as coupled internal/external simulations.

An in-depth study on the internal and near-field flow of flashing and non-flashing GDI injection is covered in chapter 7. This includes multiple simulations on the 8 hole ECN spray G target nozzle as well as a parameter study conducted on 2D axisymmetric nozzles.

Finally, in chapter 8, conclusions are made regarding single-field diffuse interface multiphase Eulerian modeling for direct injection atomizers.

CHAPTER 2

CHARACTERISTICS OF SPRAYS

2.1 Dimensionless Numbers

The fluid flow involved in the atomization of a spray can be characterized by a variety of dimensionless numbers. These numbers compare various effects, timescales, and pressures that influence the behavior of the flow, and they are useful in predicting and understanding the behavior of the spray.

2.1.1 Reynolds Number

The most common dimensionless number in fluid dynamics is the Reynolds number. Reynolds number is the ratio of the inertial effects over the viscous effects. There are a variety of ways to calculate the Reynolds number, but the most common is

$$Re = \frac{\rho U L}{\mu} \sim \frac{\text{inertial effects}}{\text{viscous effects}} \tag{2.1}$$

where ρ is the density of the fluid, U is the velocity of the fluid, L is the characteristic length of the flow, and μ is the dynamic viscosity of the fluid. In high Reynolds number flows, the inertial effects are much larger than the viscous effects. Practically, this means that convection dominates. Conversely, in low Reynolds number flows, viscous effects are greater, which causes diffusion to dominate. Because diffusion is a smoothing phenomenon, low Reynolds number flows are laminar and high Reynolds number flows are turbulent.

2.1.2 Weber Number

The Weber number is the ratio between inertial effects and surface tension effects. It is commonly defined as

$$We = \frac{\rho U^2 L}{\sigma} = \frac{\rho U^2}{\sigma / L} \sim \frac{\text{inertial effects}}{\text{surface tension effects}} \tag{2.2}$$

where σ is the surface tension of the flow. Surface tension effects work to minimize the surface area of the flow. In a liquid jet or a liquid ligament moving through the air, this means resisting the stretching of surfaces that results from aerodynamic forces and working to pull the liquid into spherical shapes where surface area is minimized. High Weber number flows break apart quickly and into small droplets. As the flow breaks apart, the characteristic length decreases, thus lowering the Weber number of the flow. When the Weber number is low enough ($We < 6$), surface tension effects tend to be strong enough to hold the droplets together [200].

2.1.3 Stokes Number

The Stokes number is a dimensionless number that can be applied to multiphase flow in which one phase is continuous and the other is suspended as bubbles, droplets, or particles. It is defined as the ratio of the characteristic time of the suspended bubble (or droplet or particle) to the characteristic time of the continuous phase, or

$$Stk = \frac{\tau_0 u_0}{l_0} \tag{2.3}$$

where τ_0 is the relaxation time of the bubble, suspended particle, or droplet, u_0 is the velocity of the flow, and l_0 is the characteristic length of the flow (typically diameter).

In flows with low Stokes numbers, the disperse phase is able to quickly relax to the velocity of the surrounding fluid, essentially following fluid streamlines. In high Stokes number flows, the disperse phase inertia dominates, allowing for this phase to continue on its initial trajectory.

2.1.4 Mach Number

In the context of nozzle flow and atomizing sprays, the Mach number represents the ratio of the speed of a fluid flow to the local speed of sound.

$$Ma = \frac{U_{flow}}{U_{sound}} \tag{2.4}$$

Because the speed of sound is the speed at which pressure waves propagate through the fluid, the Mach number can be used to determine whether or not a flow can be considered incompressible. At $Ma < 0.1$-0.3 flow can be considered incompressible [206], and as the Mach number increases, compressibility effects become more and more pronounced.

Diesel injection speeds can be as high as 400-600 m/s. The speed of sound is around 1400 m/s in diesel fuel and 650 m/s in 900 K air. Under these conditions, compressibility effects are present and must be considered. Furthermore, due to the compressibility effect of a gas in a liquid, the speed of sound in a multiphase mixture can be dramatically lower than the speed of sound for either independent fluid [95]. Because of this, supersonic effects may need to be accounted for, especially in cavitating or flash-boiling nozzles where the injected flow can be considered a multiphase mixture of vapor and liquid fuel.

2.1.5 Cavitation Number

The cavitation number is often used in injection studies to understand the propensity for cavitation in nozzle flow. The definition below was suggested by Hoehn et al. [73] and discussed in the cavitation study by Nurick [131].

$$K_{cav} = \frac{P_1 - P_v}{P_1 - P_2} \tag{2.5}$$

Here P_1 is the upstream pressure, P_2 is the pressure at the nozzle exit, and P_v is the vapor pressure of the fluid. As can be seen in Eqn. 2.5, K_{cav} increases with decreased

inlet pressure or with increased outlet pressure. Nurick observed that for cylindrical nozzles with a sharp orifice cavitation occurs when $K_{cav} < K_{crit}$, where $K_{crit} \sim 1.7$ [131].

This form of the cavitation number is derived through one dimensional flow theory on a cavitating nozzle. There are other formulations for cavitation numbers, for instance those formulated by Sou et al. [181] which seek to account for the influence of the nozzle geometry on cavitation inception.

2.1.6 Jakob Number

Vaporization takes place at small length scales and is influenced by the complex interfacial and turbulent dynamics of the flow. Moreover, phase change occurs at different rates depending on the properties of the flow. The vapor pressure and vapor density of a cold fluid is typically very low. Because of this, very little heat transfer is required per volume of vapor, and cavitation, which occurs at low temperatures, is a fast, inertially driven process which tends to be near thermodynamic equilibrium. On the other hand, the vapor density of a hot liquid is much higher. Consequently, more heat transfer is required per volume of vapor and flash-boiling is a thermally driven non-equilibrium process.

This can be understood further with the help of the non-dimensional Jakob number which is the ratio of the sensible heat available to the latent heat required for vaporization [127].

$$Ja = \frac{\rho_l C_p \Delta T}{\rho_v h_{fg}} \tag{2.6}$$

Here ρ_l is the liquid density, ρ_v is the vapor density, C_p is the specific heat at constant pressure, ΔT is the degree of superheat, and h_{fg} is the enthalpy of vaporization. When the Jakob number is high there will be an abundance of energy available in the liquid to generate vapor. This means that heat transfer time scales will be much smaller than flow time scales and it can be assumed that the flow is at thermal equilibrium.

Alternatively, when the Jakob number is low, heat transfer time scales will be of the same order as that of the flow and thermal equilibrium cannot be assumed.

2.2 Nozzle Coefficients

Nozzles are frequently characterized by a variety of coefficients. As in the work by Desantes et al. [37], these coefficients are obtained through experimental measurements of nozzle diameter, mass flux, momentum flux, injection pressures, and some simple fluid dynamics calculations involving Bernoulli's equation. Mass flux can be measured through an injection rate meter and momentum flux through a spray force test rig. These commonly used nozzle coefficients will be defined and described below.

2.2.1 Coefficient of Discharge

The coefficient of discharge is defined as the actual mass flow rate over the theoretical mass flow rate of an ideal nozzle. It can be derived through

$$C_d = \frac{\dot{m}_{actual}}{\dot{m}_{ideal}} = \frac{\dot{m}_{actual}}{A\sqrt{2\rho_l \Delta P}} \tag{2.7}$$

where $\dot{m}_{actual}$ is the measured mass flux and $A\sqrt{2\rho_\Delta P}$ is the theoretical mass flux obtained through the incompressible Bernoulli's equation. When dealing with compressible liquids, it is common to simply use the downstream density in conjunction with Eqn. 2.7. A more accurate formulation is shown in Eqn. 2.8, where the ideal mass flow rate is based upon a compressible conservation of energy analysis.

$$C_{d\ compressible} = \frac{\dot{m}_{actual}}{\dot{m}_{ideal}} = \frac{\dot{m}_{actual}}{A\rho_2\sqrt{2(\frac{P_1}{\rho_1} - \frac{P_2}{\rho_2})}} \tag{2.8}$$

Losses that drive the C_d below 1 are caused by a smaller effective exit area and/or a lower than ideal exit velocity. These losses can be captured by C_a and C_v, defined below, with the formulation $C_d = C_a \cdot C_v$.

2.2.2 Coefficient of Velocity

The coefficient of velocity is defined as

$$C_v = \frac{U_{actual}}{U_{ideal}} \tag{2.9}$$

where U_{actual} is the effective average exit velocity, which is calculated by the measured momentum flux divided by the measured mass flux, $U_{actual} = \dot{M}/\dot{m}$, and U_{ideal} is the Bernoulli velocity. Values of C_v which are less than unity are the result of viscous dissipation of energy as well as anything that may have redirected the exiting fluid to a direction that is not aligned with the mean flow. This redirection of flow could occur due to turbulent eddies, nozzle imperfections, and/or swirling nozzle flow.

2.2.3 Coefficient of Area

The coefficient of area is calculated using the following relationship:

$$C_a = C_d/C_v \tag{2.10}$$

and thus captures any losses which have occurred that were not accounted for by the velocity coefficient. These losses are typically related to vapor formation within the nozzle through cavitation or flash-boiling which reduce the effective exit area of the nozzle.

Because turbulence encourages momentum transfer across velocity gradients resulting in close to uniform average velocity profiles, this parameter can be used to characterize the turbulence intensity in a nozzle [147]. Fully developed turbulence yields a C_a close to 1, and as turbulence decreases so does C_a.

2.2.4 Contraction Coefficient

The contraction coefficient is defined as

$$C_c = \frac{A_c}{A} \tag{2.11}$$

where A_c is liquid area at the vena contracta of a cavitating nozzle. This coefficient depends only on the nozzle geometry. Following the one dimensional flow theory from Nurick [131], the C_d can be described in terms of the C_c and K_{cav}, as $C_d = C_c \cdot \sqrt{K_{cav}}$.

2.3 Spray Regimes

There are multiple spray regimens that are characterized by different break up mechanisms. This work is primarily concerned with the atomization regime, as this is the regime of direct injection sprays, however, the other regimes are listed and briefly described below. Images of the different breakup regimes can be seen in Fig. 2.1. A more thorough description can be found in [51]. In order of increasing Reynolds and Weber number, the spray regimes are as follows:

1. Non-jetting or drip regime: Here the flow rate is low and the $We < 3 - 4$; surface tension dominates and drops are immediately formed.

2. Rayleigh breakup: Here the interaction between surface tension and liquid inertia yields consistent drops of a diameter slightly larger than the nozzle.

3. First wind-induced breakup: Here helical or twisting instabilities on the liquid jet result in breakup with drops primarily the size of the diameter with some drops that are significantly smaller.

4. Second wind-induced breakup: Here surface instabilities and helical and twisting instabilities result in faster breakup with a wider range of drop size.

5. Atomization breakup: Here breakup begins right at the nozzle exit and final drop sizes are much smaller than the nozzle diameter.

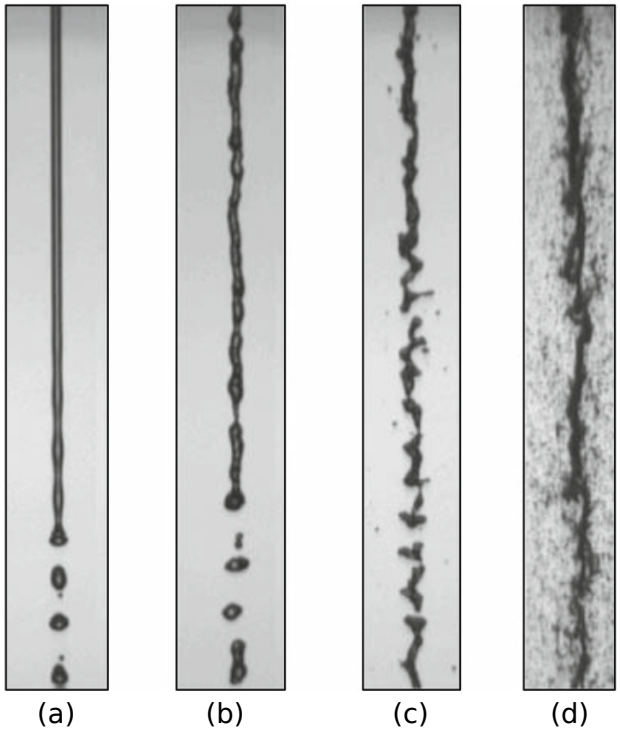

Figure 2.1: Cylindrical jet spray regimes. (a) Rayleigh regime at Re=790 We=0.06. (b) first wind-induced regime at Re=5,500 We=2.7. (c) second wind-induced regime at Re=16,500 We=24. (d) atomization regime at Re=28,000 We=70. Images from [104].

2.4 Regions of The Spray

An atomizing spray is typically described by two regions. These can be seen in Fig. 2.2.

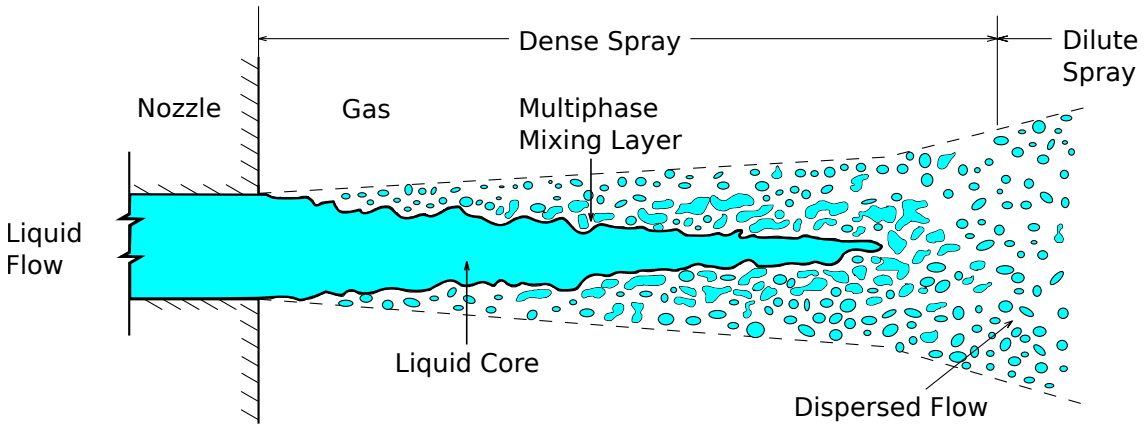

Figure 2.2: The spray regions of an atomizing jet. Adapted from [54].

2.4.1 Dense Spray Region

The first region is close to the nozzle and is described in literature as the dense spray region, the near-field region, or the spray formation region. As can be seen in Fig. 2.2, the dense spray region consists of a liquid core which protrudes from the nozzle and is surrounded by a complex multiphase mixing layer. In the mixing layer, liquid structures are broken apart from the liquid core. This process is called primary breakup. These liquid structures then undergo secondary breakup when they break into ligaments and drops. Outside of the multiphase mixing layer is a dispersed flow where liquid droplets are spread out and the liquid volume fraction is low.

2.4.2 Dilute Spray Region

The second region is known as the dilute spray region, or the far-field. Here the spray has completed the primary break up process and consists only of liquid ligaments and droplets, which will continue to undergo secondary breakup until they reach a size where the droplet Weber number is low enough ($We < 6$ [200]) that the surface tension forces can resist the aerodynamic forces. If conditions permit, the majority of fuel vaporization will occur in the dilute spray region as the surface area to volume ratio is highest there.

2.4.3 A Gap in Knowledge

The liquid in the dilute spray region is spread out and easy to observe. For this reason, it has been studied and well understood for quite some time [54]. Conversely, internal nozzle flow and flow in the dense spray region are hard to experimentally observe. Without understanding the flow in these regions, it is hard to develop predictive spray models. This is evidenced by the popular Lagrangian-Eulerian (LE) models that do a good job predicting secondary atomization and droplet motion, but struggle to handle the dense region. This has meant that accurate implementations of LE models require careful tuning of inputs like droplet size and velocity distribution [42].

This gap in knowledge has caused a significant amount of research effort to be focused on understanding flow within the nozzle and the dense spray region, and progress is being made. In the past 15 years, several new experimental techniques have emerged. Furthermore, many developments have been made in CFD modeling that have illuminated much of what occurs in these regions and are now allowing for a more fully-predictive modeling of the entire spray evolution, from the inlet of the injector to the edge of the vapor dome.

CHAPTER 3

EXPERIMENTAL CHARACTERIZATION

In this next chapter, a variety of useful experimental techniques as well as their contributions to understanding spray atomization will be described. While the selection of techniques is by no means exhaustive, it covers many that are commonly used as well as some new methods that show promise for future use.

3.1 Experimental Techniques

3.1.1 Shadowgraphy

Shadowgraphy is an optical method where the shadow of an object or flow is imaged. Because the index of refraction can vary within a fluid and between different transparent fluids, this method captures characteristics of the flow that cannot directly be seen. For instance, the shadow cast from hot air rising from a fire contains fluid flow patterns generated by the refraction of light through the variable density circulating air.

Due to its simplicity and effectiveness, this technique has been widely used in spray characterization. Shadowgram images generated through this technique can be used to observe general characteristics of the spray and to measure spray angle and liquid penetration. The technique, however, is limited to low optical densities. It is, therefore, not effective at capturing flow behavior inside the dense spray region. An example of a shadowgram can be seen in Fig. 3.2.

3.1.2 Schlieren Imaging

Schlieren imaging is very similar to shadowgraphy, with two distinct differences. First, the light is focused in a way that the object plane is mapped to the image plane. This allows for a more precise image to be captured and it also increases the sensitivity of the image to variation in the index of refraction, n; where shadowgraphy can capture variance in the second spatial derivative of n, schlieren imaging can see the first spatial derivative of n. Secondly, a large amount of background light is filtered out using a knife edge. This allows for an increase in the contrast ratio of the image.

Schlieren imaging is also widely used to characterize sprays. While being effective for capturing liquid penetration and spray angle, the increased sensitivity to variation in n also allows it to more effectively capture vapor penetration and shock patterns. Like shadowgraphy, this technique is also limited to the observation of low optical density flows. An example of a schlieren image can be seen in Fig. 3.1.

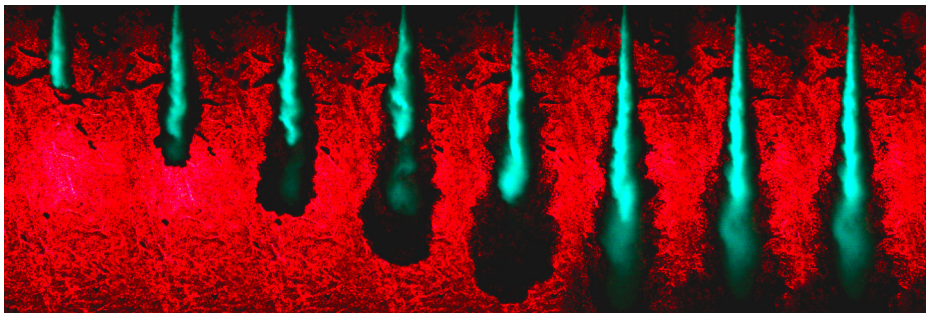

Figure 3.1: Schlieren-Streulicht image of evaporating diesel injection. Liquid fuel seen in cyan and fuel vapor seen as black. Image from [56].

3.1.3 Structured Light Surface Profilometry

When a structured light (for instance a pattern of parallel stripes) is projected onto a 3D object, the structured pattern will appear distorted from perspectives other than that of the projector. Images of the object taken from different perspectives can then be used to generate an exact geometric reconstruction of the surface profile. This

is a well understood technique that has a variety of applications including object recognition, 3D map building, biometrics, and clothing design [163].

In diesel injection, where the near-field spray is surrounded by a dense cloud of small liquid droplets, this technique would not be effective. However, in impinging sprays, where two jets collide to form an unstable atomizing liquid sheet, it has been implemented. This was done in 2013 by Halls et al. [68], producing an accurate representation of the liquid sheet.

3.1.4 Ballistic Imaging

Originally developed for the medical community, this is a line-of-sight technique where a laser is passed through the spray. Uncorrupted photons that have not been scattered (ballistic photons) are then detected on the far side, essentially generating a shadowgram of liquid structures. Ballistic imaging works for higher optical densities than shadowgraphy or schlieren imaging, penetrating the droplet cloud surrounding the core and allowing for effective imaging of the liquid/gas interface. Multiple BI images can be captured in rapid succession allowing for the characterization of interface velocity [170, 171]. For a detailed description of BI, read the work of Linne, [109, 110].

This technique has been used in the study of the primary breakup of a turbulent water jet [136], a laminar jet of water in the cross-flow of air [105, 107], a rocket injector [63, 168], and an atomizing diesel spray into air at a range of pressures from 0.1-6 MPa [55, 77, 106, 110, 139]. In these experiments ballistic imaging was primarily used to characterize the liquid/gas interface, producing surface wave amplitude and wavelength measurements, and void and ligament size distributions. It has also been used to observe diesel injection into elevated ambient density conditions at a variety of temperatures, with two resulting images seen in Fig. 3.7.

3.1.5 Structured Laser Illumination Planar Imaging

In traditional laser planar imaging, a single planar laser illuminates the spray and photons make their way from the laser to the imaging camera, typically located orthogonal to the laser plane, through Mie scattering off of the liquid droplets in the flow. Some photons, however, scatter off of multiple droplets before making their way to the camera. This adds noise to the image because the multiple scattered photons do not directly originate from the viewing plane. In structured laser illumination planar imaging (SLIPI) three laser sheets with a characteristic grid structure, each offset from the next by a spatial phase, are passed through the spray and imaged with a camera. The grid structure of the laser image and the presence of multiple images allow for most multiply scattered photons to be filtered out with image processing. For a more thorough description see the PhD thesis of Kristensson [94].

The resulting image from this technique produces a good cross sectional depiction of the droplets in the spray. This method can be used to produce a quantitative characterization of droplet size distribution across a plane in the dilute spray region [66]. Unfortunately, because the image processing assumes light has been scattered by spherical droplets, this method cannot produce quantitative results in the dense spray region.

3.1.6 Optical Connectivity

In optical connectivity, a florescent dye is added to the injected fluid and a laser is guided through the injector to illuminate the exiting liquid. The index of refraction of the liquid is higher than that of the ambient air, so a large amount of the laser is contained in the liquid core through refraction. After the liquid core breaks apart, the laser light is scattered and illumination of the liquid stops. The sole purpose of this technique is to measure the length of the liquid core.

This method has been used to image the liquid core in a multi-hole diesel injector [71], as well as air blast atomizers [26]. These initial studies predicted slightly longer liquid core lengths as compared to those predicted by high speed Mie scattering images [57], however neither result is experimentally verifiable. An optical connectivity image can be seen in Fig. 3.2

This method is new and there are still some questions about its accuracy. For instance, Charalampou et al. noted that the surface of the liquid core is not necessarily geometrically formed to permit refraction, the liquid core may contain narrow regions followed by thick regions that would not be adequately illuminated, and in highly atomizing sprays, the image of the core will be multiply scattered on the way to the camera [27]. However, the method is appealing due to its simplicity, low cost, and effectiveness under certain conditions.

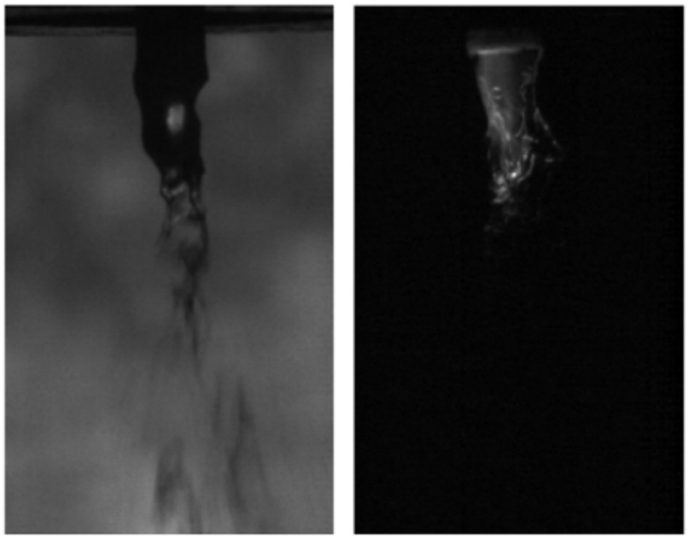

Figure 3.2: Optical connectivity demonstrated, with shadowgram image of spray on left and optical connectivity image on the right. Images from [71].

3.1.7 Laser Doppler Velocimetry

Laser Doppler Velocimetry (LDV), also known as laser Doppler Anemometry (LDA), is a technique that uses lasers to characterize the velocity of the spray. In its

typical implementation, two collimated, monochromatic, and coherent laser beams are crossed at an angle. The lasers interfere with one another in the region where they cross, generating a fringe pattern of fluctuating intensity at a known spacing. As particles from the spray then pass through this region, reflected light is detected and the velocity can be calculated by observing the frequency of the reflection intensity. The Phase Doppler Particle Analyzer (PDPA) is based on LDV and can measure the size, velocity, and concentration of spherical droplets in sprays. PDPA measurements are taken simultaneously so correlations can be made between quantities.

As the frequency measurements depend on the known properties of the laser, these methods require no calibration. They are highly accurate for spherical droplets in the dilute region of the spray, and have been used extensively to characterize atomizing sprays [51, 123, 159, 183, 186]. These methods can also work to characterize internal flow of transparent nozzles, provided the fluid is seeded with particles, for instance TiO_2 [6].

3.1.8 X-Ray Phase Contrast Imaging

When an X-ray beam traverses through a sample, its amplitude and phase are both altered. In X-ray phase contrast imaging (PCI) the altered phase of the X-ray is measured and the difference in phase is transformed into variation in the intensity, thus generating an image. The goal of this imaging technique in its application to sprays has been to help understand the primary atomization process in the near-field region [96, 97, 111, 202, 203]. As a dense cloud of liquid droplets can interfere with the X-ray phase signal, their effectiveness in imaging the internal features of the spray formation region has been questioned [108].

Alternatively, X-ray PCI can be used to characterize the geometry of metal injectors as shown by Kastengren et al. [90], and it can be used to observe cavitation in metal nozzles as shown by Duke et al. [47]. In their cavitation study, Duke et al.

added a cerium contrast agent to the surrogate fuel and high powered X-ray PCI was then used to image the inside of a diesel injector during injection. This is a ground breaking study in cavitation as all previous internal imaging of cavitation has been done on transparent injectors at significantly lower pressures and lower velocities. The study showed that tapered nozzles suppress cavitation, and that cavitation can still occur in hydro-ground nozzles.

3.1.9 X-Ray Radiography

In X-ray radiography the attenuation of an X-ray beam is measured after it has passed through the spray. Beer's law is then used to determine the amount of fuel through which the beam passed. There is typically a significant amount of noise in the signal so it is common to take multiple measurements (128-256) to smooth the results [89]. This produces a time averaged, quantitative liquid length of the spray. Some X-ray radiography methods do work in a single shot, allowing for time resolved spray density measurements [68].

This method is commonly used by experimentalists to characterize the spray density. Because X-ray beams can penetrate the dense liquid core, these measurements can be taken directly at the nozzle exit. These results are helpful for the validation of computational models.

3.1.10 Computed Tomography

In X-ray computed tomography (X-ray CT), a series of X-ray radiography images are taken from different locations, and computer analysis is used to construct a three-dimensional image of the object. CT scanning requires a static sample, which has effectively limited its use in this field to characterizing the internal geometry of injectors [90].

3.2 Experimental Observations

Experimental observations have shown that spray atomization is dependent on many factors. The following section will summarize some of these studies, addressing the influence of nozzle geometry, turbulence, cavitation, and ambient conditions.

3.2.1 The Influence of Nozzle Geometry

Nozzles directly constrain the flow, having tremendous influence on the internal flow field and, subsequently, the spray. Engineers design nozzles with a variety of parameters in mind: liquid and vapor penetration, fuel flow rate, the control or suppression of cavitation, and minimizing post injection fuel drip, to name a few. Geometric variables that can influence the flow include nozzle hole conicity, the geometry of the inlet orifice, the roughness of the nozzle surface, and the upstream inlet flow.

Many experimentalists have highlighted the influence of internal flow on spray development. The following section will present a selection of studies that are representative of typical observations that can be found in literature. Some studies discuss nozzle geometry effects with a focus on induced turbulence or cavitation. These will be discussed in the corresponding subsections to follow.

A simplified schematic of two popular types of direct injection injectors can be seen in Fig. 3.3. Fuel injection starts when the needle lifts off of the seat. This allows fuel to flow past the needle and out the nozzle holes. A production injector typically has from 5 to 10 holes [101], although single-hole nozzles are commonly used in an experimental setting [89]. Injection stops when the needle drops onto the seat, cutting off the fuel flow.

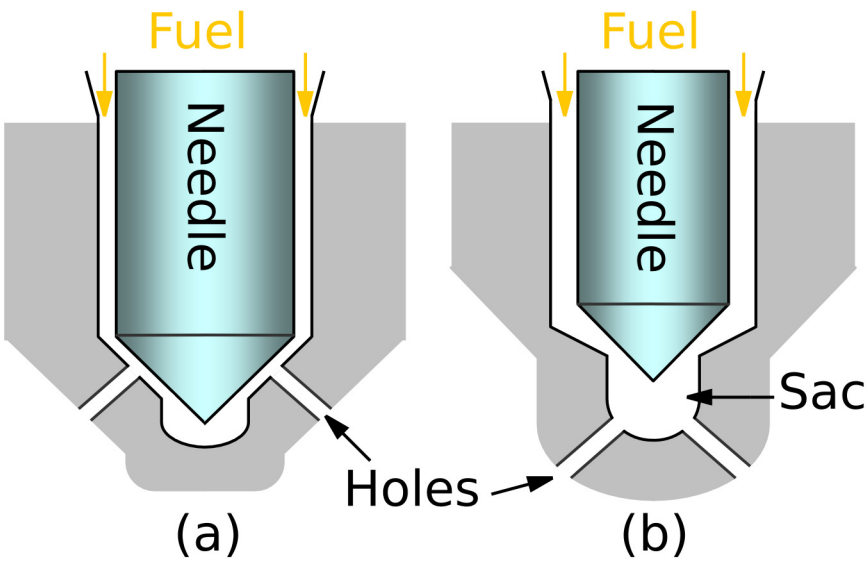

Figure 3.3: Two types of diesel injectors: VCO injector (a), and sac-type injector (b). Adapted from [117].

A common issue with fuel injectors is that small amounts of fuel escape into the combustion chamber after the needle has dropped. This results in UHC emissions. Injector (a) in Fig. 3.3 is a valve-covered orifice (VCO) injector. VCO injectors address this problem by seating the needle directly over the nozzle holes. This problem can also be mitigated by reducing the size of the sac in the sac-type injector (part (b) in Fig. 3.3). Small sac injectors are often referred to as mini-sac injectors. The trade-off between the conventional sac-type of injector and a mini-sac or VCO injector is that the close proximity of injector holes to the needle means that fuel enters the holes with an asymmetric inlet velocity. This leads to asymmetric sprays that may not atomize well, and it potentially leads to nozzle cavitation which can damage the nozzle [158, 189].

Emissions testing on engines can indirectly reveal the significant influence the nozzle geometry has on the spray. In a test conducted by DaimlerChrysler Group Research, emissions data were collected for the same injection under two different loading points with two different nozzles (VCO and sac-type). As can be seen in Fig.

3.4, the VCO injector has fewer hydrocarbon (HC or UHC) emissions, indicating that post injection drip is minimized. For this particular VCO nozzle, this came at the cost of high levels of soot emissions under certain loading conditions [189].

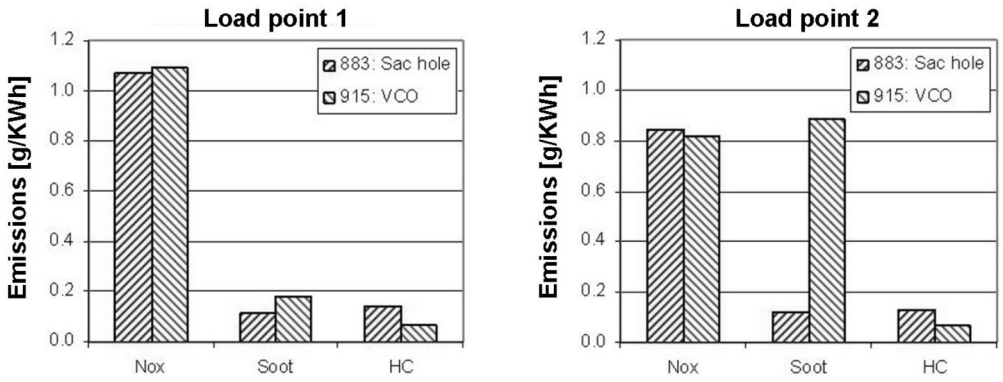

Figure 3.4: Emissions production for a common rail diesel engine at different load points with sac-type and VCO nozzles. Reproduced with permission from [189].

In 2002, Han et al. [69] conducted a detailed experimental and numerical study looking at single-hole and multihole nozzles, with cylindrical and tapered geometries in VCO and mini-sac injectors. Additionally, the single-hole nozzles were differentiated by various grades of hydrogrinding. Experimental imaging of the far region of the spray and pulsed-laser microscopy of the dense region revealed that nozzle geometry has a significant influence on fuel atomization. Showing that conicity delays primary atomization, increases spray tip penetration, and decreases spray angle. Han et al. also noted that there are significant differences in the spray structure for single-hole versus multihole injectors, which indicates that flow upstream of the nozzle flow also influences the spray.

This idea was supported by a simple 2006 study conducted by Stahl et al. where an insert was placed into a transparent nozzle directly by the inlet orifice. The insert was shown to have significant effects on the spray; inducing cavitation at the inlet orifice, enhancing turbulence and resulting in faster atomization [183].

The effects of conicity were further investigated in the work of Blessing et al. [21] through photography of enlarged transparent nozzles, and Payri et al. [142] through hydraulic characterization on real-sized diesel type injectors. These studies both showed that in non-evaporating conditions, increasing the conicity increases liquid penetration and decreases the cone angle. Payri et al. conducted a similar study under evaporating conditions in 2008 [146] showing the same result. Payri et al. concluded that cavitation increases spray angle while also increasing exit velocity due to the conservation of mass and the lower density of the cavitating vapor. All of these results are supported by computational studies like the one conducted by Som et al. [153] which showed that conicity suppresses turbulence and cavitation within the nozzle (turbulence and cavitation both aid in primary breakup).

In 2011, Payri et al. [147] observed the influence of nozzle diameter on spray angle and spray penetration. The study was conducted on three similar axisymmetric, single-hole nozzles in non-vaporizing diesel injection conditions. The nozzles were all tapered and hydro-eroded to prevent cavitation. It was observed that in the initial transient portion of the injection, the spray penetration and spray angle are both independent of the nozzle diameter. In the steady portion of the injection, spray angle remained independent of diameter while spray penetration increased with increased diameter.

In diesel DI engines the nozzle diameters tend to be small (around 100 μm). At this size, consistent manufacturing to designed specifications is a challenge. Evidence of this was found by Karimi, who observed hole-to-hole variation in spray angle and penetration in multi-hole production diesel injectors [84]. And it has been directly observed by Kastengren et al. with four "Spray A" injectors from the Engine Combustion Network (ECN). In their 2012 Atomization and Sprays paper, four nominally identical axisymmetric single hole injectors were characterized through X-ray

tomography, X-ray PCI, silicone molding, and optical microscopy. Needle motion and hydraulic behavior were also observed [90]. The conclusions were as follows,

- all four nozzles were misaligned and offset slightly from the nozzle axis
- the diameter vs. axial distance profile for the nozzles deviated slightly from the nominal specification, including a slight convergence near the nozzle exit
- the exit profiles were not perfectly circular and the diameters varied by around 5 μm
- the nozzles exhibited similar axial needle lift behavior and different lateral needle motion
- the nozzles had similar C_v, C_a, and C_d

This was a very interesting result, which begged the question of how these nozzle eccentricities affected the flow itself.

This was answered in 2014, when Kastengren et al. used X-ray radiography from a variety of angles to generate a 3-D time resolved characterization of the spray for these same four nozzles. Injection was conducted under the ECN target "Spray A" condition which is meant to represent diesel operating conditions (900 K and 6 MPa ambient gas, 150 MPa injection pressure). In this work, it was shown that spray eccentricity exists for each nozzle in the same orientation as the nozzle eccentricity. Kastengren et al. thus concluded that diesel spray structure is highly sensitive to nozzle geometry and that even nominally identical injectors may produce different sprays [89]. In fact, of the seven "axisymmetric" nozzles tested by Kastengren et al., none produced a truly axisymmetric spray [86] [87] [89].

Kastengren et al. suggested that it is likely that the effects of the nozzle eccentricities in single-hole injectors are more pronounced than in multi-hole injectors where the inlet flow asymmetry is stronger [89]. This is a very interesting suggestion that

seems to make sense if the asymmetric inlet conditions influence the flow in a way that overpowers, mixes, and/or dissipates the effects of the nozzle eccentricities. This could be done through an influence on the turbulence of the nozzle flow, through sustained swirling in the flow, and/or through internal cavitation. All of which are effects that are known to be more pronounced in multi-hole injectors, especially of the VCO or mini-sac type [158]. The idea is particularly plausible for eccentricities that exist far from the exit of the nozzle, as the asymmetric flow would have more time to mitigate the effects of the eccentricities before exiting the injector. Conversely, it is hard to imagine the effects of nozzle eccentricities close to the nozzle exit being so influenced by asymmetric inlet flow e.g. a non-circular exit orifice will always affect the spray. Perhaps the idea warrants more experimental or computational investigation, and researchers should certainly be cautious when drawing comparisons between multi-hole and single-hole nozzles.

3.2.2 The Influence of Turbulence in the Nozzle

In 2005, Stahl et al. conducted a study specifically looking to see how nozzle geometry affects the spray by influencing the turbulence of the flow. To do this, they used three nozzles of equal diameter but with slight variations in their geometries. One nozzle was conical, preventing the flow from having time to develop significant turbulence, and the other two contained a long ($L/D \simeq 10$) cylindrical nozzle in which turbulence could develop. The cylindrical nozzles were differentiated in that one contained an object directly above the conical section to force asymmetric inlet flow. The nozzles were observed at $Re = 5000$ and $Re = 6700$. The work concluded the type and intensity of the turbulence dramatically changes the spray angle [182].

Similarly, in a 2010 work by Balewski et al. [6] the effects of turbulence on spray break up were investigated with a pressure atomizer where different pre-nozzle inlays were used to modify the nozzle inlet flow. This was a very interesting study

that used LDV to measure the velocity and turbulence profiles inside the transparent cylindrical nozzle, high speed photography to determine spray angle, PDA to measure the velocity and size distribution of the droplets in the spray, and X-ray radiography to evaluate the liquid density distribution. The L/D of the cylindrical nozzle was 10, with a 1 mm diameter. The flow rate was set for a Reynolds number of Re=2300. This was the limit for their set up as higher flow rate caused inlet cavitation with the V5 nozzle inlay. The design of the inlays can be seen in Fig. 3.5, and the resulting spray can be seen in Fig. 3.6.

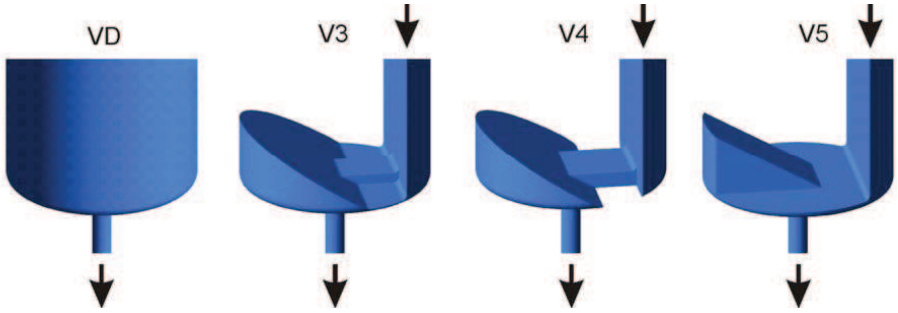

Figure 3.5: Design of pre-nozzle nozzle inlays to influence inlet nozzle flow. Reproduced from [6].

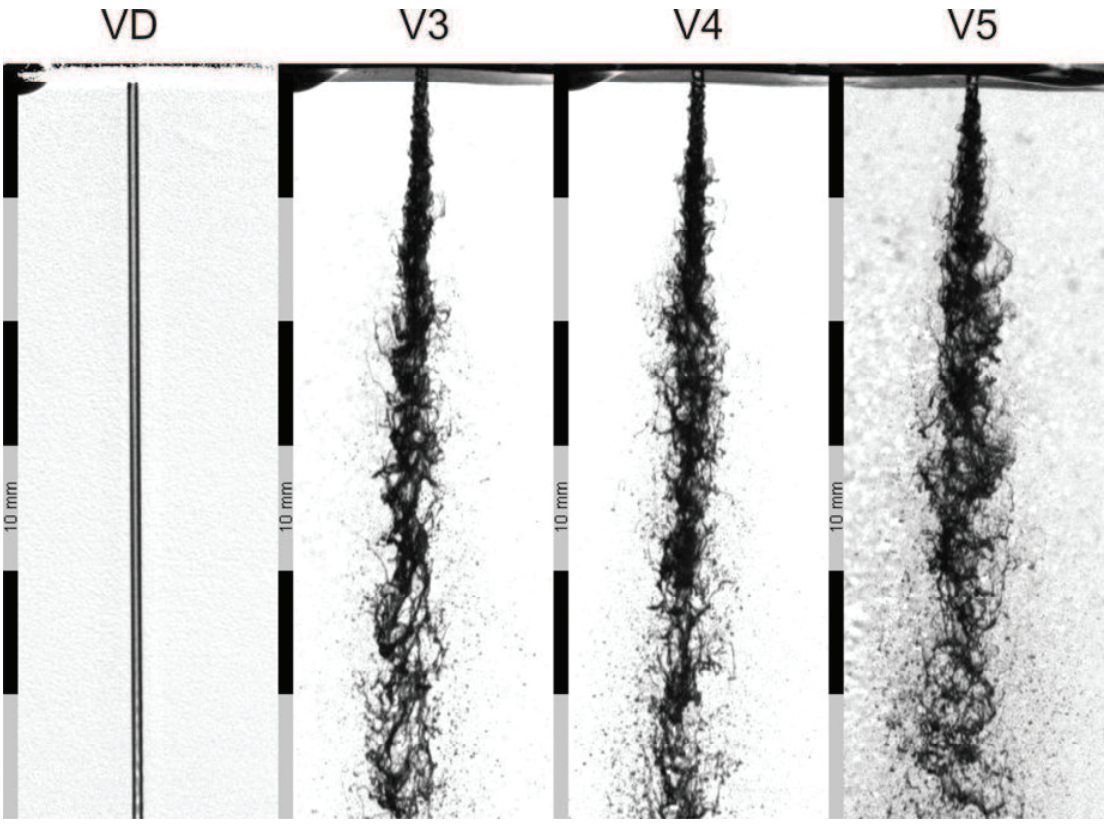

Figure 3.6: Images of resulting sprays for different pre-nozzle inlays. Reproduced from [6].

The LDV observations of the liquid flow at the nozzle exit revealed that the flow was laminar for the VD case, and turbulent for V3-V5 cases. It also revealed asymmetric internal flow patterns in the V3-V5 nozzles. As can be seen in Fig. 3.6, this work clearly proved the tremendous influence the internal flow and turbulence level has on the breakup of the jet.

Finally, in the 2011 work by Payri et al. [147], the effects of the flow regime in diesel nozzles were characterized. Here the degree of turbulence was inferred by observing the change in the area contraction coefficient C_a, and the effects on the spray were quantified by spray angle. This test was conducted on non-cavitating tapered diesel nozzles in non-vaporizing conditions. The results showed that the lower the C_a, i.e. the lower the degree of turbulence, the smaller the spray angle.

3.2.3 The Influence of Cavitation in the Nozzle

Cavitation is the growth and subsequent collapse of vapor bubbles within a liquid that occurs when the pressure of the liquid drops below its saturation pressure at a given temperature. This can occur through a reduction in static pressure due to the hydrodynamic motion of the liquid, or through a reduction in pressure driven by acoustic waves in the flow. In direct injection injectors, cavitation is often caused by an abrupt change in the geometry of the nozzle, at the sharp transition near the nozzle inlet orifice, for instance.

Although cavitation can be beneficial for the break-up of sprays, it also has some downsides. For example, the collapse of vapor bubbles can be a violent process that generates enough force to cause surface erosion in the nozzle. Additionally, because the vapor phase is much less dense than the liquid, cavitation can limit the mass flow rate of the fuel.

Studies have been done to investigate the presence of cavitation based on hydraulic characterization through trends in the C_d. For instance, in 2004, Benajes et al. [17] studied the influence of conical and cylindrical nozzle orifices in common rail injection systems on injection rate behavior. Their study was conducted at maximum needle lift and it showed that a conical orifice suppressed cavitation, increased the C_d, and, due to the smaller orifice diameter of their conical nozzle, increased exit velocity and reduced mass flow rate. Also through hydraulic characterization, Payri et al. [143] observed that in conical nozzles mass flow rate was always proportional to the square root of pressure drop, thus indicating that conical nozzles suppress cavitation. In the same study, Payri et al. observed indicators of cavitation for cylindrical nozzles, such as choking conditions and increased exit velocity due to the presence of vapor.

Many experimental studies on cavitation are done using various optical imaging techniques. The clear nozzles required for these techniques cannot withstand the pressures and velocities typical of production injectors. Because of this, these studies

are done at lower pressures and lower velocities [28, 29, 120], and often on enlarged injectors [158, 186]. These studies have helped to reveal the mechanisms of cavitation, however they do not accurately represent the flow within high pressure Diesel injectors.

Thankfully, advancement in experimental methods is now allowing for the internal imaging of metallic production injectors under diesel operating conditions. As discussed in section 3.1, this is done through high energy X-ray phase contrast imaging of unmodified metal diesel injectors [47, 48].

3.2.4 The Influence of Ambient Conditions

In atmospheric conditions, air has a density of approximately 1 kg/m^3. At the moment of injection, density of the gas in a diesel engine can be upwards of 22 kg/m^3 [1]. The density of the injected diesel fuel is around 800 kg/m^3 [25]. This makes for a fuel/chamber density ratio of 800:1 for injection into atmospheric conditions vs. 40:1 for diesel conditions. This difference is significant; experimental observation shows that spray angle increases and liquid length decreases with elevated ambient density [87, 147].

As the ambient temperature of the gas is increased beyond the boiling point of the fuel, vaporization of the fuel is introduced. In diesel operating conditions the ambient temperatures can be as high as 900-1000 K. This is well beyond the boiling point of diesel fuel, so vaporization occurs quickly; it has been shown that in vaporizing diesel conditions the liquid penetration is a small fraction of the total spray penetration [178].

The presence of vaporization influences the spray penetration and dispersion in an interesting way. Naber and Siebers [122] and Huang [76] have shown that sprays penetrate slower and disperse less under vaporizing conditions. The differences tend to be small, around $\sim 10\%$ in typical diesel conditions, and they occur more noticeably

at higher liquid/chamber density ratios. Clearly the added process of vaporization influences the spray in an interesting way as one would expect the change in spray penetration and dispersion to be negatively correlated.

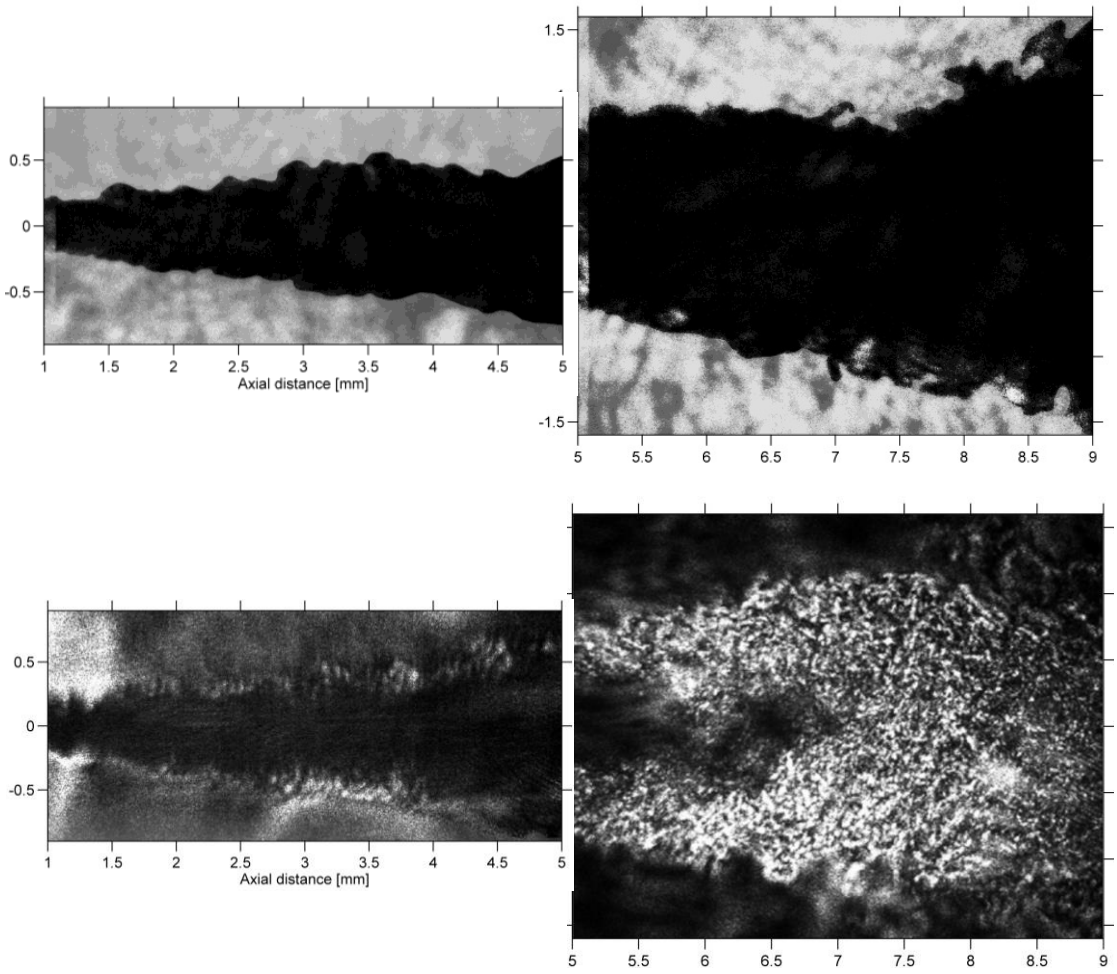

Figure 3.7: Ballistic images of Spray A nozzle 210677 injection. Top images were taken at 440 K - 22.8 kg/m^3, bottom images were taken at 900 K - 22.8 kg/m^3. Shown with permission from Professor Mark Linne, Chalmers University of Technology.

Experimentalists have also observed the influence that vaporization has on the fuel/gas interface in the near-field region. Ballistic imaging of the near-field region of diesel injection at two different chamber temperatures can be seen in Fig. 3.7. Here it is shown that at relatively cold conditions there is a distinct boundary between liquid and gas, whereas at 900 K this boundary does not exist. This is indicative

of an interesting phenomenon that Dahms et al. [32] and Dahms and Oefelein [33] have been working to understand. They have noted that under some conditions a distinct gas-liquid interface no longer exists, surface tension effects are diminished and the jet appears to undergo a continuous change of state with mixing being diffusion-dominated [32, 33]. In these conditions it would appear that atomization is better described as a single-phase, diffusion-dominated mixing process, rather than the classic two-phase spray atomization mechanism shown in Fig. 2.2.

This is in line with what Siebers observed over one decade earlier [178, 179]; by examining changes in liquid length with change in orifice diameter and injection pressure, he showed that vaporization rate is not controlled by interphase transport. Stating that, "the processes of atomization and the ensuing interphase transport of mass and energy at droplet surfaces are not limiting steps with respect to fuel vaporization in DI diesel sprays," his work instead indicated that turbulent mixing and gas entrainment are pivotal.

The observations of Dahms et al, and Siebers are are particularly interesting to those working with the $\Sigma - Y$ model. This is because $\Sigma - Y$ predicts atomization as turbulent mixing in a variable density complex multiphase mixture. This model will be discussed further in section 4.5.1.

3.2.5 The Influence of Flash-Boiling

A multitude of experimental studies have attempted to characterize the behavior of flash-boiling sprays. Among them, it is commonly observed that the spray structure is completely altered by flash-boiling conditions; penetration is reduced, atomization and spray angle are increased, and often a large recirculating toroidal vortex is present around the tip of the jet [151, 175, 208]. Compared to non-flashing conditions, where the Weber number and Reynolds number are highly important [212], under flashing

conditions Zeng et al. [211] and Xu et al [208] have shown that it is the ambient to saturated pressure ratio (P_a/P_s) which correlates well with spray characteristics.

Experimental studies done on multi-hole injectors commonly observe a collapse of the spray under hard flashing conditions [2, 4, 140, 172, 198, 211, 213]. This collapse typically occurs at or below (P_a/P_s) of 0.3 as the quickly expanding spray plumes interact with one another [211]. The collapse of these sprays alters the designed directionality of the injectors and inhibits mixing with the ambient gas. Hole-to-hole variation in mass flow rate [184] and spray plume structure [22] are also commonly observed. In such cases, it is possible that factors such as asymmetry in the nozzle geometry and the manufacturing defects work together to generate asymmetry in the flow.

Many experimental studies describe their observations with semi-empirical zero or one-dimensional models [124, 135, 175, 208, 212]. These are beneficial to an extent, however, they will never be able to represent the sprays generated by the complex geometries present in production injectors. Consider, for example, the significant influence something as subtle as manufacturing imperfections can have on sprays: Kastengren et al. observed differences in sprays from nominally identical diesel injectors [90], and Zhang et al. observed differences in GDI sprays from nominally identical injectors which were fabricated with different techniques [214]. Capturing the influence of such subtle differences is beyond the scope of lower order models, however CFD can capture these effects [209]. For this reason, CFD simulations have an important role to play, both as an engineering design tool and in the academic investigation into the complex physics occurring within these sprays.

3.3 Conclusions

This chapter covered the experimental characterization of sprays by first highlighting selected techniques. While no single experimental technique is capable of

characterizing the whole spray, many of them are complementary and can be implemented together to provide a good overall description of the spray. For instance, schlieren imaging can capture spray angle and liquid and vapor penetration, PDPA can capture droplet size and velocity in the dispersed region, X-ray radiography can capture the fluid density distribution within the nozzle and the dense regions of the spray, ballistic imaging can characterize the surface of the dense liquid core, and X-ray PCI can be used to image any cavitation that may occur in the nozzle. Unfortunately, no technique is able to provide a thorough characterization of the flow within the dense core region.

Next, relevant literature was reviewed and common experimental observations were detailed. It was shown that the nozzle geometry is of particular significance, with the type of nozzle, the conicity of the nozzle, and the number of holes all influencing the internal flow and, subsequently,the spray. The level of turbulence within the nozzle was shown to increase the spray angle, and cavitation was shown to aid in atomization, while also having the potential downside of limiting flow rate and damaging the nozzle. Conicity was shown to effectively suppress cavitation. Finally, the influence of ambient conditions was discussed. Increased ambient density increases spray angle and decreases penetration, and elevated ambient temperature induces vaporization which slightly slows penetration and decreases spray angle. Additionally, under elevated pressures and temperatures, the interface between liquid and gas phases appears indistinct, suggesting that mixing is a diffusion-dominated process.

With the end goal of designing better combustion systems, these experimental techniques and corresponding observations are of value for two primary reasons. First, they can be used to inform design decisions, and second, they can be used to validate computational models, which can then be used to inform design decisions. As the atomization of a liquid jet is a complex process with many variables, design based

only upon experimental observation would be highly inefficient. For this reason the development of better CFD models is important.

CHAPTER 4

CFD MODELING OF MULTIPHASE INTERNAL NOZZLE FLOW AND EXTERNAL SPRAYS

For many years computational scientists have been working to fill in the gaps left by the experimentalists within the nozzle and the near-field regions. In this chapter, the popular multiphase methods relevant to modeling multiphase flow in these regions are described and literature related to their application in fuel injection is reviewed and analyzed.

4.1 High-Fidelity Sharp Interface Approach

4.1.1 Direct Numerical Simulation

Direct numerical simulation (DNS) involves solving the governing equations of the flow for all length and time scales present. Depending on the conditions of the spray, the form of these equations will differ. For instance, when modeling primary atomization at very high injection pressures, the flow velocities can approach the speed of sound and the compressible formulation of the Navier-Stokes equations is necessary. Under milder injection velocities, when the Mach number is less than 0.3, the incompressible formulation is appropriate. Assuming the Mach number is low and the multiphase system consists of two immiscible fluids, the flow would be governed by the unsteady variable density Navier-Stokes equations in the incompressible limit, seen below as Eqns. 4.1 and 4.2.

$$\nabla \cdot u = 0 \tag{4.1}$$

$$\frac{\partial \mathbf{u}}{\partial t} + \mathbf{u} \cdot \nabla \mathbf{u} = (-\nabla p + \nabla \cdot (\mu(\nabla \mathbf{u} + \nabla^T \mathbf{u})) + \rho \mathbf{g} + \mathbf{T}_\sigma)\frac{1}{\rho} \tag{4.2}$$

The surface-tension term, T_σ, in the momentum equation (Eqn. 4.2) is only non-zero on the interface between the two fluids. This presents one of the challenges in high-fidelity numerical modeling of multiphase flows: tracking the interface between the two fluids. This challenge is especially significant in spray modeling where the interface between the two fluids is constantly moving, deforming, and breaking apart. Another problem that is only present at the fluid interface is properly handling the discontinuous fluid properties.

Because a DNS requires the resolution of all length scales in the flow, the topology change that occurs in liquid break-up poses a problem. When a liquid droplet or ligament breaks apart, it first pinches to a point pushing the length scale to zero. This makes a true DNS of droplet break-up impossible. The pinching process therefore must be approximated, either implicitly by an interface-capturing method, or by a pinching model. These methods will be described in more detail later in this chapter.

To gain a sense of the cost of conducting a DNS of internal nozzle flow and near-field external sprays, the Kolmogorov length scale can be calculated. This length scale is representative of the smallest eddy present in a turbulent flow, and it is defined in Eqn. 4.3.

$$\eta = \left(\frac{\nu^3}{\epsilon}\right)^{1/4} \tag{4.3}$$

For diesel injection at 150 MPa through a nozzle with a diameter of 100 μm, η would be approximately 30 nm. In order to resolve a 30 nm eddy, the length scale of the mesh would have to be 4 times smaller: approximately 7.5 nm. This is 13,000 times smaller than the nozzle diameter and 500 times smaller than a 4 μm droplet in the downstream spray.

4.1.2 Large Eddy Simulation

Subgrid source terms can be added to high-fidelity multiphase simulations, creating computationally less expensive large-eddy simulation (LES) models. LES models, then, are a good solution for problems which demand a high-fidelity solution that are too expensive for DNS.

Similar to a DNS, high-fidelity sharp interface LES simulations rely on first principles with the interfacial effects being directly simulated. This means that both primary and secondary atomization can be captured, making these approaches a beneficial tool in helping to understand the underlying mechanisms which determine a nozzle's spray characteristics.

The popular approaches used to simulate the sharp fluid interface will be discussed in the following sections.

4.1.3 Interface-Capturing Methods

The interface between two fluids can be captured by the addition of a passive scalar field that is advected through the computational mesh. There are two interface-capturing methods, volume of fluid (VOF), and the level-set method. Interface-capturing methods automatically handle the topology changes involved in droplet break-up when two interface surfaces come together into a single cell. These methods, therefore, have a break-up length scale that is limited by the local grid size.

4.1.3.1 VOF

Here a marker function, ψ, tracks the liquid volume fraction of each computational cell. The liquid interface is then reconstructed from this marker function. The VOF method is a popular method partly because it can easily be constructed to be liquid volume conserving. Unfortunately, because of the discontinuous nature of ψ, its advection must be solved with special geometric algorithms to avoid numerical

diffusion [67] and [156]. A more thorough description of this method can be found in the 1999 paper by Scardovelli and Zaleski [164].

A novel, second-order, unsplit VOF method was recently proposed by Chenadec and Pitsch [30]. This method couples VOF to a consistent, monotonicity-preserving discretization of the Navier-Stokes equations, with the goal being the study of turbulent primary atomization at arbitrary density ratios. The study validated the approach by modeling the atomization of a planar jet, showing the influence of mesh resolution on drop size distribution and conservation errors. They then used the model to observe the break-up of a jet from a turbulent cylindrical pipe, with a liquid/gas density ratio of 40 and Re=5000. Overall results were promising and the authors suggest that further research and validation will occur with a focus on quantification of the mesh requirements. Conservation errors here were small, around 0.25%.

4.1.3.2 Level-Set

In the level-set method, the interface is marked by a specified value, ϕ_0, of a tracking scalar field, ϕ. In one fluid, $\phi > \phi_0$, and in the other fluid $\phi < \phi_0$. The value of ϕ away from the interface can be defined by a number of smooth functions, such as the signed distance function, $|\nabla\phi| = 1$ [65]. A more thorough description of the level-set method can be found in the 2013 work by Sethian and Smereka [173].

Unlike VOF, the level-set method does not preserve liquid volume. Because the volume errors depend on the grid resolution, the method is frequently supplemented by a grid-refinement strategy. Popular grid-refinement strategies include the structured adaptive mesh refinement (SAMR) which is well suited for compressible flows [130] and the refined level-set grid (RLSG) method which works for both structured and unstructured meshes [72].

Liquid conservation can also be achieved through coupling the level-set method with the VOF method. Introduced in 2003 by Sussman, the coupled level-set volume-

of-fluid (CLSVOF) method is second-order accurate [188] and treats the liquid as incompressible and the gas as isobaric. In 2007, Sussman et al. introduced a new formulation of the CLSVOF method that treats both fluids as incompressible [187]. The CLSVOF method has proven to be robust and stable even for high-density ratios [187] [119].

Furthermore, liquid conservation can also be attained through the conservative level-set method, presented by Olsson and Kreiss in 2005 [132]. This method uses a smeared Heaviside function for ϕ, where $\phi_0 = 0.5$ and a hyperbolic tangent function smooths ϕ to zero on one side of the interface and one on the other. The interface is moved in a two step process, first through advection and then through a re-smoothing of ϕ. Second-order accurate, conservative approximations are used in both steps, resulting in a method that shows both second-order accuracy and very good liquid conservation. This method was improved upon and coupled with the ghost fluid method in 2008 by Desjardoms et al. [41]. It was then used to model the turbulent atomization of a diesel jet at $Re = 3000$. The method proved to be robust and the mass conservation errors were small.

In 2009 Desjardins et al. [43] presented a level-set scheme capable of providing a more accurate interfacial curvature through a spectrally refined interface (SRI). The method attains a subcell resolution of the interface by introducing a set of quadrature points with known values of the level-set function into each cell. The resulting approach essentially eliminates the mass conservation issues and provides improved accuracy of the interface curvature and transport [42, 43].

4.1.4 Interface-Tracking Methods

Sometimes called front-tracking, in interface-tracking many marker points are placed on the interface between the fluids and their motion is tracked. Typically these marker points are advected in a Lagrangian way, forming an interface surface

grid that moves through the fixed-flow solver grid [193, 194]. In interface-tracking methods topology changes are not handled automatically. Because of this limitation, these methods have never been applied to a DNS of primary breakup [65].

4.1.5 Ghost Fluid Method

The ghost fluid method, or ghost fluid approach, developed by Fedkiw et al. in 1999 [58] is commonly used in multiphase flow to handle the singular surface tension force and the discontinuous material properties, both of which exist at the interface between the two fluids. In this approach, a band of 3 to 5 ghost cells surround the fluid interface and contain properties for the fluid on the opposite side of the interface. The ghost cells allow for computation to occur for both phases independently, as if the interface was not present. The fluid interface is then advanced (typically with some form of the level-set method), and the new interface location is used to determine which fluid properties to use.

The method has been widely adopted, especially alongside level-set methods. It is efficient, robust, and accurate. The results of the work of Desjardins et al. [41, 43] suggest that the ghost fluid method is accurate, even with a small number of grid points (< 10), for problems like Rayleigh breakup, Rayleigh-Taylor instability, and the decay of standing waves. This suggests that the ghost fluid method is well suited to handle the small structures expected in the primary breakup of an atomizing spray.

4.1.6 DNS and LES Results of Primary Atomization

The DNS of the primary atomization process has been attempted using the VOF method by de Villiers et al. [201], Bianchi et al. [19], and Chenadec and Pitsch [30], the CLSVOF method by Menard et al. [118] and [119] and Lebas et al. [99] , the conservative level-set method by Desjardin et al. [40], the RLSG method by Kim et al. [91], and the SRI approach to the level-set method by Desjardins and Pitsch [42].

In the examination of these studies it is evident that significant progress has been made towards conducting DNS of primary atomization. For instance, in the older works, mesh resolution was often not fine enough; mesh convergence studies typically either showed a lack of convergence [201] or they were not conducted [19, 40, 118, 119]. This is not so for the more recent study conducted by Chenadec and Pitsch [30]. Here Chenadec and Pitsch modeled the primary atomization of a scaled up cylindrical jet that was designed to reproduce features characteristic of diesel injection. The study included density ratios of 40:1 and 800:1, and the analysis included a mesh convergence study in addition to validation against experimental nozzle velocity and droplet distribution data.

In spite of these improvements, DNS studies are very far from be able to completely model diesel injection. While the results of Chenadec and Pitsch's study were good, the computational costs were high, taking upwards of 100,000 CPU hours. The study was also conducted on an enlarged nozzle at Re=5000, and in non-vaporizing conditions. This means length scales were larger, velocities were much slower, turbulence was less intense, and compressibility and vaporization effects were disregarded. All of these factors dramatically reduce the expense of the computation.

A couple of good examples of recent high fidelity multiphase LES models are the works of Shost et al. [177] and Befrui et al. [14]. They both used a VOF-LES model to simulate GDI sprays and elucidate the influence of nozzle geometry, flow turbulence, and aerodynamic instabilities.

Although a true DNS of the primary atomization of a highly atomizing spray currently unattainable, these high fidelity methods do have their place. Directly capturing interfacial effects allows for insight into the underlying physics of the atomization process. This insight can then inform lower fidelity engineering level models. DNS and LES models can also provide quantitative results for the validation of models where no experimental data is available. In their 2013 Atomization and Sprays

paper, Demoulin et al. describe this process in relation to the validation of the Eulerian-Lagrangian spray atomization (ELSA) model [34].

Unfortunately, the high fidelity sharp interface approach faces two significant drawbacks when applied to spray modeling. First, it can be prohibitively expensive as it requires that the interface be fully resolved. While this is possible for some Reynolds and Weber number sprays, the high Reynolds and Weber numbers present in most diesel and some GDI sprays render this approach extremely expensive. Furthermore, the expense is compounded significantly in flash-boiling conditions where very small bubbles can be present within the spray itself, rendering the interface extremely complex. Second, this approach is inappropriate altogether when a sharp interface is not physically present, for instance in diesel sprays which can be near-supercritical [32, 33].

4.2 Lagrangian-Eulerian Approach

The Lagrangian and Eulerian specifications of a flow field are two different ways of looking at flow. In the Lagrangian specification, individual fluid parcels are tracked through time and space. In the Eulerian specification, fixed positions are observed as fluid flows through these locations. The Lagrangian specification easily tracks particle motion with no numerical diffusion and the Eulerian reference frame is well suited to capture large continuous fluid domains.

The Lagrangian-Eulerian (LE) approach is also known as the Lagrangian Droplet Eulerian Fluid (LDEF) approach, the Eulerian-Lagrangian method, the Discrete Phase Model (DPM), the Discrete Phase Element (DPE) model, and the Discrete Droplet Method (DDM). Although this is not a requirement of the approach [137, 185], LE models are typically used in flows where one fluid can be considered dispersed and one considered continuous. In the case of spray modeling, this is true everywhere except inside the nozzle and within the dense core in the near-field region.

This approach is based off the work of Williams, who in 1958 proposed a statistical representation of the spray called the droplet distribution function (ddf) [207]. The ddf, $f(r, \mathbf{x}, \mathbf{v}, t)\, \mathrm{d}r\, \mathrm{d}\mathbf{x}\, \mathrm{d}\mathbf{v}$, represents the probability density distribution of droplet size and velocity as a function of space and time. The transport equation of the ddf, known as Williams' spray equation, is typically solved indirectly using a Lagrangian particle method. The Lagrangian description of the transport of the ddf avoids numerical diffusion and allows for tracking of particle attributes like size, shape, rotation, and composition. This also simplifies vaporization and drag modeling as they both directly depend on droplet size.

Early models based on the Williams' spray equation were only one-way coupled; they were basically Lagrangian particle-tracking algorithms that ignored the influence of the droplets on the ambient gas. By the 1980s two-way coupled methods were developed, the pioneers being Dukowicz, whose formulation also accounted for the volume displacement of the particles on the gas [50], and O'Rourke [133] [134] and O'Rourke et al. [3], who established early sub-models describing vaporization, acceleration, coalescence, collision, and break-up. Two-way coupling is achieved through added source terms in the Eulerian specified gas and drag terms on the Lagrangian specified liquid.

Properly implemented, this approach has proven to provide accurate results at a reasonable computational cost [50, 78, 93]. Because of this, LE models are very popular and can be found in most CFD packages. The approach, however, has some drawbacks:

- The Lagrangian description of the liquid phase does not lend itself to easily modeling the dense region of the spray. This means that fully-predictive, nozzle to spray tip, modeling can only be achieved by implementing a complex inlet boundary condition or coupling it with an internal flow model [7, 180]. Most

LE models do not do this. Instead they operate off of the bad assumption that liquid is injected as droplets that are the size of the nozzle diameter [155].

- Computational cost can be high for flows with a large number of droplets. This problem can be mitigated by coupling similar droplets together into computational parcels. The user must be careful, however, as the number of discrete elements per parcel has been shown to influence the final result [52, 93].

- For regions with higher phase fractions, the coupling between the fluid and the gas becomes very strong and numerical stability problems can result [93].

- A severe mesh dependency occurs in many LE models due to the dependence of the liquid drag term on the local gas velocity. This causes coarse cells near the liquid jet to over-predict drag [176].

- Conversely, due to the coarse mesh near the nozzle, turbulence intensity and turbulent diffusivity is often underestimated. This is because the velocity gradient here is often under-resolved [70]..

A more detailed description of the LDEF method can be found in [3] and a thorough review of Lagrangian-Eulerian methods for multiphase flows can be found here [185].

4.3 Eulerian-Eulerian Approach

In the Eulerian-Eulerian (EE) approach, also known as the Eulerian Liquid Eulerian Gas (ELEG) or Two-Fluid approach, both phases are treated as continuous over the entire domain. Averaged continuum equations, seen below as Eqns. 4.4 for conservation of mass and 4.5 for conservation of momentum taken from [79], are solved for both the liquid and the gas phases. These equations are similar to their one-phase counterparts with an added phase fraction coefficient α_k representing the probability that a certain phase is present at any given point in space and time.

$$\frac{\partial \alpha_k \rho_k}{\partial t} + \nabla \cdot (\alpha_k \rho_k \mathbf{u}_k) = 0 \tag{4.4}$$

$$\frac{\partial \alpha_k \rho_k \mathbf{u}_k}{\partial t} + \nabla \cdot (\alpha_k \rho_k \mathbf{u}_k \mathbf{u}_k) = -\alpha_k \nabla p_k + \nabla \cdot \alpha_k (\tau_k + \tau_k^t) + (p_{k,i} - p_k) \nabla \alpha_k + \mathbf{M}_k^d \tag{4.5}$$

The two phases are coupled by an additional term $\mathbf{M}_k^d$ in the momentum equation, Eqn. 4.5, which accounts for the average effect of the lift, drag, and virtual mass forces acting between the phases. The behavior of an EE model is highly dependent on the method used to model this term. The $p_{k,i}$ term is the average interfacial pressure and the $\mathbf{u}_{k,i}$ term is the average interfacial velocity. The averaged equations resulting from this approach are further described by Drew in [46].

In the past decade, the EE method has been increasingly used in spray modeling as it doesn't suffer from the near-field shortcomings of the LE approach. Iyer and Abraham developed an EE model for diesel sprays and applied it to vaporizing and non-vaporizing spray conditions [79] [80]. They achieved adequate agreement in both cases and their model was shown to be numerically convergent with regard to spray angle and liquid penetrations, which is a good result as many LE models do not show convergence.

Additionally, the EE approach can be preferred in LES simulations, where the high particle density required to achieve good statistical results can be computationally prohibitive for LE models. With this limitation in mind, Martinez et al. [116] developed an inlet boundary condition for an EE simulation of diesel sprays. The boundary condition seeks to further limit the computational expense and increase the accuracy of inlet conditions by using characteristic features of the nozzle to build an algebraic description of the spray characteristics close to the nozzle exit. This boundary condition was then implemented by Tillou et al. [191] in a LES simulation of diesel spray combustion that employed an Eulerian microscopic approach,

described here [59], that resembles the EE approach. This model produced a very accurate representation of the mean chamber pressure evolution, heat release rate, auto-ignition delay, and lift-off length.

As the EE approach is preferred where liquid volume fractions are high, and the LE approach preferred in dispersed flow, Subramaniam and O'Rourke suggested that fuel spray modeling could potentially benefit from a model that uses the EE approach in the near-field region and the LE approach in the dispersed spray region [137]. Properly executing the fluid phase handover from the Eulerian description to the Lagrangian description requires a knowledge of the relationships between the two representations. With this in mind, Pai and Subramaniam established the foundations of the EE and LE representations in the context of a comprehensive probability density function (pdf) formalism [137]. In their work, they showed that the EE pdf formalism naturally leads to the averaged Navier-Stokes equations shown above. They then show that although the LE pdf formalism results in averaged equations, the equations are not identical to those of the EE formalism. Their study shows that the fundamental quantities of both representations bear a simple relationship with one another only when the two-phase flow is homogeneous. Their paper provides the consistency relations that must be satisfied in a proper EE-LE handover.

4.4 Eulerian Quadrature-Based Moment Models

One significant limitation facing the typical Eulerian approach of a fluid is that the fluid velocity is represented by a single vector in each cell. This means that models using this approach for the dispersed phase are unable to accurately model flows that contain particles with crossing trajectories. Particle trajectory crossing is not a dominant feature in conventional atomizing sprays, so this is not an issue for most spray models. It is, however, a dominant feature in some types of atomizers, such as impinging sprays and jets in a cross flow. To overcome this limitation, Fox

[60, 61] and Fox et al. [62] developed an Eulerian quadrature-based moment method. In this method, velocity is represented by a velocity distribution function, allowing for a finite set of lower-order velocity moments to be captured.

The model has been validated through direct comparison with EE and LE models for an unsteady free-jet with monodispersed and polydispersed droplets with and without evaporation [83]. Here the number density and gas-phase fuels mass fraction both showed excellent agreement, suggesting that the Eulerian quadrature-based moment method is well suited for spray combustion.

4.5 Single-Field Diffuse Interface Eulerian Approach

The distinguishing difference between the diffuse interface single-field Eulerian approach and the high-fidelity sharp interface approach is that in the diffuse interface approach no attempt is made to resolve or capture the interface. Instead, the effects of the interface are modeled and a density-averaged flow field is solved on a lower resolution grid. This approach works well for low Stokes number flows, where the dispersed phase naturally follows the streamlines of the continuous phase. It is also a fitting approach for flows with diffusion-dominated mixing [33].

4.5.1 $\Sigma - Y$ Spray Atomization Model

4.5.1.1 Model Description

The $\Sigma - Y$ model, was introduced in 1999 by Vallet and Borghi [197]. It is founded on four assumptions:

1. At infinite Reynolds and Weber number, the large-scale features of the flow are independent of surface tension and viscosity. This is because surface tension and viscosity essentially act at small length scales where the liquid/gas interface is highly curved or where a large velocity gradient exists.

2. The velocity field of the flow can be studied in terms of mean values using standard turbulence closures, such as the classical $(k-\epsilon)$ model.

3. The dispersion of the liquid phase can be computed through a transport equation of the liquid mass fraction containing a turbulent diffusion liquid flux term to account for mixing.

4. The mean droplet size of the dispersed liquid phase can be predicted by modeling the mean surface area of the liquid/gas interface per unit volume. This term quantity is also known as (Σ).

These assumptions allow for the mean flow to be captured by a single velocity field that represents both the liquid and gas phase as a complex mixture with a highly variable density. This allows momentum and continuity to take their familiar forms as Eqns. 4.6 and 4.7, respectively.

$$\frac{\partial \bar{\rho}\tilde{u}_j}{\partial t} + \frac{\partial \bar{\rho}\tilde{u}_i\tilde{u}_j}{\partial x_i} = -\frac{\partial \bar{p}}{\partial x_j} - \frac{\partial \bar{\rho}\widetilde{u_i'u_j'}}{\partial x_i} \tag{4.6}$$

$$\frac{\partial \bar{\rho}}{\partial t} + \frac{\partial \bar{\rho}\tilde{u}_i}{\partial x_i} = 0 \tag{4.7}$$

Here an over-tilde ($\tilde{}$) denotes Favre averaging, an over-bar ($\bar{}$) denotes time averaging, and $'$ denotes a turbulent fluctuation.

As per assumption 2, a turbulence model along with the Boussinesq eddy viscosity assumption can be used to close the Reynolds stress term, $\widetilde{u_i'u_j'}$, in the momentum equation.

Regarding the third assumption, the mean liquid mass fraction is defined as ($\tilde{Y} = \frac{\overline{\rho Y}}{\bar{\rho}}$) and the averaged transport of $\tilde{Y}$ is shown below as Eqn. 4.8.

$$\frac{\partial \bar{\rho}\tilde{Y}}{\partial t} + \frac{\partial \bar{\rho}\tilde{u}_i\tilde{Y}}{\partial x_i} = -\frac{\partial \bar{\rho}\widetilde{u'_iY'}}{\partial x_i} \tag{4.8}$$

The turbulent diffusion liquid flux term, $\widetilde{u'_i Y'}$, accounts for the mixing effect of the relative velocity between the fuel and the gas.

While the approach used here assumes that the resolved momentum of the liquid/gas mixture can be characterized by a single bulk velocity, the slip velocity can be expressed explicitly as derived by [35] and seen in Eq. (4.9).

$$u_i|_l - u_i|_g = \frac{1}{\tilde{Y}\left(1-\tilde{Y}\right)} \cdot \widetilde{u'_i Y'} \tag{4.9}$$

The turbulent diffusion liquid flux term is typically closed through Fick's law of diffusion, as shown in Eqn. 4.10.

$$\widetilde{\rho u'_i Y'} = \frac{\mu_t}{Sc}\frac{\partial \tilde{Y}}{\partial x_i} \tag{4.10}$$

An alternative closure was suggested by Demoulin et al. [35], which is meant to capture the increased mixing that occurs due to increased Raleigh-Taylor instabilities in the presence of a large density gradient.

So far this system contains unknown quantities $\tilde{Y}$, $\tilde{u_i}$, $\bar{p}$, and $\bar{\rho}$, and requires one more equation for closure. This is obtained by the relationship between $\tilde{Y}$ and density. Assuming the two phases form an immiscible mixture, $\tilde{Y}$ is related to density by Eqn. 4.11.

$$\frac{1}{\bar{\rho}} = \frac{\tilde{Y}}{\rho_l} + \frac{1-\tilde{Y}}{\rho_g} \tag{4.11}$$

Under incompressible assumptions this equation closes the system, with density determined by Eqns. 4.8 and 4.11, and pressure determined through a pressure-corrector method to satisfy the continuity Eqn. 4.7.

Compressibility can be handled in a variety of ways. Ning et al. [128, 129] related density and pressure through an isentropic assumption as shown in Eqn. 4.12.

$$\frac{D\bar{\rho}}{Dt} = \frac{1}{a^2}\frac{D\bar{p}}{Dt} \tag{4.12}$$

Combining this with the continuity equation, they arrived at the pressure equation shown in Eqn. 4.13.

$$\frac{1}{a^2}\frac{\partial \bar{p}}{\partial t} + \frac{1}{a^2}\tilde{\mathbf{u}} \cdot \nabla \bar{p} + \bar{\rho}\nabla \cdot \tilde{\mathbf{u}} = 0 \tag{4.13}$$

A pressure-corrector method can be formulated to account for various forms of compressibility. Salvador et al. [162] took this approach using an experimentally derived polynomial to approximate the fluid compressibility [162]. Desantes et al. [39], Trask et al. [192], and García-Oliver et al. [64] approximated the mixture compressibility as a volume weighted average of the compressibility of each phase, using the ideal gas law for the gas phase and a speed of sound derived compressibility for the liquid phase. This is seen in Eqn. 4.14.

$$\Psi = \tilde{Y}\frac{\bar{\rho}}{\bar{\rho}_l}\frac{1}{a_l^2} + \left(1 - \tilde{Y}\frac{\bar{\rho}}{\bar{\rho}_l}\right)\frac{1}{RT} \tag{4.14}$$

The pressure equation can then be obtained by first recasting the momentum equation into its semi-discretized form, as explained by Jasak [81] and shown in Eqn. 4.15.

$$a_p \mathbf{U}_p = \mathbf{H}(\mathbf{U}) - \nabla p \tag{4.15}$$

Here a_p represents the diagonal coefficients of the momentum matrix and $\mathbf{H}(\mathbf{U})$ represents the off-diagonal terms which account for the momentum contributions from neighboring cells.

This semi-discretized form of momentum is then combined with the continuity equation to yield the poisson equation for pressure shown below.

$$\frac{D\rho}{Dt} = -\rho\nabla \cdot (\mathbf{U}_p)_f = -\rho\nabla \cdot (\frac{\mathbf{H}(\mathbf{U})}{a_p} - \frac{1}{a_p}\nabla p)_f \tag{4.16}$$

The chain rule can then be used to approximate the total derivative of density, as done by Trask et al. [192] and shown in Eqn. 4.17.

$$\bar{\rho}\nabla\cdot(\mathbf{U}_p)_f = -\frac{\partial\bar{\rho}}{\partial\tilde{Y}}\frac{D\tilde{Y}}{Dt} - \frac{\partial\bar{\rho}}{\partial\bar{p}}\frac{D\bar{p}}{Dt} - \frac{\partial\bar{\rho}}{\partial\tilde{T}}\frac{D\tilde{T}}{Dt} \tag{4.17}$$

Alternatively, for density based solvers, the pressure can be explicitly determined based upon an equation of state for the fluid. This requires the addition of an energy transport equation which is used to determine the fluid temperature. Pandal et al. [138] took this approach with the $\Sigma - Y$ solver.

As per the fourth assumption, the mean droplet size of the dispersed liquid phase can be modeled by the balance equation of Σ, the mean surface area of the liquid/gas interface per unit volume. This balance equation, Eqn. 4.18, was developed by Vallet et al. [196] and reviewed later by Beheshti et al. [15].

$$\frac{\partial\overline{\Sigma}}{\partial t} + \frac{\partial\tilde{u}_j\overline{\Sigma}}{\partial x_j} = \frac{\partial}{\partial x_j}\left(D_\Sigma\frac{\partial\overline{\Sigma}}{\partial x_j}\right) + (A+a)\,\overline{\Sigma} - V_s\overline{\Sigma}^2 \tag{4.18}$$

Here A is the production term accounting for the stretching of the fluid/gas interface due to velocity gradients, a is the production term due to interface stretching due to droplet collisions and turbulence, and V_s is the destruction term related to droplet coalescence. The D_Σ term is a diffusion coefficient term typically defined as the turbulent viscosity over a Schmidt number [64, 162]. This term accounts for the turbulent dispersion of Σ.

Under the assumption that the dispersed phase is composed of spherical droplets with identical diameters, Σ, $\tilde{Y}$, ρ, and $\bar{\rho}_l$ can be used to calculate the mean droplet number density (Eqn. 4.19) and Sauter Mean Diameter (SMD)(Eqn. 4.20) [23].

$$n = \frac{\bar{\rho}_l^2\bar{\Sigma}^3}{36\pi\bar{\rho}^2\tilde{Y}^2} \tag{4.19}$$

$$d_{32} = \frac{6\bar{\rho}\tilde{Y}}{\bar{\rho}_l\Sigma} \tag{4.20}$$

For a more in-depth description of the Σ balance equation, see Belhadef et al.'s 2012 paper [16].

4.5.1.2 Lagrangian Switch

The transition to the Lagrangian reference frame for the liquid in the dispersed region of the flow is optional. Indeed, the liquid and vapor penetration as well as the SMD and droplet density profile can be accurately captured in diesel sprays with the $\Sigma - Y$ model [162]. However, in certain instances the transition is certainly beneficial, such as in an impinging spray, where droplet trajectory crossing must be captured, or in combustion modeling, where more information than SMD and droplet density is required. Furthermore, because the Lagrangian approach is widely used, it offers many well-developed submodels [185]. For these reasons, continued development of the ELSA model is a worthwhile endeavor for both researchers and industry engineers.

The Lagrangian switch occurs in regions where the liquid density is low. Different researchers have used slightly different methods of defining this region. Blokkeel and Borghi, who first added the Lagrangian switch, initially proposed a criterion based upon the distance between drops in the cell and the mean size of the droplets [23]. They defined the transition region by $\frac{n^{1/3}}{d_{32}} > 2$, that is, where the average space between droplets is twice the mean droplet diameter. Since their work, the transition has consistently been based upon $\bar{Y}$, the liquid volume fraction, with Lebas et al. [98] using $\bar{Y} < 50\%$, Ning et al. [128] using $\bar{Y} < 10\%$, and Desportes et. al [44], Hoyas et al. [75], and Desantes et al. [38] using $\bar{Y} < 1\%$. To the knowledge of this author, nobody has explored the influence of adjusting the transition criteria.

Once a cell meets the requirements for transition, it will begin to switch liquid out of the Eulerian reference frame and into the Lagrangian. This occurs gradually, with only one parcel generated per transition cell per time step [38, 44, 74]. To implement the transition, the liquid velocity and liquid turbulence intensity must be extracted from the mean flow. This information is then used to generate the appropriate distribution of particles to represent the spray. Once this is determined, the liquid parcels are transitioned and placed randomly in the cell. For a more

thorough description of the transition process, including a derivation of the liquid velocity and liquid turbulence intensity terms mentioned above, see Blokkeel and Borghi's 2003 paper [23].

Due to the complexity of the liquid-gas interface in atomizing sprays, future developments to the Σ balance equation and to the Lagrangian transition criteria will be empirical in nature and will require thorough investigation alongside experimental drop size and drop velocity data.

4.5.1.3 Literature Review of the $\Sigma - Y$ Atomization Model

The model was introduced in 1999 by Vallet and Borghi [197]. In 2001 Vallet et al. provided an initial validation of this model against experimental results [196]. The near-field region SMD results did not match experimental data well. Overall, however, the results were encouraging, as they captured the spreading of the liquid and the evolution of SMD well.

In 2003, Blokkeel et al. coupled the Eulerian model with a Lagrangian droplet description for the dilute spray region [23, 24]. The combined model has since taken the name ELSA (Eulerian Lagrangian Spray Atomization). This model demonstrated good results, but the authors noted that future work needed to be done to develop a high-density ratio turbulence model, add vaporization effects, and account for compressibility.

Vaporization was then added to the ELSA model in 2005 by Lebas et al. [98]. This implementation performed well, accurately capturing spray atomization of heptane and dodecane into ambient densities ranging from 12-31 kg/m^3, ambient temperatures ranging from 800-1100 K, and injection pressures from 80-150 MPa.

In 2005 and 2006, the ELSA model was compared to a DNS with a CLSVOF ghost fluid method [11, 12, 118]. These DNS studies were questionable as they did not prove

mesh convergence. Still, the results showed that the representation of the initial liquid break-up and dispersion can be appropriately modeled as turbulent mixing.

In 2007, Ning et al. implemented a compressible ELSA model based upon an isentropic compressibility assumption in KIVA-3V and analyzed diesel injection under vaporizing conditions. In this study inlet conditions were generated through a three-dimensional HEM cavitation model [129]. Later, in 2009, they published more results with this model, making modifications to the turbulence model to account for compressibility and vortex stretching [128]. This implementation included an evaporation model that accounts for evaporation in the Eulerian liquid phase and it reproduced liquid and vapor penetration well at a variety of gas densities.

In 2007, Beheshti et al. [15] published results from a $\Sigma - Y$ model predicting air assisted atomization. The analysis matched results well both qualitatively and quantitatively for all varied parameters except liquid viscosity. Varied parameters included geometry, velocities and densities of liquid and gas, and surface tension.

Also in 2007, Demoulin et al. [35] developed a new high-density ratio turbulence model for ELSA to accurately model a coaxial injector. This model increased the turbulent flux due to Raleigh-Taylor instability induced by high-density fluctuations and turbulence.

In 2009, Lebas et al. [99] validated ELSA with a DNS that used the CLSVOF and ghost fluid methods. This study showed good results; in particular the ELSA model was able to accurately recover the influence of gas temperature changes.

In 2010, Desportes et al. [44] implemented the ELSA model into the commercial code, STAR-CD. Validation was conducted in vaporizing and non-vaporizing conditions in a constant-volume bomb.

In 2011, Hoyas et al. [75] conducted a mesh independence study on the ELSA model in a 2D simulation, which showed that 5 cells across the nozzle radius was adequate. They also experimented with tuning the $C_{\epsilon 1}$ turbulence model coefficient

and proved that a value of 1.52 provided the best results. The standard $C_{\epsilon 1}$ value is 1.44 and the typical value used in round jet sprays is 1.6 as suggested by Pope [150].

In 2012, Trask et al. [192] implemented a compressible $\Sigma - Y$ model on a gas-centered, swirl-coaxial fuel injector. Entrainment rate was modified by altering the Schmidt number and accurate results were predicted over a wide range of momentum flux ratios.

Also in 2012, Belhadef and Vallet et al. [16] implemented the $\Sigma - Y$ model on a pressure swirl atomizer that is commonly used in the agricultural industry. SMD predictions were found in good agreement with PDA experiments.

In 2013, García-Oliver et al. [64] validated a compressible formulation of the $\Sigma - Y$ model using high speed imaging, PDPA, and Rayleigh-scattering measurements. Diesel sprays at a variety of ambient densities and pressures were analyzed under both vaporizing and non-vaporizing conditions. Agreement was very good especially under medium and high ambient gas density conditions. This study is described in more detail in section 6.1

In the 2014 study by Salvador et al. [162], the effect of the turbulence model and the inlet boundary conditions on diesel spray behavior was examined using a $\Sigma - Y$ model that was modified to handle internal flow. The modifications included the use of the common pressure equation, the addition of compressibility, and the use of the PIMPLE algorithm rather than the PISO algorithm. The geometry used was an axisymmetric single-hole nozzle, and the computational domain was two-dimensional. As the $\Sigma - Y$ approach considers atomization as turbulent mixing, it is not surprising that Salvador et al. observed significantly different results between turbulence models. At 1 ms past start of injection, the spray penetration varied from 32 mm to well over 40 mm, and the spray angle varied from 7° to 23°, with the experimental penetration being 30 mm and the spray angle being 16° at the same point in time.

Similarly, Desantes et al. [39] implemented a $\Sigma - Y$ model that uses the common pressure equation to analyze internal flow in addition to the first few millimeters of external flow. The study was conducted on three different geometries, and internal flow coefficients were predicted well for all geometries at a variety of injection rates. The authors commented that more work is required to improve the near-field spray structure. Additionally, they mentioned that their model was unstable unless the nozzle started full of fuel.

Xue et al. [210] implemented a $\Sigma - Y$ model on top of a VOF method in the CONVERGE CFD software. This model was used to analyze injection through a single-hole, Spray A injector. The simulation was three-dimensional and the conditions were non-evaporating. The model predicted rate of injection characteristics and near-field fuel distribution well. The influence of the nozzle asymmetry on fuel distribution was captured. Results were shown to improve with the mesh resolution, indicating that mesh convergence was perhaps not reached. The round jet correction improved the results significantly and Schmidt number was shown to have little influence on the simulation. In this study the $\Sigma - Y$/VOF model was also compared to a traditional EL model. The Eulerian model was in better agreement both qualitatively and quantitatively with the experimental data than the EL model.

In the 2016 work by Desantes et al. [36], the $\Sigma - Y$ atomization model was further validated for near-field internal structure and the influence of coupling internal nozzle flow simulations with the downstream spray was investigated. This work is described in more detail in section 6.2.

In the 2016 work by Pandel et al. [138], a construction of the $\Sigma - Y$ model built around the IMEX-RK3 algorithm is described. Two benefits of using this construction are presented. First, it is easier to maintain consistency between hydrodynamic and thermodynamic variables. Second, this construction results in great parallel scal-

ability, with a 34x speedup when compared with the conventional PISO construction on 256 processors.

4.6 Conclusions

This chapter described the common approaches used in CFD modeling of atomizing sprays. This includes high-fidelity sharp interface DNS and LES, the LE approach, the EE approach, the Eulerian quadrature-based moment approach, and the diffuse interface single-field Eulerian approach.

Starting with the sharp interface high-fidelity approach, it was shown that a true DNS of a highly atomizing spray is not attainable. However, high-fidelity DNS and LES models still provide value in their use in validating engineering level models under more moderate conditions or on smaller scales. Additionally, they provide insight into the underlying physics behind the atomization process.

The LE approach is popular and offers accurate predictions of sprays at reasonable computational costs. However, the Lagrangian description of the liquid does not lend itself to easily modeling the dense region of the spray. This leads to questions about how to properly initialize the model as well as numerical stability problems and mesh dependency issues.

The EE approach does not suffer from these issues in the dense region. The downside of this model, as compared to single-field Eulerian modeling, is the computational cost; EE requires the solution of two coupled sets of conservation equations. While this is necessary in some instances, it doesn't appear to be so for highly atomizing sprays [33].

The diffuse interface single field Eulerian approach has proven suitable for internal, near-field, and far-field multiphase simulations in many DI applications. The $\Sigma - Y$ model is included in this approach, accurately characterizing highly atomizing sprays by modeling atomization as turbulent mixing and the evolution of the multiphase

interface with the Σ transport equation. This model has received a lot of attention in recent years and there are currently multiple groups using it in some form. The recent implementation of $\Sigma - Y$ for internal/external flow is exciting because it allows for the effects of the nozzle on the spray to naturally be captured.

CHAPTER 5

DEVELOPMENTS AND ADVANCEMENTS

5.1 A Realizable Constraint on Turbulent Mixing

5.1.1 Description

When an intact liquid jet first contacts gas near the nozzle exit, the sharp liquid/gas interface results in a nearly infinite gradient of the liquid mass fraction field. When using the standard turbulent gradient flux model to diffuse the liquid mass in an Eulerian spray model, this can produce unbounded, unrealistic mixing velocities. This unbounded mixing may have only modest impacts on overall model accuracy, but it causes local errors that have significant stability implications. For this reason, a constraint on the mixing velocity has been developed.

For multiphase flows with turbulent driven mixing, it is logical that the slip velocity should not exceed the magnitude of the turbulent velocity fluctuations,

$$u_i|_l - u_i|_g \leq u'_i \tag{5.1}$$

Using the expression for slip velocity, Eq. (4.9), with the turbulent velocity fluctuation extracted from the Reynolds stress tensor, the following constraint is derived:

$$\frac{1}{\tilde{Y}\left(1-\tilde{Y}\right)} \cdot \widetilde{u'_i Y'} \leq \sqrt{R_{ii}/\rho} \tag{5.2}$$

Note that i in Eqn. 5.2 is the free index, so R_{ii} does not indicate summation. When using an isotropic turbulence model, this simplifies to:

$$\frac{1}{\tilde{Y}\left(1-\tilde{Y}\right)} \cdot \widetilde{u'_i Y'} \leq \sqrt{\frac{2}{3}k} \tag{5.3}$$

This can then be imposed on the turbulent diffusion liquid flux term by combining Eq. (5.3) and Eq. (4.10). The result yields a lower bound to the Schmidt number which can be seen below in Eq. (5.4).

$$Sc \geq \frac{\mu_t}{\bar{\rho}\sqrt{2/3k}\tilde{Y}(1-\tilde{Y})}\frac{\partial \tilde{Y}}{\partial x_i} \tag{5.4}$$

The implementation is then achieved by making the Schmidt number in Eq. (4.10) a field and setting its value to whichever is greater, the lower bound prescribed by Eq. (5.4) or the conventional Schmidt number of 0.9. This realizable constraint on the Schmidt number prevents the turbulent liquid diffusion flux from exceeding the magnitude of the turbulent fluctuations.

5.1.2 Evaluation

The realizable Schmidt number was evaluated and implemented in an article by Desantes et al. [36]. Here we conducted an evaluation of the realizable Schmidt number with 2D simulations of the ECN spray A condition. Two cases were run, one with a constant Schmidt number of 0.9 and one with the realizable Schmidt number. In Fig. 5.1, in order to help to understand where the constraint is manifest, a snapshot of the realizable Schmidt number is shown, capturing the tip of the nozzle and the near-field region of the spray. It can be observed that the constraint takes effect on the border of the intact core of the liquid jet.

In Fig. 5.2, the model predicted results of projected mass density are compared against X-ray radiography measurements conducted at Argonne National Laboratory.

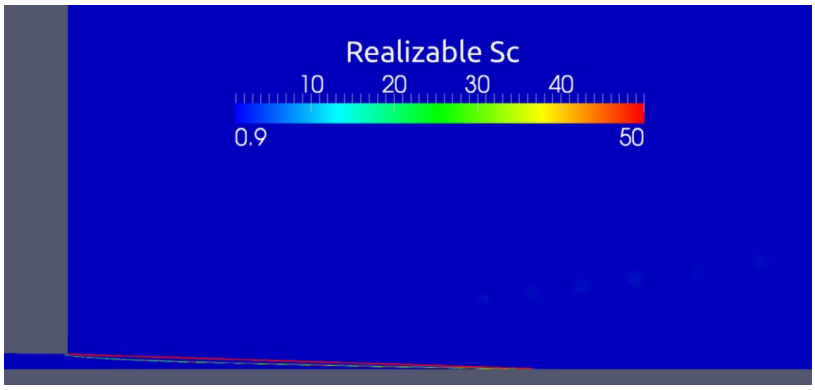

Figure 5.1: The realizable Schmidt number field at 500 μs after SOI.

The variable used for comparison is the projected mass density of the fuel, which is calculated by a line-of-sight integration along the X-ray beam [89, 149]. A similar procedure is replicated with the data from simulations to enable fair comparisons against experiments. This comparison is made at 0.1 mm, 2 mm, and 6 mm downstream of the nozzle exit. The results are nearly identical and only at 0.1 mm can some insignificant differences be noticed.

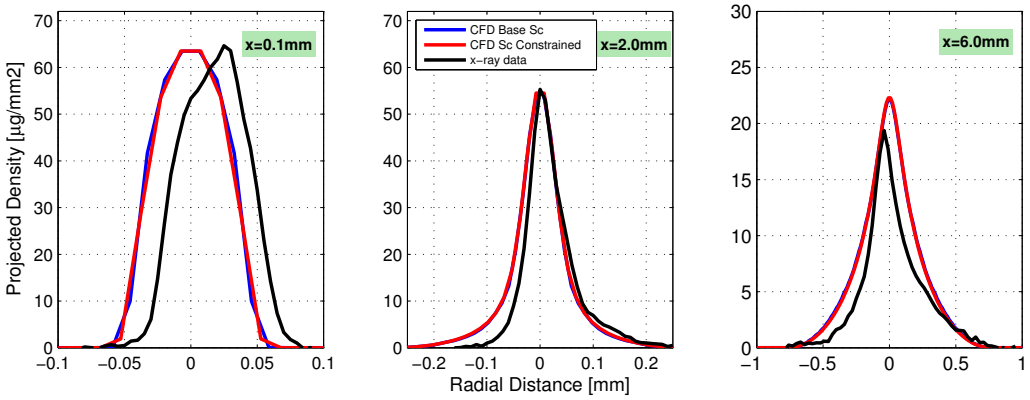

Figure 5.2: Computed and measured profiles of projected mass density [μg/mm^2] 500 μs after SOI at axial locations of 0.1 mm, 2 mm, and 6 mm downstream of the nozzle exit.

Another useful quantity obtained from the X-ray radiography measurements is the transverse integrated mass (TIM), which is obtained from the integral of the projected density across the transverse position at a particular axial location [88]. In

Fig. 5.3, it is shown that the constrained case has a slightly lower TIM value right at the nozzle exit and again in the far-field, due to the limited liquid mass diffusion.

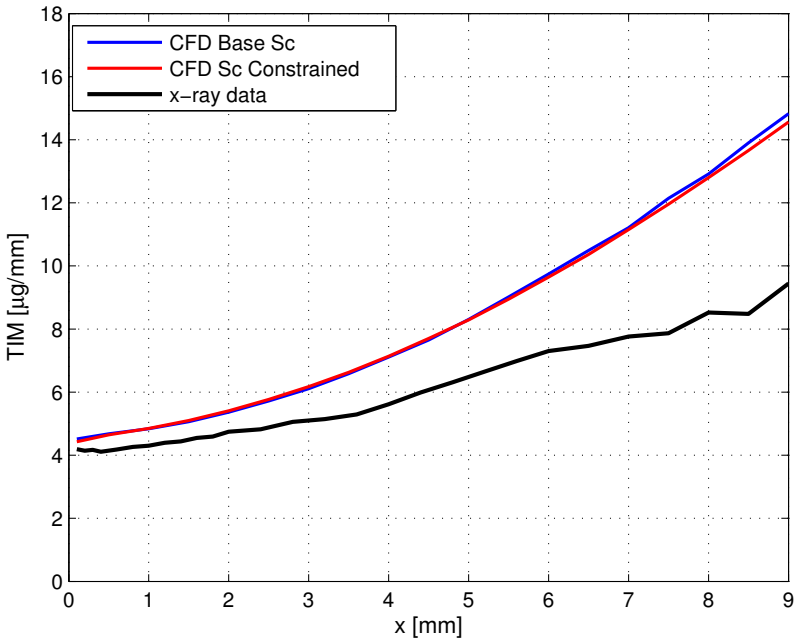

Figure 5.3: Computed and measured transverse integrated mass (TIM) along the axis at 500 μs after SOI.

Overall, a good agreement with experimental data is provided independently of which Schmidt number is used. No great differences could be detected between the predicted values of the simulations, as can be seen in the projected density profiles as well as the TIM profiles. The remarkable utility of this constrained formulation is that it improves the numerical stability, in this case allowing the simulation to run with a Courant number four times greater than the reference case.

5.2 Modeling Phase Change

There are two ways in which fuel vapor can be generated in DI systems. The first is through caviation or flash-boiling. These occur when the local pressure drops below the vapor pressure of the fluid. Here the latent heat of vaporization is supplied by sensible heat, which is already available in the fuel. The second way that it can

occur is through vaporization, when the downstream ambient conditions are hot and the latent heat of vaporization is provided by the ambient gas. Phase change models for both of these mechanisms have been developed and are described below.

5.2.1 Locally Homogeneous Flow

A vaporization model was added to the $\Sigma - Y$ solver in the work of García-Oliver et al. [64]. Here we used a Locally Homogeneous Flow (LHF) approach [53]. The implementation is described below.

A transport equation for fuel vapor mass fraction, Eqn. 5.5, is added to the system.

$$\frac{\partial \bar{\rho}\tilde{Y}_v}{\partial t} + \frac{\partial \bar{\rho}\tilde{u}_i\tilde{Y}_v}{\partial x_i} = -\frac{\partial \bar{\rho}\widetilde{u'_i Y'_v}}{\partial x_i} + \bar{\rho}\tilde{\dot{Y}}_{vap} \tag{5.5}$$

In conjunction with this, a vaporization sink term is added to the liquid mass transport equation, as seen in Eqn. 5.6.

$$\frac{\partial \bar{\rho}\tilde{Y}}{\partial t} + \frac{\partial \bar{\rho}\tilde{u}_i\tilde{Y}}{\partial x_i} = -\frac{\partial \bar{\rho}\widetilde{u'_i Y'}}{\partial x_i} - \bar{\rho}\tilde{\dot{Y}}_{vap} \tag{5.6}$$

The effects of the vaporization sink term on Σ are accounted for through the $\bar{\dot{\Sigma}}_{vap}$ term in Eqn. 5.7. This equation is more fully described in section 4.5.1.1.

$$\frac{\partial \overline{\Sigma}}{\partial t} + \frac{\partial \tilde{u}_j\overline{\Sigma}}{\partial x_j} = \frac{\partial}{\partial x_j}\left(D_\Sigma \frac{\partial \overline{\Sigma}}{\partial x_j}\right) + (A + a)\,\overline{\Sigma} - V_s\overline{\Sigma}^2 - \bar{\dot{\Sigma}}_{vap} \tag{5.7}$$

The definition of $\bar{\dot{\Sigma}}_{vap}$ comes from [99] and is seen in Eqn. 5.8.

$$\bar{\dot{\Sigma}}_{vap} = \frac{2}{3}\frac{\Sigma^2}{\bar{\rho}\tilde{Y}_l}\dot{m}_{l\to v} \tag{5.8}$$

The value of $\dot{m}_{l\to v}$ is related to the vapor source term, $\tilde{\dot{Y}}_{vap}$, through the following equation.

$$\dot{m}_{l\to v} = \frac{\bar{\rho}\tilde{\dot{Y}}_{vap}}{\Sigma} \tag{5.9}$$

The vapor source term is calculated through

$$\tilde{\dot{Y}}_{vap} = \frac{Y_{v,sat} - \tilde{Y}_v}{\tau_{evap}} \tag{5.10}$$

where $\tilde{Y}_v$ is the local vapor fuel mass fraction, $Y_{v,sat}$ is the value of vapor fuel mass fraction under adiabatic saturation conditions, and τ_{evap} is a short relaxation timescale meant to keep the system at equilibrium.

Finally, state relationships are applied to describe the spray thermodynamic conditions under the assumption of local thermodynamic equilibrium. The enthalpy balance for the mixture is expressed in terms of an adiabatic mixing process:

$$h\left(T\right) = Y \cdot h_{f,l}\left(T\right) + Y_v \cdot h_{f,v}\left(T\right) + \left(1 - Y - Y_v\right) \cdot h_a\left(T\right) \tag{5.11}$$

where $h_{f,l}$ is the liquid fuel enthalpy, $h_{f,v}$ is the fuel vapor enthalpy, and h_a is the ambient gas enthalpy. Together with the thermodynamic equilibrium assumption, local temperature and composition can be derived [141], from which $Y_{v,sat}$ is fed into the vaporization term of the transport equation.

5.2.2 Homogeneous Relaxation Model

Vapor generation through cavitation and flash-boiling is well approximated by the homogeneous relaxation model (HRM). This model was developed in 1990 by Bilicki and Kestin [20]. They sought to capture the variability in the vapor generation and condensation rate by the addition of a partial differential equation to the Homogeneous Equilibrium Model (HEM). This additional partial differential equation governs the local and instantaneous rate that the dryness fraction tends toward its equilibrium value, taking the form

$$\frac{Dx}{Dt} = \frac{\bar{x} - x}{\Theta} \tag{5.12}$$

where x is the quality, $\bar{x}$ is the equilibrium quality, and Θ is the timescale. The equilibrium quality, given by Eqn. 5.13 is determined by the enthalpy and the saturated liquid and saturated vapor enthalpies at the local pressure.

$$\bar{x} = \frac{h - h_l}{h_v - h_l} \tag{5.13}$$

As per the work of Downar-Zapolski et al. [45], the timescale, Θ, is determined by an empirical fit to experimental data of flash boiling water in pipes. For upstream pressures above 1 MPa, the empirical fit takes the form seen in Eqn. 5.14.

$$\Theta = \Theta_0 \alpha^a \phi^b \tag{5.14}$$

Where $\Theta_0 = 3.84 \cdot 10^{-7}$[s], $a = -0.54$, $b = -1.76$, and ϕ is a dimensionless pressure defined by Eqn. 5.15.

$$\phi = \left| \frac{P_s - p}{p_c - P_s} \right| \tag{5.15}$$

Here p_c is the critical pressure of the fluid. And the void fraction, α, is determined by the density and the saturated liquid and vapor densities, as seen in Eqn. 5.16.

$$\alpha = \frac{\rho_l - \rho}{\rho_l - \rho_v} \tag{5.16}$$

While HRM was originally developed for one-dimensional analysis, it was extended to a two-dimensional CFD model in 1997 by Schmidt [165, 166]. In 2010, it was extended to a three-dimensional CFD model by Schmidt et al. [167]. The introduction of variable rate phase change required a method for connecting predicted phase change with conservation of mass and momentum. This can be done using the chain rule as shown in Eqn. (5.17). This allows for the pressure to respond to compressibility,

density change from phase change, and density change from turbulent mixing with the non-condensable gas.

$$\begin{aligned}\frac{D\rho}{Dt} = &\left.\frac{\partial\rho}{\partial p}\right|_{x,h,y}\frac{Dp}{Dt} + \left.\frac{\partial\rho}{\partial x}\right|_{p,h,y}\frac{Dx}{Dt} \\ &+\left.\frac{\partial\rho}{\partial h}\right|_{p,x,y}\frac{Dh}{Dt} + \left.\frac{\partial\rho}{\partial y}\right|_{p,h,x}\frac{Dy}{Dt}\end{aligned} \tag{5.17}$$

The HRM model in diffuse interface Eulerian solvers has been used and validated in a wide variety of applications, including a condensing injector [31], flash boiling in superheated jet fuel [100], pressure swirl injectors [125], internal cavitating flow through single and multi-hole diesel nozzles [9, 47, 210, 215], as well as flash-boiling GDI flow [121, 160, 161, 184].

5.3 Solver Consistency

It can be difficult to maintain consistency between hydrodynamic and thermodynamic variables when modeling compressible flows using a segregated solution procedure. Multiple approaches can be taken to help address this challenge and some of them will be described in this section.

First, when multiple transport equations exist, it is important that the same interpolation scheme, with identical weighting, be used by each of the variables. In OpenFOAM, this tool is called multivariate selection. When an inconsistency between the density field and the equation of state was discovered in our $\Sigma - Y$ model, this was the first tool that we utilized. It was able to help our solver maintain consistency up to machine precision for some flows, however, in many circumstances the inconsistency would persist.

For the work by García-Oliver et al. [64], we added a penalty term to the pressure equation used by Trask et al. [192] (Eqn. 4.17. This penalty term worked to relax

the density field towards the equation of state density. The pressure equation with the penalty function is shown in Eqn. 5.18.

$$-\bar{\rho}\nabla\cdot(\mathbf{U}_p)_f = \frac{\partial\bar{\rho}}{\partial\tilde{Y}}\frac{D\tilde{Y}}{Dt} + \frac{\partial\bar{\rho}}{\partial\tilde{Y}_{vap}}\frac{D\tilde{Y}_{vap}}{Dt} + \frac{\partial\bar{\rho}}{\partial\bar{p}}\frac{D\bar{p}}{Dt} + \frac{\partial\bar{\rho}}{\partial\tilde{T}}\frac{D\tilde{T}}{Dt} + \frac{\rho_{eos}-\bar{\rho}}{C_{relax}} \tag{5.18}$$

Here, the C_{relax} term was a tunable constant which dictated how hard the push towards consistency would be. This approach worked well here and the ability of this term to correct the discrepancy can be observed in Fig. 5.4, where the density is compared with the equation of state density for the $\Sigma - Y$ solver with and without the penalty term.

This penalty function approach was an ad-hoc fix, intended only to correct small discrepancies. Further analysis of the problem revealed that the root cause of the inconsistency was simply the segregated solution procedure in conjunction with an overdetermined system of equations. The solver contained a transport equation for density (continuity), a transport equation for the liquid mass fraction, a pressure equation, and an equation of state relating the liquid mass fraction to the density, Eqn. 4.11. This meant that even when the solver was converging to a solution, there was no guarantee that the solution would be mathematically consistent with itself. Furthermore, in some configurations, this inconsistency would cause stability problems, with the pressure equation struggling to converge to a solution with the inconsistent variables.

Two apparent fixes are possible for such a problem. The first is removing an equation, for instance, the Y transport equation. This approach was taken with a successful result. In the no$-Y$ implementation of $\Sigma-Y$, the influence of the turbulent liquid diffusion flux term is still captured through the chain rule implementation of the total derivative of density in the pressure equation,

$$\bar{\rho}\nabla\cdot(\mathbf{U}_p)_f = -\frac{\mathrm{D}\bar{\rho}}{\mathrm{D}t} = -\frac{\partial\bar{\rho}}{\partial\tilde{Y}}\frac{\mathrm{D}\tilde{Y}}{\mathrm{D}t} - \frac{\partial\bar{\rho}}{\partial\bar{p}}\frac{\mathrm{D}\bar{p}}{\mathrm{D}t} - \frac{\partial\bar{\rho}}{\partial\tilde{T}}\frac{\mathrm{D}\tilde{T}}{\mathrm{D}t} \tag{5.19}$$

where

$$\bar{\rho}\frac{\mathrm{D}\tilde{Y}}{\mathrm{D}t} = \frac{\mathrm{D}\bar{\rho}\tilde{Y}}{\mathrm{D}t} - \tilde{Y}\frac{\mathrm{D}\bar{\rho}}{\mathrm{D}t} \tag{5.20}$$

and

$$\frac{\partial\bar{\rho}\tilde{Y}}{\partial t} + \frac{\partial\bar{\rho}\tilde{u}_i\tilde{Y}}{\partial x_i} = -\frac{\partial\bar{\rho}\widetilde{u'_i Y'}}{\partial x_i} \tag{5.21}$$

combine together and yield,

$$\bar{\rho}\frac{\mathrm{D}\tilde{Y}}{\mathrm{D}t} = -\frac{\partial\bar{\rho}\widetilde{u'_i Y'}}{\partial x_i} \tag{5.22}$$

Here the value of Eqn. 5.22 is explicitly set, typically with a Fickian diffusion model. This restructured solver behaves similar to the previous implementation, except without the mathematical inconsistency. It is currently being used to model impinging jet sprays.

The problem also could be addressed simply through correcting the inconsistency at every time step, and thus preventing it from ever developing into anything of significance. In the 2015 work by Battistoni et al. [8], a similar inconsistency was discovered in their Eulerian based HRM solver, and this type of explicit correction to the inconsistency was adopted.

Alternatively, these difficulties can be avoided for high Mach number flows by using a coupled, density based algorithm. This was done by Pandal et al. in our 2016 IJMF work [138]. Here we implemented the $\Sigma - Y$ model in an IMEX-RK3 algorithm. This approach offers several advantages over the previous segregated PISO construction from Trask et al. [192] and García-Oliver et al. [64]. For instance, it is easier to maintain consistency in the coupled approach, as seen in Fig. 5.4. Also, solving for pressure explicitly improved stability, and greatly improved parallel scalability, as seen in Fig. 5.5. The benefit of improved scalability is very significant, allowing for these types of models to solve problems of much greater magnitude through high performance computing.

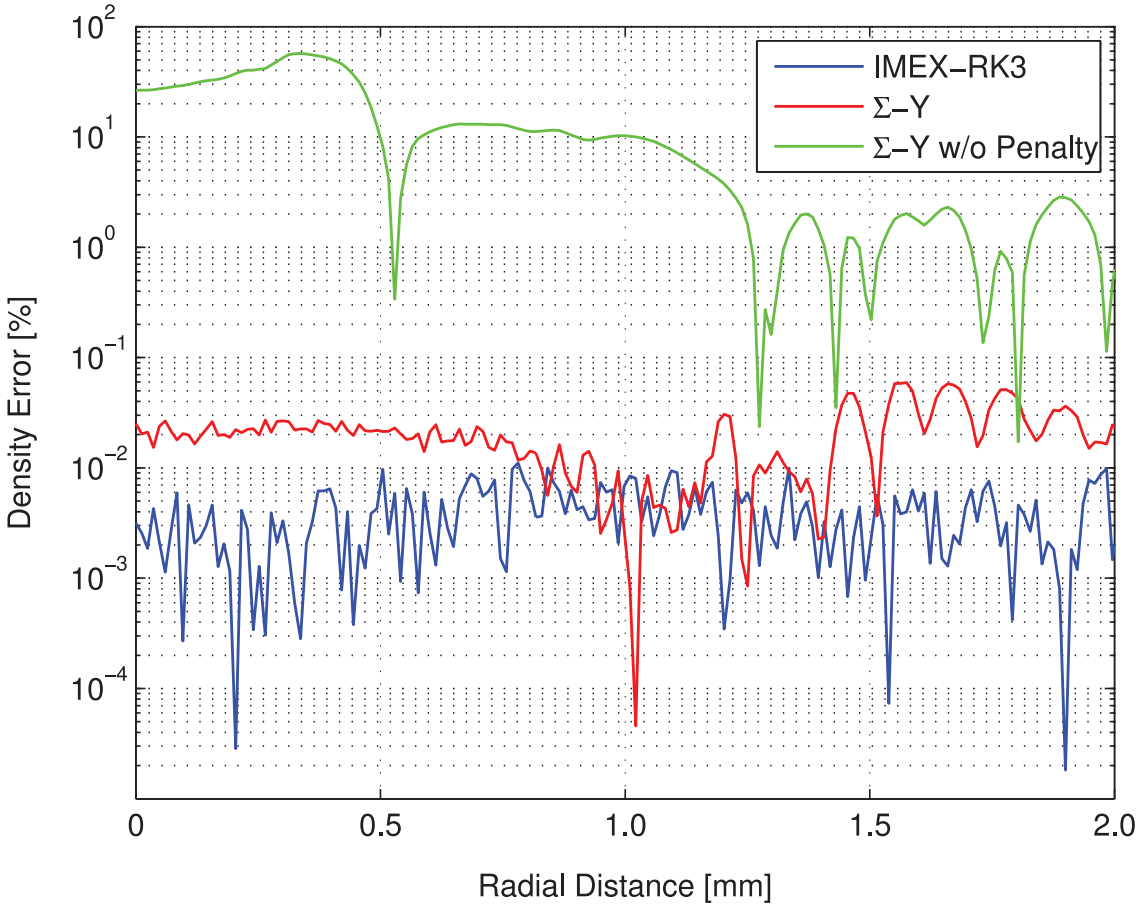

Figure 5.4: Assessment of consistency between the ρ and ρ_{eos}. The three methods correspond to the work of Pandal et al. [138], García-Oliver et al. [64], and Trask et al. [192], respectively.

5.4 Transient Needle Motion

The Eulerian HRMFoam solver developed by our group is built upon the foam-extend open source CFD libraries. These libraries provide a tremendous amount of utility to the user, including access to a range of dynamic mesh functionality. HRMFoam had previously been modified to work with these dynamic mesh libraries, allowing for the modeling of transient needle motion during an injection event.

This was demonstrated in 2012 by Neroorkar et al. [126]. Here, flow through a multi-hole diesel nozzle was modeled with a laminar, incompressible simulation using slip walls and upwinding convection schemes. Internal mesh motion was handled

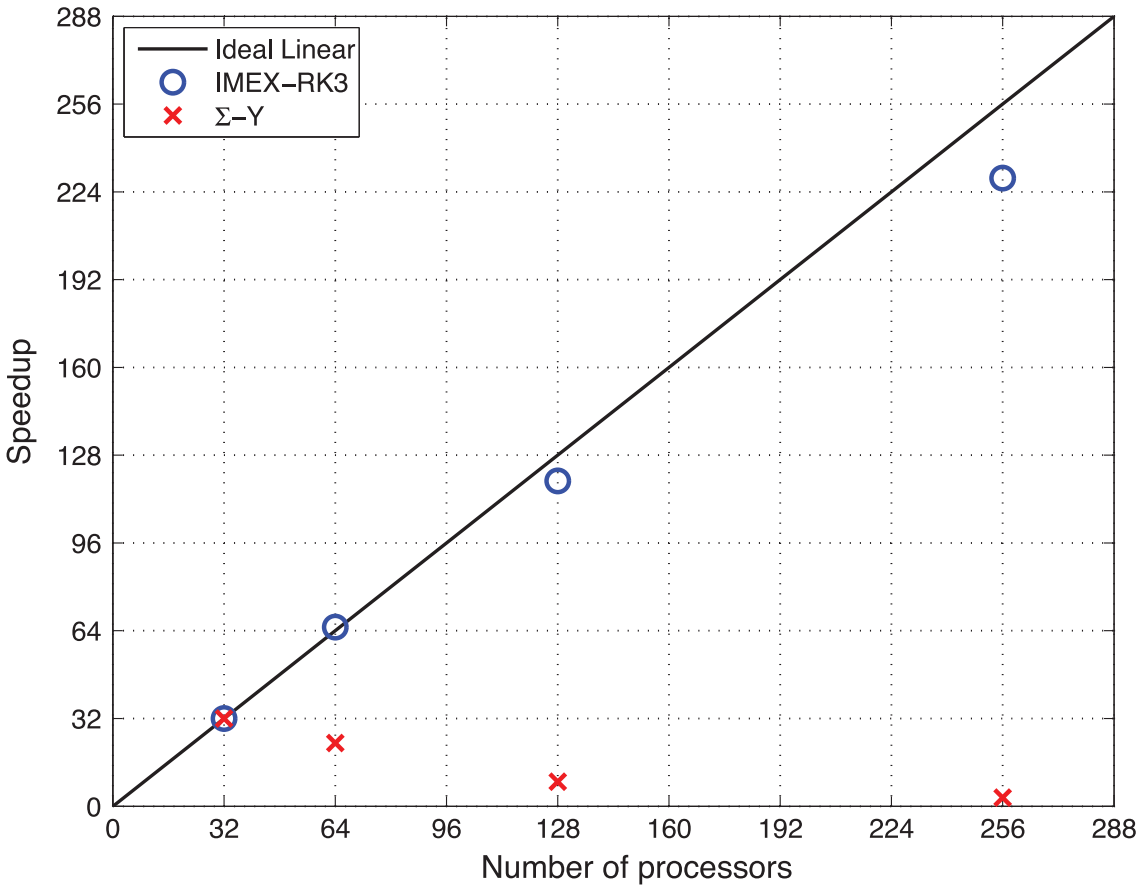

Figure 5.5: Scalability comparison of PISO based $\Sigma - Y$ and the IMEX-RK3 implementation.

with layer addition and removal and without uniform layer stretching/squeezing. The minimum needle lift was set to 25 μm, and computed rate of injection profiles were compared with experimental data. The computational results predicted a significant influence of needle position on internal flow structure, with low needle lift resulting in swirling flow within the nozzle sac. In addition, it was observed that hole-to-hole variation in flow rate was most significant at low needle lift positions.

The mesh motion implementation in HRMFoam, however, still required more work. For instance, when operating with the compressible implementation of the solver, artifacts of the mesh motion were produced in the flow field. In addition to this, the solver was unable to run in parallel with mesh motion routines that utilized

uniform layer motion or topology change. These issues have been addressed and their solutions will be discussed within this section. Furthermore, mesh motion best practices will be covered.

5.4.1 Dynamic Mesh Motion in the FVM

When structuring a transport equation in the finite volume method (FVM), the motion of faces on each volume must be considered. Eqn. 5.23 is the general form of a transport equation for a scalar field γ constructed using the Reynolds transport theorem.

$$\frac{d}{dt}\int_V \gamma \mathrm{d}V + \oint_S \gamma(\mathbf{u_a} - \mathbf{u_m}) \cdot \hat{\mathbf{n}}\, \mathrm{d}S = \oint_S \mathbf{q}_\gamma \cdot \hat{\mathbf{n}}\, \mathrm{d}S + \int_V s(\gamma)\mathrm{d}V \tag{5.23}$$

Here, $\mathbf{u_m}$ is the face velocity and $\mathbf{u_a}$ is the absolute velocity. The first term represents the time rate of change of γ in any given volume. The second and third terms represent the convective and diffusive transport of γ, respectively. The final term represents a source/sink term. The relationship between the volume rate of change and the integral of the face velocity must satisfy the space conservation law, Eqn. 5.24 [81].

$$\frac{d}{dt}\int_V \mathrm{d}V - \oint_S \mathbf{u_m} \cdot \hat{\mathbf{n}}\, \mathrm{d}S = 0 \tag{5.24}$$

The first step in adding a dynamic mesh capability to a solver, therefore, is to restructure each transport equation to account for the mesh velocity in the convective terms. This had already been done in HRMFoam. The remaining problem in the algorithm was related to a discretization mistake which will be described in the next section

5.4.2 Improving the Dynamic Mesh Implementation in HRMFoam

5.4.2.1 Motion Artifact

An artifact of the mesh motion was visible in the flow field; the expanding cells had a very slight increase in density, and after layer addition or removal a significant error in density was generated in the cells involved in the topology change. This can be seen in the Fig. 5.6. The mesh motion artifact was the result of error introduced due to the improper discretization of a total derivative term in the pressure equation.

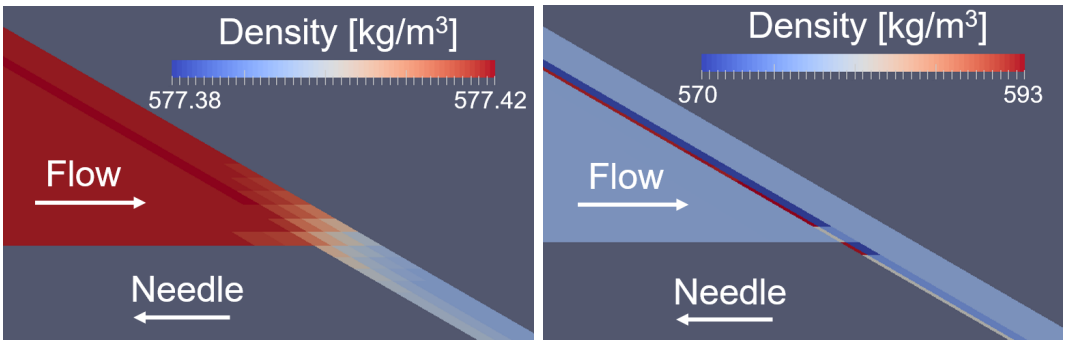

Figure 5.6: Artifact of mesh motion seen in flow field of test case. Left image is before layer addition and right is after layer addition.

To explain this error, lets first look at the definition of the total derivative using continuous math. For a scalar field $\gamma(x,t)$ it is as follows,

$$\frac{D\gamma}{Dt} = \frac{\partial\gamma}{\partial t} + \mathbf{u}\cdot\nabla\gamma \tag{5.25}$$

This equation can also be rewritten as,

$$\frac{D\gamma}{Dt} = \frac{\partial\gamma}{\partial t} + \nabla\cdot(\gamma\mathbf{u}) - \gamma(\nabla\cdot\mathbf{u}) \tag{5.26}$$

Moving from the continuous form of the total derivative to the control volume form requires that the relative velocity of the control volume be accounted for. This relative velocity can be different for each surface of the control volume, depending on the mesh

velocity of the cell faces. It, therefore, is inherently different from the velocity term used in Eqn. 5.26. To properly account for the change in γ due to a change in the control volume, the mesh motion should be considered in only the second term of Eqn. 5.26. It, however, was accounted for in both terms as shown in Eqn. 5.27.

$$\frac{D\gamma}{Dt} = \frac{d}{dt}\int_V \gamma \mathrm{d}V + \oint_S \gamma(\mathbf{u_a} - \mathbf{u_m}) \cdot \hat{\mathbf{n}}\, \mathrm{d}S - \gamma \oint_S (\mathbf{u_a} - \mathbf{u_m}) \cdot \hat{\mathbf{n}} \tag{5.27}$$

Here, the nature of the mistake is quite apparent. Consider, for example, a stationary flow where γ is uniform and constant but the mesh is moving. As per the space conservation law, Eqn. 5.24, it is easy to see that the volume change captured by the first two terms will balance out. The final term, however, also contains this mesh velocity, making it non-zero. In this form, therefore, γ is not being conserved.

The properly discretized total derivative takes the form seen in Eqn. 5.28. The interested reader can find a thorough derivation of the material derivative of a moving control volume in chapter one of [204].

$$\frac{D\gamma}{Dt} = \frac{d}{dt}\int_V \gamma \mathrm{d}V + \oint_S \gamma(\mathbf{u_a} - \mathbf{u_m}) \cdot \hat{\mathbf{n}}\, \mathrm{d}S - \gamma \oint_S (\mathbf{u_a}) \cdot \hat{\mathbf{n}} \tag{5.28}$$

With this form of the total derivative, the mesh motion artifacts were no longer observed, as seen in Fig. 5.7

5.4.2.2 Flux Correction

A flux correction step was added to the HRMFoam solver to ensure that non-conservative fluxes do not adversely affect the prediction step of the SIMPLE algorithm. This correction step is common in dynamic mesh solvers, and it occurs whenever the topology of the mesh changes.

After a topology change, cell centered values are mapped from the old mesh to the new one. This mapping process cannot be done for fluxes, however, as they are

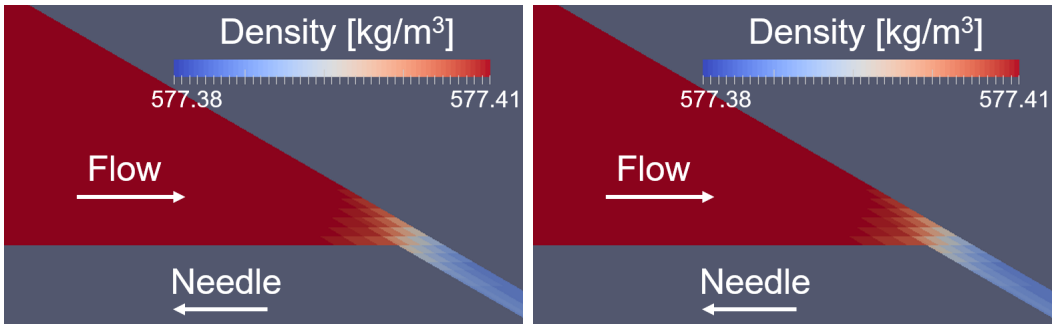

Figure 5.7: No artifact of mesh motion seen prior to layer addition (left) or after (right).

stored on cell faces. The solution includes first calculating the divergence of the flux field prior to the topology change. After the topology change, this cell-centered value is then mapped to the new mesh and used in the Laplacian equation shown in Eqn. 5.29.

$$\nabla \cdot \frac{1}{a_p} \nabla P_{corr} = \nabla \cdot \phi_0 - (\nabla \cdot \phi)_c \tag{5.29}$$

Here ϕ_0 is the uncorrected face flux on the new mesh, which is initialized based upon the mapped cell-centered velocity field. The $(\nabla \cdot \phi)_c$ term is the cell-centered pre-topology change divergence, the P_{corr} is a dummy pressure field which is implicitly solved in this equation, and a_p represents the diagonal coefficients of the matrix, as further described in [81].

Once this equation is solved, the face flux can then be corrected as per Eqn. 5.30.

$$\phi = \phi_0 - \frac{1}{a_p} \nabla P_{corr} \tag{5.30}$$

The resultant face flux, ϕ, will then have the same divergence as that of the flux pre-topology change.

5.4.2.3 Running in Parallel with Topology Change

There was a problem with the HRMFoam solver which caused parallel simulations to crash. Running a parallel test case in a debugger revealed that the crash was

occurring during the process of mapping several thermodynamic fields from the old mesh to the mesh with a new topology. Not all of the thermodynamic fields declared in the abstract base class inherited by our thermodynamic class were actively used by our solver. This caused the child processes to be unable to find these variables during the map fields routine, and this resulted in the program to crashing. The solution was to use the thermodynamic class to handle all of the fields defined by the abstract base it inherits. This was not a big code change; it involved relocating when and where various thermodynamic fields were initialized and calculated. Fixing this allowed for the add/remove layer mesh motion library designed for HRMFoam to run in parallel.

5.4.3 Mesh Motion Approaches

5.4.3.1 Laplacian Smoothing

One common method used to obtain a solution for internal mesh motion is to solve Laplace's equation for the mesh. This is easy to set up, provides a good solution for moderate to small deformations, and works with a structured or unstructured grid. Laplacian smoothing was the approach taken in the ECN spray G study conducted in section 7.2.

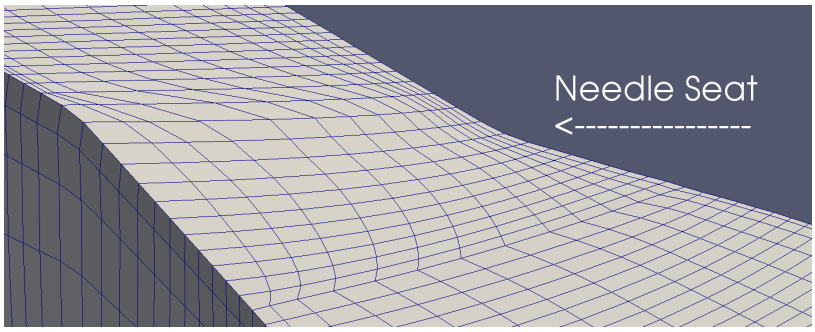

Figure 5.8: Needle seat region of diesel injector after lifting needle 200 μm with Laplacian smoothing.

This approach has two drawbacks. First, the cost of the Laplacian solve is not trivial, especially for large meshes. Thus, it adds to the computational cost of the solution. Second, it does not work for large deformations. For example, consider Fig. 5.8. Here Laplacian motion was used to lift the spray D needle, and it can be seen that the mesh quality is starting to deteriorate after only 200 μm of lift.

5.4.3.2 Uniform Layer Motion

An alternative to Laplacian motion is to uniformly stretch and squeeze cell layers which are adjacent to the moving boundary. The computational cost of this is low, as motion is based upon a simple mathematical expression. This method can also handle very large deformations. As seen in Fig. 5.8, the uniform motion results in very uniform cell layers. Cell aspect ratio, rather than mesh quality, therefore, becomes the limiting factor when using this approach.

One moderate drawback to uniform layer motion is that it only works with uniform, structured layers. While many meshing tools can accommodate this limitation, it does complicate the meshing process.

5.4.3.3 Layer Addition/Removal

Cases which require large deformations must address the problem of cell aspect ratios becoming large. This can be done through the addition or removal of cell layers.

While this approach has the same structured grid limitation, if the case starts with the lifting process and the addition of layers, the resulting mesh will inherently be structured and readily available for later removal. Layer addition/removal methods are commonly used for internal engine simulations where large deformations occur due to the motion of the piston. They are well suited for the internal nozzle simulations of diesel injectors where needle lifts can be as large as 500 μm [1].

The uniform layer motion and layer addition/removal methods work well together. Both require uniform layers, and both have similar code structure demands and re-

quirements. Coupling these methods also provides the added benefit of distributing and minimizing the errors associated with mapping the flow solution from one topology to another.

5.4.4 Mesh Motion Best Practices

First, it is best to initially mesh the geometry with the needle at a low lift position. This is because the surface normal of a fuel injector needle is not typically parallel to the direction of needle motion. For this reason, lowering the needle on a mesh generated at full lift will quickly result in highly skewed cells. To help visualize this best-practice, see Fig. 5.9.

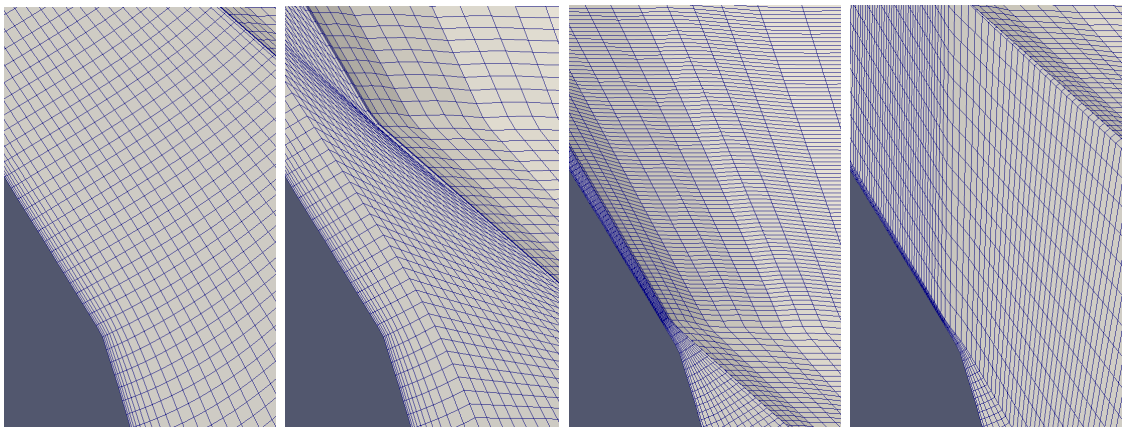

Figure 5.9: Seat region mesh of diesel nozzle subjected to needle motion. Two meshing approaches shown. Initial mesh generated at full lift (left-most image), lowered (left-center image), results in highly skewed cells. Initial mesh generated at low lift (right-center image), raised (right-most image), results in minimized cell skewness.

Next, generating a mesh at low lift is best done with cells that have a high aspect ratio in the direction of the flow. This must be done to keep the total cell count down. A good visualization of this best-practice can be seen in Fig. 5.10.

Finally, if using the layer motion with layer addition/removal approach, it is best to start with a non-zero number of uniform layers. This is because it allows the initial mesh motion to be distributed and it reduces and distributes the inherent mesh-dependency error introduced with the addition of cell layers. For example,

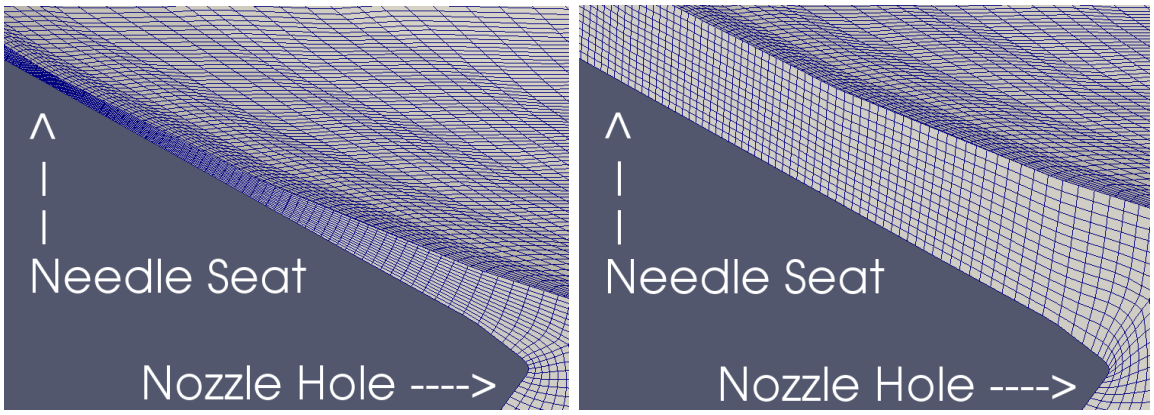

Figure 5.10: Mesh shown for the region between needle and nozzle wall at 5 μm lift (left) and 50 μm lift (right) for the ECN spray G injector.

taking this approach will allow for the first topology change to result in the flow solution being mapped from say 6 cell layers to 7, rather than from 1 to 2.

In this regard, two limitations with the layer addition/removal and uniform motion libraries developed for HRMFoam were discovered. The first prevents the removal of a face which is also a processor boundary. The second prevents uniform layer motion from occurring through processor boundaries. These limitations can be avoided by never removing cells which were not previously added by the motion routine. This, however, is also a limitation of its own, i.e. the best-practice described above cannot be achieved in parallel.

For this reason, a program and script were written to help setup parallel cases in a way which ensures that all of these limitations are avoided. The process works in the following way:

- In serial, lower the needle with a mesh motion only solver, removing as many layers of mesh as desired. These will be built back again in parallel and utilized for uniform mesh motion at the start of the simulation.

- Decompose the case so that it can be run in parallel.

- In parallel, lift the needle with a mesh motion only solver, adding as many layers as had previously been removed.
- Set up the initial fields for the CFD simulation.

5.5 High Pressure Thermodynamic Properties

The thermodynamic class of the HRMFoam solver has been extended to properly handle high pressure thermodynamic properties. The properties are tabulated before runtime using the NIST REFPROP database [103]. HRMFoam then reads the table into memory and utilizes fast lookup/interpolation routines to access the properties at runtime.

Proper integration of these properties into the solver also required a correction to the enthalpy equation. The viscous dissipation term was using the fluid viscosity, while the momentum equation was using the effective viscosity, which accounts for both the fluid viscosity and the turbulent eddy viscosity. Total energy flux for the inlet and outlet of a 100 MPa injection n-dodecane test case are shown in Fig. 5.11. The correction to the enthalpy equation occurs just after 1 ms of runtime, at which point it can be seen that energy is conserved.

Error in the liquid density was also observed. This is because the density change of a fluid due to a change in enthalpy can be very significant. HRMFoam was not accounting for this. A simple and effective change was implemented as can be seen in Eqn. 5.31.

$$-\rho\nabla\cdot(\mathbf{U}_p)_f = \frac{D\rho}{Dt} = \left.\frac{\partial\rho}{\partial p}\right|_{x,h,y}\frac{Dp}{Dt} + \left.\frac{\partial\rho}{\partial x}\right|_{p,h,y}\frac{Dx}{Dt} + \left.\frac{\partial\rho}{\partial y}\right|_{p,h,x}\frac{Dy}{Dt} + \left.\frac{\partial\rho}{\partial h}\right|_{p,x,y}\frac{Dh}{Dt} \tag{5.31}$$

Here, the last term accounts for density change due to a change in enthalpy. This term is calculated upon construction of the property tables, based upon a linear gradient of the enthalpy and density data. These values are then stored in memory and accessed

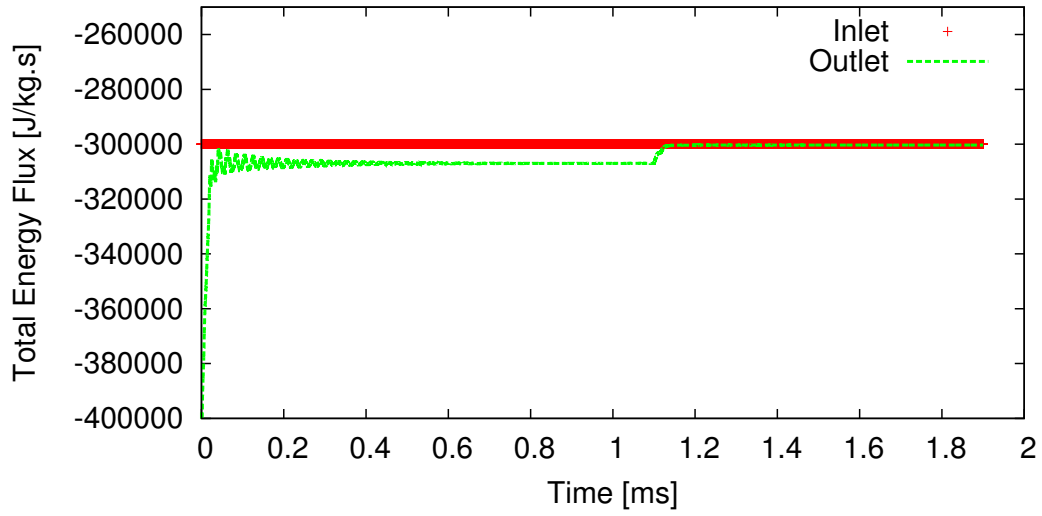

Figure 5.11: Total energy flux through the inlet and outlet of a high-pressure n-dodecane test case. At 1 ms, the enthalpy equation was corrected to use the effective viscosity.

using the same interpolation/lookup routines. The results of this fix can clearly be seen in Fig. 5.12.

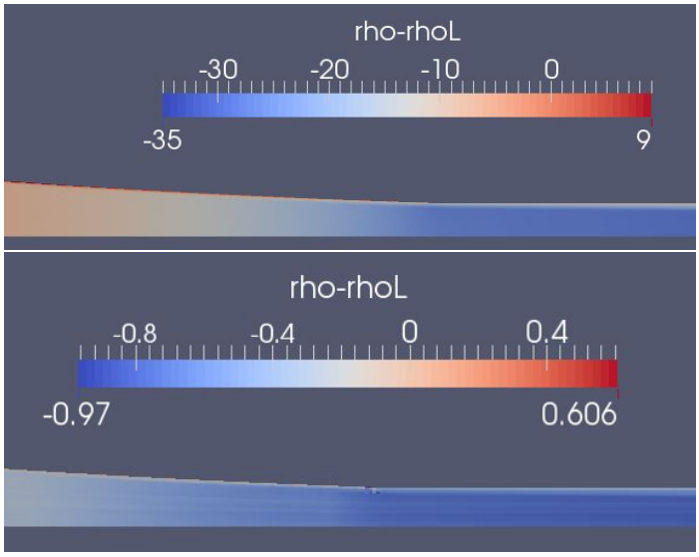

Figure 5.12: Density minus liquid density for high pressure n-dodecane test case.

CHAPTER 6

CASE STUDIES: DIESEL INJECTION

6.1 $\Sigma - Y$ Simulations of External Diesel Sprays

Over the past decade, the $\Sigma - Y$ atomization model has been increasing in popularity for the simulation of high Reynolds and high Weber number flow. In the 2013 work by García-Oliver et al. [64], we validated a compressible formulation of this model using high speed imaging, PDPA, and Rayleigh-scattering measurements. The solver used in this work also included modeling of fuel vaporization. This work will be described below, with some passages quoted verbatim from the published work.

6.1.1 Case Setup

This study was conducted on a 2-D axisymmetric computational domain which spanned 80 mm in the axial direction and 25 mm in the radial. The mesh was structured with non-uniform grid resolution. There were 10 cells along the orifice diameter, keeping an aspect ratio close to one in the near-field region, as depicted in Fig. 6.1. A mesh size convergence study was performed in order to achieve grid independent results. The grid used in the calculations is comprised of 450 x 80 cells, with a cell expansion ratio of 1.01 and 1.06 in the axial and radial directions, respectively.

A Gamma NVD scheme was used for discretization of divergence terms and a first order Euler scheme was applied for time derivative terms. The inlet velocity boundary condition was obtained from mass flow rate and momentum flux measurements, applying a constant radial profile of axial velocity and density at nozzle outlet. The turbulent intensity was set to 5% and the length scale to 10% of nozzle diameter.

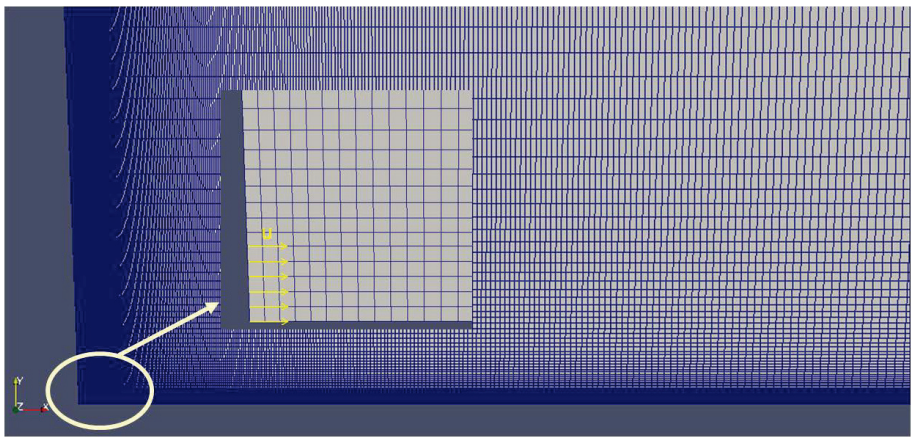

Figure 6.1: Computational grid. The inset shows the mesh near the nozzle exit.

The turbulence model used in this study was a modified form of the k-ε model meant to account for flows with high density ratio [192]. Due to the well-known round jet spreading overprediction of k-ϵ turbulence models, this study first demonstrated the improvement obtained from using the corrected $C_{1\epsilon}$ constant of (1.6) as suggested by Pope [150], compared to the standard value of (1.44), and then adopted this correction for the remainder of the investigation.

The LHF evaporation model described in section 5.2.1 was used in the vaporization section of this study.

6.1.2 Results and Discussion

6.1.2.1 Non-Vaporizing Conditions

A series of experiments with different ambient and injection conditions were simulated. The range of validity of the model was evaluated by running cases with lower ambient density (25 and 10 kg/m^3) and increased (130 MPa) and decreased (30 MPa) injection pressures. As shown in Fig. 6.2, the accuracy of spray penetration predictions for high and intermediate ambient densities was similar, though some differences in centerline velocity results can be observed for ρ_a=25 kg/m^3 con-

ditions. Spray penetration was under-predicted for the lower ambient density, and also centerline velocities were lower than PDPA measurements.

Similarly, the velocity radial profiles shown in Fig. 6.3 show good agreement for high and medium ambient density, and a significant departure from experiment for the low ambient density condition. The worst agreement occurs in the low injection pressure, low ambient density case. Here both Reynolds number and ambient to fuel density ratio are decreased, potentially having an effect on the spray atomization regime [154] and compromising the validity of the model assumptions. Here the slip between phases is more significant and better results could likely be obtained through Lagrangian tracking for sparse spray regimes [23] or a more detailed model for the diffusion flux term closure, such as suggested in [10].

6.1.2.2 Vaporizing Conditions

Vaporizing sprays were simulated using the Spray A specifications as the base case. Results shown in Fig. 6.4 depict good agreement for both liquid and vapor penetration. In both cases, predictions were within the experimental error interval of measured values. The accuracy in maximum liquid length predictions confirms that the evaporation process under Spray A conditions is mainly mixing-controlled.

Predicted vs. measured centerline mixture fraction is shown in Fig. 6.5. Here the predicted values on the axis always fell within the experimental error interval, except below 22 mm, where the measuring uncertainty was also larger.

Parametric studies with different injection conditions, as well as with different ambient density and temperature were also performed. Spray vapor penetration and liquid length predictions have been summarized in Fig. 6.6 to Fig. 6.8. Trends of decreasing vapor penetration with decreasing injection pressure and increasing penetration with decreasing ambient density were captured by the model. In general, good agreement between calculations and experiments was obtained, with most of the

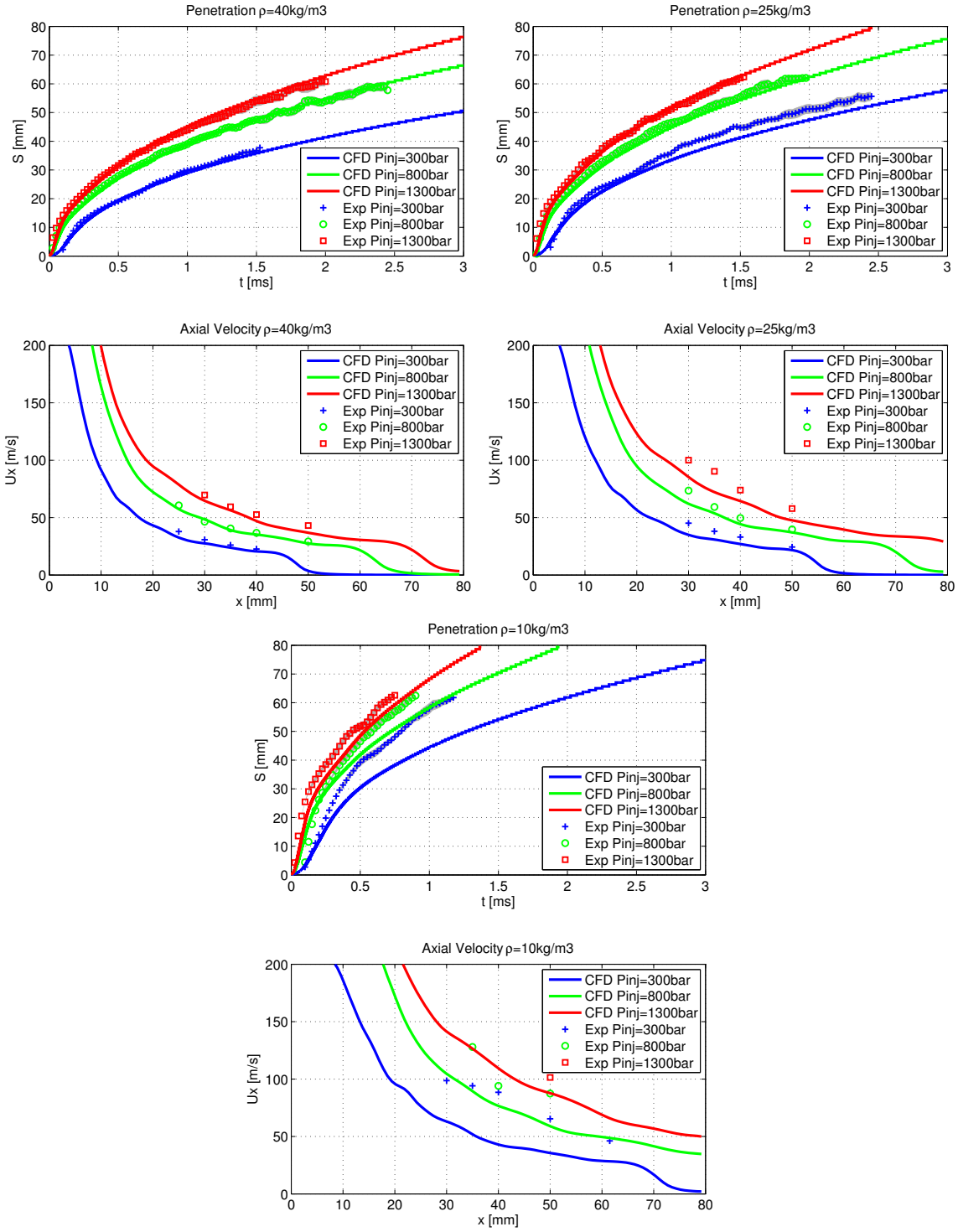

Figure 6.2: Spray penetration and centerline axial velocity over a variety of ambient densities.

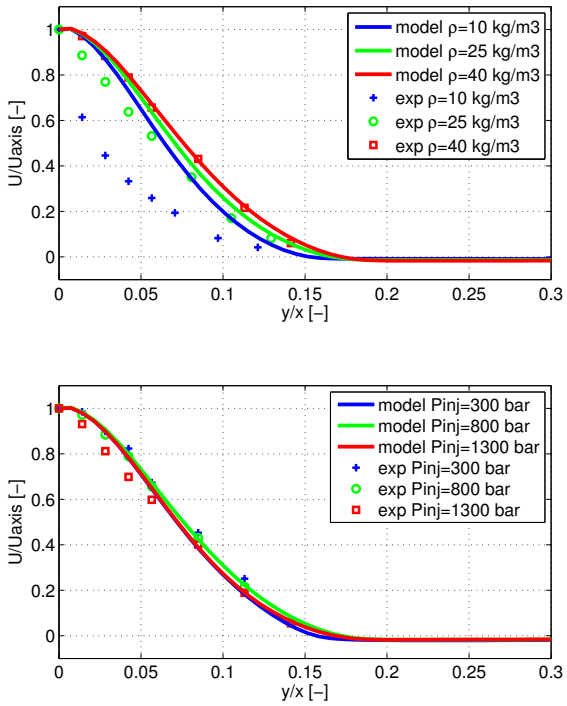

Figure 6.3: Axial velocity radial profiles for P_{inj}=800 bar (bottom) and $\rho_a = 40\text{kg/m}^3$ (top) at x=35 mm.

predicted results within experimental uncertainties. The effects of ambient density and temperature on quasi-steady values of liquid length were also well predicted. Departures were noticeable at the lowest density conditions, which could be expected from the non-vaporizing spray results. This agreement also confirms that the LHF evaporation model is valid over a wide range of operating conditions of current diesel engines.

6.1.3 Summary

This study demonstrated the ability of the $\Sigma - Y$ model to capture liquid and vapor penetration as well as spatial distribution of axial velocity, and fuel mass fraction. The model is applicable to ambient gas density conditions that are normally present in Diesel engines, but would be less accurate for very early injection conditions, such as those found in highly premixed combustion strategies, due to the lower ambient

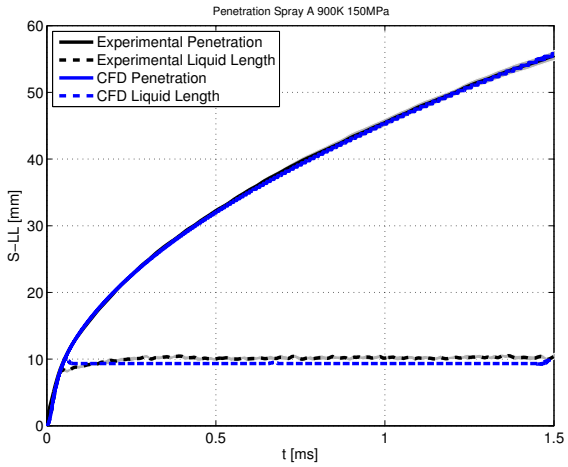

Figure 6.4: Computed and measured liquid and vapor penetration. Injector 210677, P_{inj}=150 MPa, T_a=900 K and ρ_a=22.8 kg/m^3.

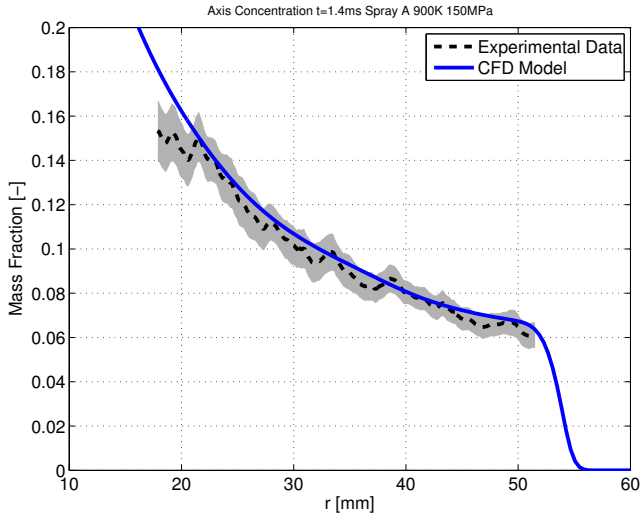

Figure 6.5: Centerline mixture fraction with ρ_a=22.8 kg/m^3.

density. Ambient density conditions in GDI engines are also low. This suggests that accurate Eulerian modeling of GDI sprays would require a transition to Lagrangian particle tracking in the near-field of the spray.

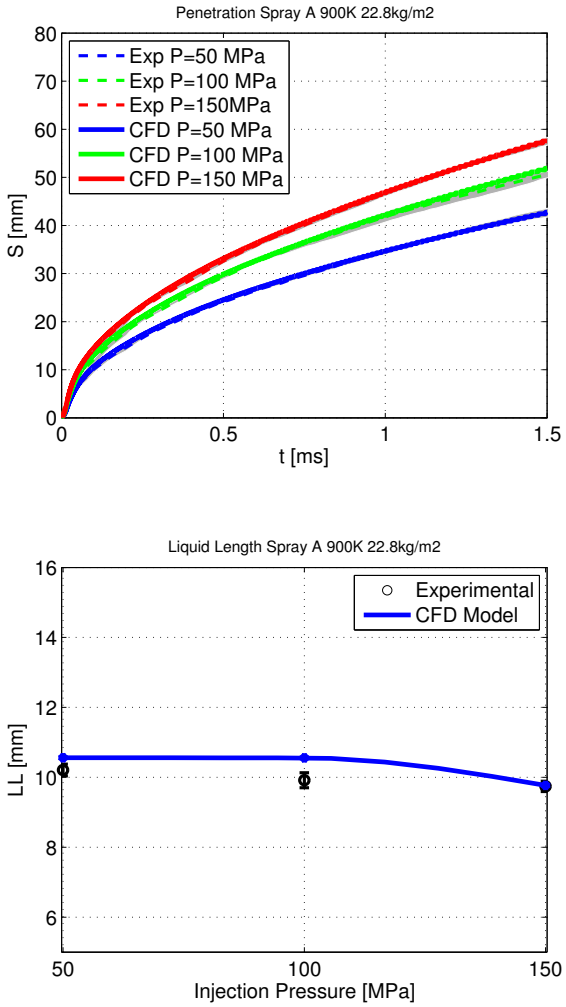

Figure 6.6: Vapor and liquid penetration with T_a=900 K.

6.2 Coupled Internal/External Simulations

In the 2016 work by Desantes et al. [36], we further validated the $\Sigma-Y$ atomization model with a focus on near-field internal structure and we investigated the influence of coupling internal nozzle flow simulations with the downstream spray. A coupled internal/external simulation was conducted in 3D and in 2D and the results were compared. Additionally, the 2D coupled internal/external simulation was compared with two external-only simulations. This work will be summarized below, with some passages quoted verbatim from the published work.

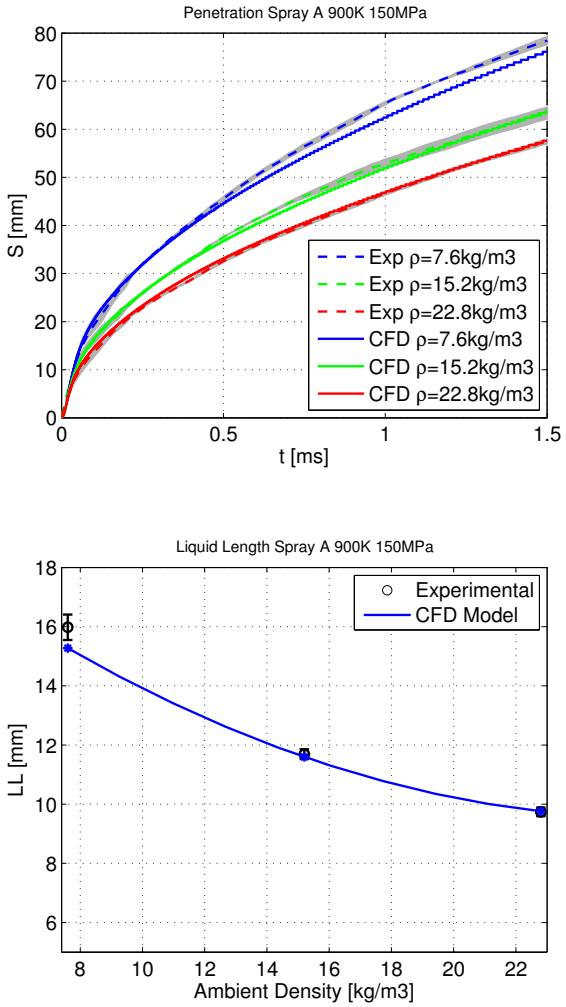

Figure 6.7: Computed and measured vapor penetration and liquid length for different conditions of ambient density.

6.2.1 Experimental data

The Spray A non-evaporating condition of ECN was used in order to evaluate the model in terms of the near-field structure of diesel sprays. The experiment was conducted with the ambient gas at room temperature (303 K) as the X-ray transparent polymer windows used cannot be subjected to high temperatures. Nevertheless, the same ambient density of the nominal evaporating Spray A condition was matched in order to reproduce similar conditions for the spray breakup process, assuming that density is a more critical parameter than pressure for atomization [122]. The main

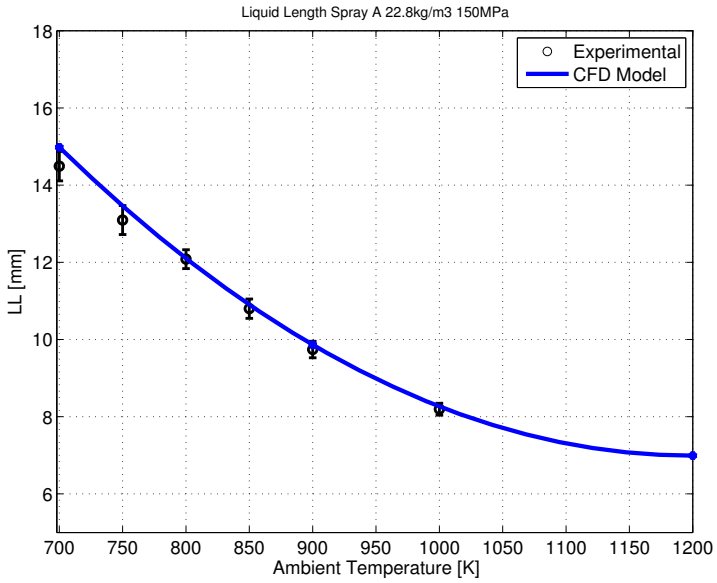

Figure 6.8: Computed and measured liquid length for different conditions of ambient temperature.

.

Table 6.1: Conditions for non-evaporating Spray A experiment

Fuel	n-dodecane
Ambient composition	100% N2
Injection pressure [MPa]	150
Ambient temperature [K]	303
Ambient density [kg/m^3]	22.8
Fuel injection temperature [K]	343

conditions of this experiment are presented in Table 6.1. Further details about the experimental set-up are provided in [90].

Detailed internal nozzle geometric characterization has been performed for the injector employed in these experiments, where the main characteristics are presented in Table 6.2. D_o, D_i, L and r denote nozzle orifice outlet diameter, nozzle orifice inlet diameter, length, and inlet radius, respectively. The nozzle convergence is described by the k-factor, as defined in [113]. Experimental data is based upon measurements

Table 6.2: Nozzle geometric characteristics for single-hole Spray A ECN injector

Injector Serial#	D_o[μm]	D_i[μm]	L/D_o[-]	r/D_o[-]	k-factor	exit offset [μm]
210675	89.4	116	11.5	0.23	2.7	53

taken on injector #210675. Experimental characterization has revealed that the orifice outlet for this nozzle is offset from the nozzle axis.

6.2.2 Case Setup

The 3D geometry used in this work captured the off-center nozzle hole, as depicted in Fig. 6.9. This computational domain included a cylindrical spray chamber 12 mm in length and 14 mm in diameter. In Fig. 6.9, the mesh structure can be seen. It consisted of 2.25 million hexahedral cells with a minimum cell size of 1.5 μm near the walls inside the nozzle and a maximum cell size of 250 μm far from the orifice exit.

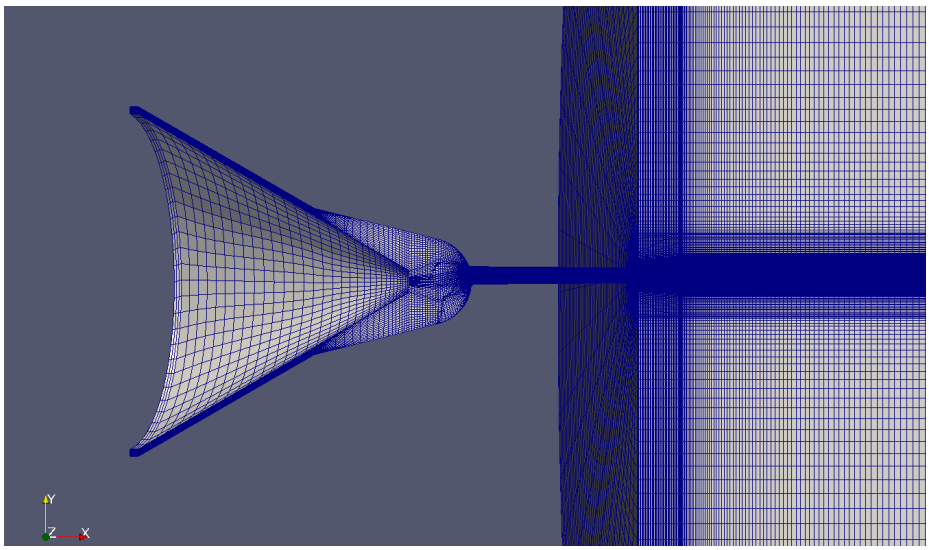

Figure 6.9: Computational grid for three-dimensional Spray A simulations

A 2D axisymmetric mesh with the same geometry dimensions and mesh resolution as the 3D domain was used and can be seen in Fig. 6.10. There are 89,000 cells with 72 elements at the orifice exit.

Finally, a 2D axisymmetric computational domain without the nozzle geometry was considered. This mesh consisted of 20 cells along the orifice diameter, an aspect ratio close to one in the near-field region, and non-uniform grid resolution consists of cells with an expansion ratio of 1.01 and 1.06 in the axial and radial directions.

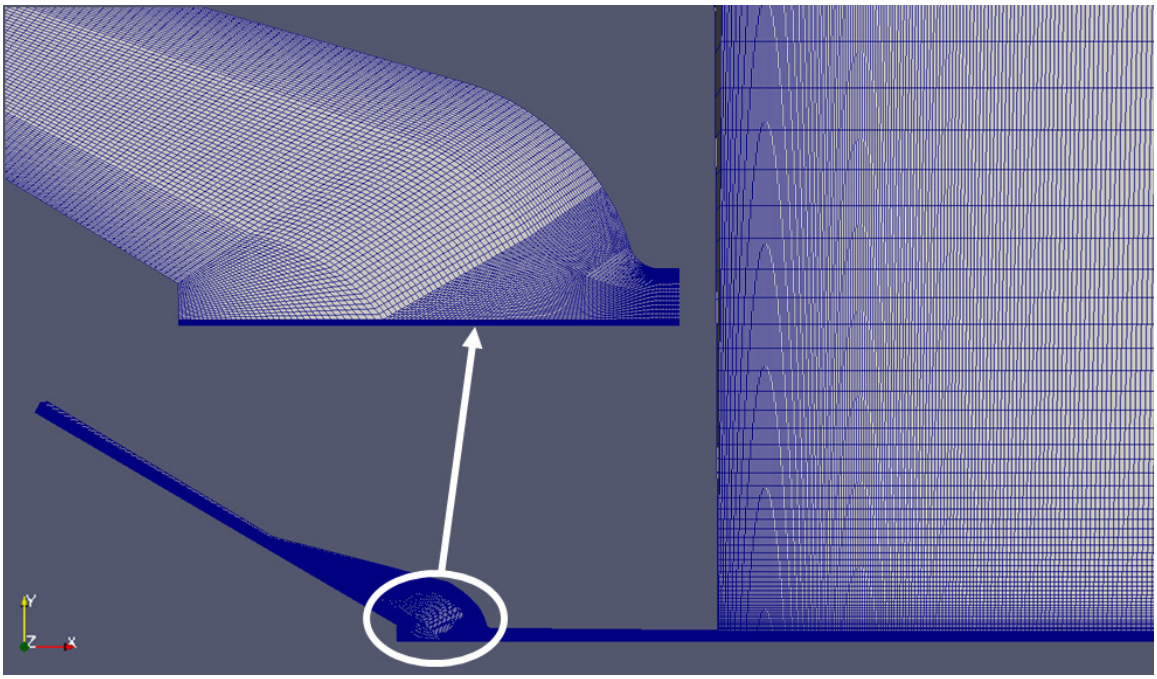

Figure 6.10: Grid used for coupled nozzle-spray simulations

Boundary conditions selected for all the walls of the domains were no-slip. A non-reflexive boundary condition was used for the outlet and a time varying velocity condition was used for the inlet. The inlet velocity was obtained from mass flow rate and momentum flux measurements.

The k-ϵ turbulence model was used. The turbulent intensity was set to 5% and the length scale to 10% of the inlet length. Due to the well known round jet spreading overprediction of k-ϵ type models [150], a corrected value (1.60) for $C_{1\epsilon}$ was used, as indicated in [64]. Pope [150] has previously suggested that the latter value should be used for round jets. The liquid turbulent flux closure [10] was calculated by means of a gradient closure, the discretization of the divergence terms was solved with a

Gamma NVD scheme, and a first order Euler scheme was applied for time derivative terms.

6.2.3 Results and Discussion

6.2.3.1 3D vs 2D Coupled Simulations

The first study conducted was a comparison of the coupled 3D and 2D simulations to the experimental data. Obviously, only the 3D geometry is capable of capturing the experimental asymmetries. However, investigating the effectiveness of 2D simulations is of interest because of the benefit of reduced computational cost.

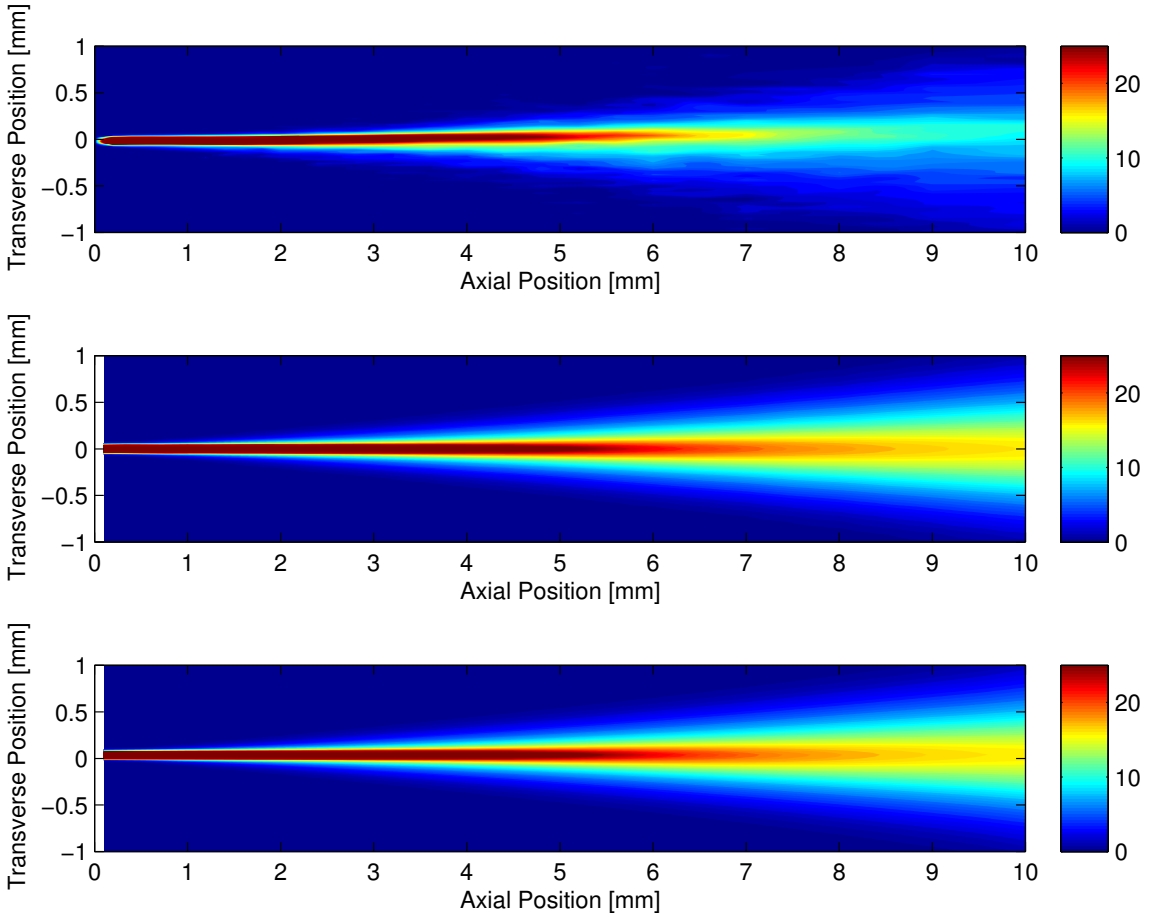

Figure 6.11: Projected density distributions from X-ray data (top), 2D CFD simulation (middle), and 3D CFD (bottom) [μg/mm^2] at 500 μs after SOI

From the projected density contours it is seen that the simulations can capture the fuel distribution in the very near-field region (i.e., within 6 mm) with both meshes. Downstream of this axial position, the radial dispersion of simulations tend to be over-predicted.

The projected density along the transverse direction comparing the simulations and X-ray radiography data is shown at 0.1 mm, 2 mm, and 6 mm downstream of the nozzle exit in Fig. 6.12. The 3D computational profiles shown in this figure were made along the transverse directions Y and Z, respectively. The profiles in both 3D directions are essentially identical; however, the profile which corresponds to the Y axis is shifted due to the off-center nozzle position. At the three axial positions, a very similar density profile is predicted by the model independent of the used grid. Comparing the CFD predictions with the experimental measurements, the largest differences can be observed at 6 mm. Here projected density is well matched in terms of radial dispersion but over-predicted in terms of peak value.

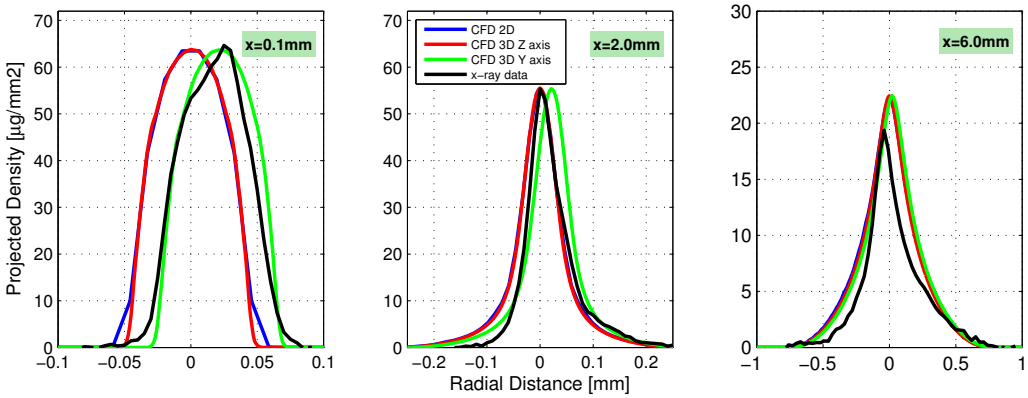

Figure 6.12: Computed and measured profiles of projected mass density [μg/mm^2] at 500 μs after SOI at axial locations of 0.1 mm, 2 mm, and 6 mm downstream of the nozzle exit

As explained in [209], the mass distribution data can be used to describe the trends in the axial spray velocity under steady-state conditions. This is done by means of the TIM, which is inversely proportional to the mass-averaged axial spray velocity at

any given axial location. Thus, the relative velocity can be obtained by normalizing the TIM at any location with the TIM at the nozzle exit. This is used to compare the axial spray velocity profile along the axis among the simulations and X-ray data. Fig. 6.13 shows the predicted results of simulations, using the two different computational domains, compared with measurements. The relative velocity profiles for both 2D and 3D computations are essentially identical, which shows that 2D simulations are adequate if nozzle asymmetry does not need to be captured. Compared with the experimental profile, the relative velocity is increasingly under-predicted with axial position, with a noticeable divergence occurring at 3 mm and 6 mm.

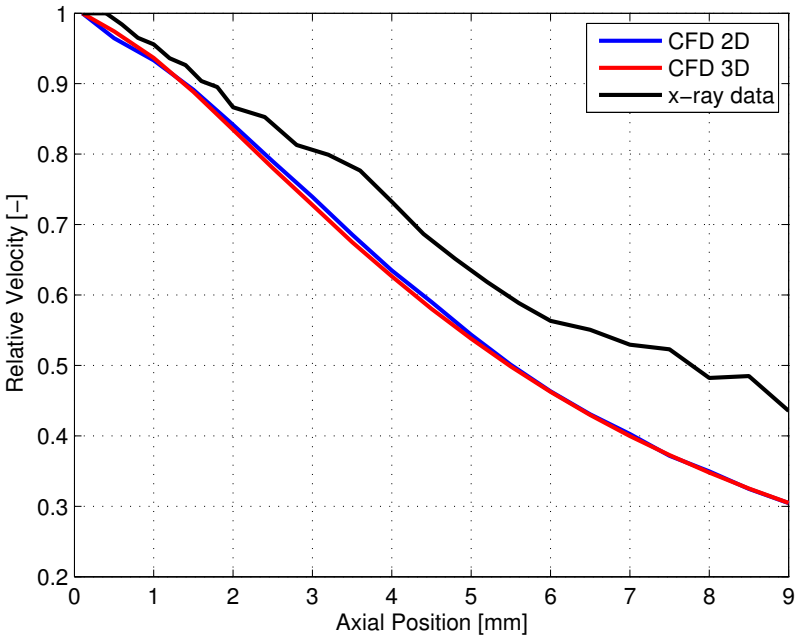

Figure 6.13: Computed and measured mass-average spray velocity along the axis at 500 μs after SOI

Overall, the $\Sigma - Y$ model provides modest agreement with experimental data and can capture the trend of the internal structure of a diesel spray fairly well in the near-field. This is shown in the projected density profiles as well the relative velocity profiles. Beyond 6 mm downstream of the nozzle exit, the peak projected mass density is over-predicted. Furthermore, it is clear that the 2D axisymmetric

domain is completely capable of predicting satisfactory results when asymmetry is not present at the nozzle. As a result, the following simulations, conducted in order to evaluate different turbulence models, have been made using this mesh.

6.2.3.2 2D Decoupled Simulations

Next, two more simulations were conducted using the 2D axisymmetric computational domain without the nozzle geometry. The first simulation was conducted using the fields obtained at the nozzle exit in the 2D coupled simulation as an inlet boundary condition. To do that, the mapped boundary condition of OpenFOAM was used. The other simulation was made without any influence of internal flow simulation. The inlet boundary condition was a top-hat (TH) radial profile of axial velocity obtained from mass flow rate and momentum flux measurements [143]. In this case, the turbulent intensity and the length scale were taken as area-averaged values at nozzle exit from coupled simulation.

Here, the analysis is started with the projected density along the transverse direction comparing the simulations and X-ray radiography data at 0.1 mm, 2 mm, and 6 mm downstream of the nozzle exit in Fig. 6.14. This figure shows the profiles of the 2D coupled simulation (as reference) against the profiles achieved with the decoupled ones. The radial dispersion of all profiles is quite similar. When comparing peak projected density, the profiles predicted with the flat inlet velocity profile performed slightly worse, under-predicting at 0.1 mm and over-predicting at 6 mm.

In Fig. 6.15 the relative velocity axial profile as derived from TIM is shown. Once again, the three profiles are quite similar and the trends are well captured. The coupled simulation achieved the best match with the experimental measurements and predicted a less diffusive spray as indicated by slower relative velocity decay.

To study the influence of the internal flow simulation on penetration and liquid volume fraction (LVF) field, the simulations conducted using the mesh without the

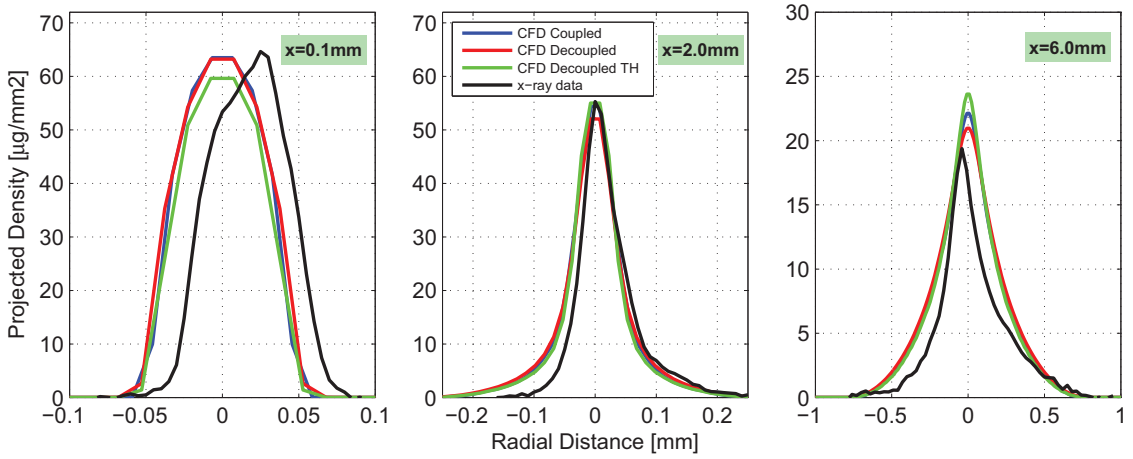

Figure 6.14: Computed and measured profiles of projected mass density [μg/mm^2] at 500 μs after SOI at axial locations of 0.1 mm, 2 mm, and 6 mm downstream of the nozzle exit for different types of 2D simulations

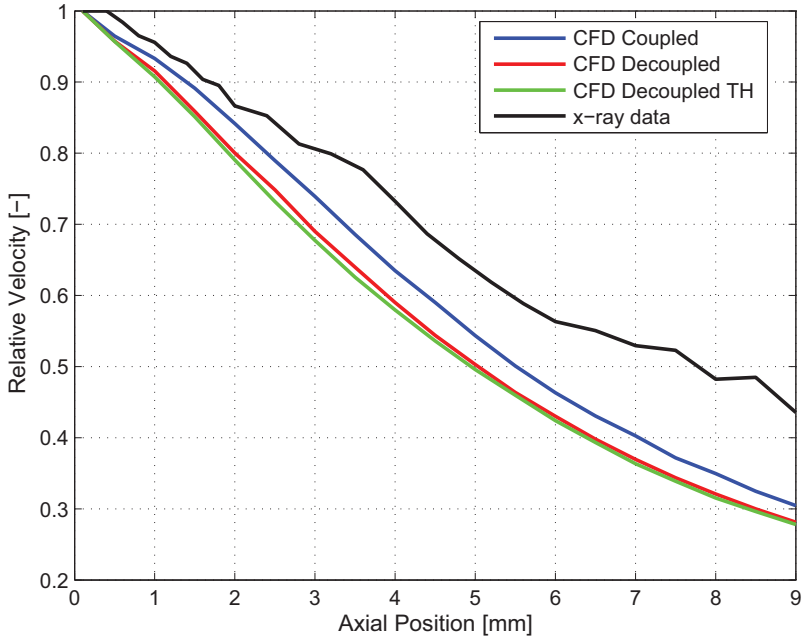

Figure 6.15: Computed and measured mass-average spray velocity along the axis at 500 μs after SOI for different types of 2D simulations

internal nozzle geometry have been run to a time of 3 ms after start of injection. In Fig. 6.16 spray penetration (left) and predicted centerline LVF profiles (right) are compared. In terms of spray penetration, the top-hat simulation over-predicts during

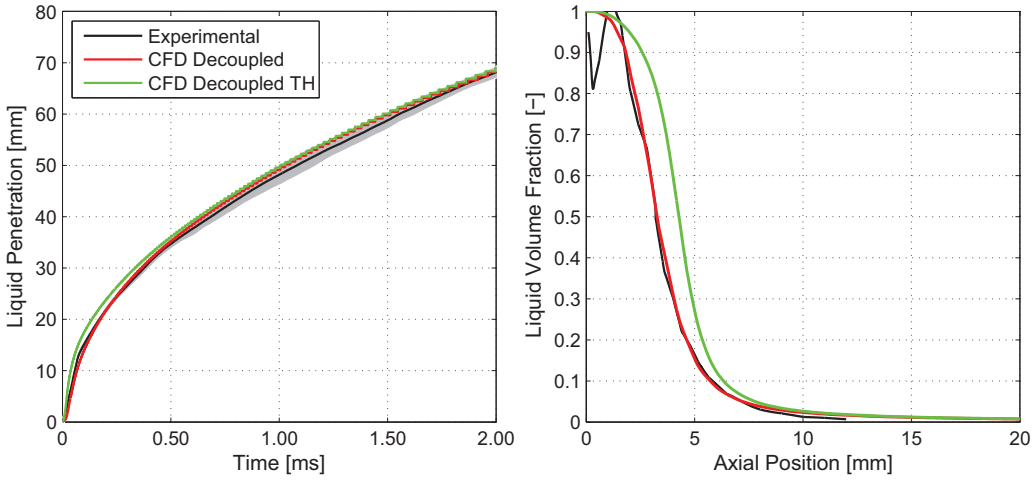

Figure 6.16: Spray penetration [left] and computed centerline liquid mass fraction at 2 ms after SOI [right] for different types of 2D simulations

the first 0.5 ms of simulation, after which both simulated curves perform well. In terms of LVF on the axis, the decoupled simulation, with the nozzle profile derived from the coupled calculations, performs better than the top-hat decoupled case, exactly matching the decay of the liquid volume fraction and predicting an intact liquid core (LVF > 0.9) almost in the range estimated by recent analyses in [].

6.2.4 Summary

The $\Sigma - Y$ Eulerian atomization model has been applied to the study of direct injection diesel sprays, with a focus on reproducing the internal structure of a diesel spray in the near-field. Calculations have been validated against X-ray radiography measurements of non-evaporating Spray A condition of ECN, conducted at Argonne National Laboratory.

3D and 2D coupled internal/external flow simulations were compared. Both simulations produced qualitatively and quantitatively good agreement with the experimental data, showing that unless asymmetries are present in the nozzle, 2D simulations are adequate.

Additionally, external spray simulations were run without the internal nozzle flow. In one case, the inlet boundary condition was taken from the coupled simulation and in the other a top-hat velocity profile obtained from mass flow rate and momentum flux measurements was applied at the nozzle outlet. Here performance was similar, with the top-hat simulation slightly under-performing when compared to the other decoupled simulation and the coupled simulation. Therefore, an interesting conclusion of this study is that when ROI and momentum flux measurements are available, and no cavitation is involved, internal flow modeling provides only marginal benefit and a two-dimensional external study is perhaps sufficient.

6.3 Simulating the ECN Spray D Converging Nozzle

Simulations were conducted to investigate the influence of transient needle motion and internal nozzle flow on a converging diesel injector. The influence of flash-boiling conditions was also investigated using n-pentane fuel at elevated temperatures. Rate of injection and momentum flux profiles were considered and results were compared to an experimental hydraulic characterization study conducted by Payri et al. [144]. Furthermore, localized and mass flux averaged fuel temperatures were analyzed and a thermodynamic analysis was conducted to inform the CFD results.

6.3.1 Case Setup

Two 3D meshes were used. There were both based upon the same topology which consisted of the internal nozzle with a $\sim$2.5 mm outlet plenum. One mesh was intended for static, full lift simulations and the other for dynamic needle motion. Cell count and structure were similar. The static simulations were conducted first and used for the hydraulic characterization which required only a steady-state solution. The internal nozzle was based upon an axisymmetric radial profile obtained through commercial CT measurements [1]. The exit diameter of the domain was equal to

the nominal specification of 186 μm and boundary layer cells were used to allow for log-law wall functions to model the turbulent boundary layer.

For the dynamic mesh simulations, an in-house layer addition and removal library with uniform layer expansion and contraction was used to capture the needle motion. The initial needle lift was $\sim$10 μm and the mesh consisted of 676k cells prior to the first layer addition. At peak needle lift 410 μm, 15 layers were added to the mesh, increasing the cell count by 195k. A linear needle lift velocity of 1 m/s was imposed from 10-410 μs, and a linear needle drop of 1 m/s was imposed from 610-1020 μs. Simulations therefore ran for around 1015-1016 μs, at which point the needle lift was less than 10 μm and the solver would crash as a result of high cell aspect ratios and non-orthogonality.

The target conditions chosen for the CFD study are described in Table 6.3. The n-dodecane target conditions are intended to match those of the Payri et al. study [144]. The n-pentane conditions are identical to those chosen for the flashing parameter study conducted on axisymmetric GDI nozzles, described in detail in section 7.1.

Table 6.3: Conditions for the CFD simulations.

Fuel	P_a/P_s [-]	ΔP [MPa]	U_{theo} [m/s]	P_a [kPa]	T_a [K]	T_{exit} [K]
n-dodecane	12,146	150	631	6,000	300	343
n-dodecane	12,146	100	511	6,000	300	343
n-dodecane	12,146	50	350	6000	300	343
n-pentane	0.8	20	268	326	300	357
n-pentane	0.3	20	268	122	300	357

For the CFD simulations, the mass flow rate and momentum flux were calculated using swak4Foam libraries to integrate the fluxed values across a set of cell faces at the outlet of the nozzle. Experimentally, the mass flow rate was obtained through the Bosch method, described in Ref. [145], and momentum flux was measured using a device designed by CMT-Motores Términcos, described in Ref. [143]. These exper-

imental data were there basis of the Payri et al. work published in Fuel [144], and they are used here with permission from Professor Raul Payri from CMT-Motores Térmicos. The ideal velocity used to calculate the discharge and velocity coefficients was obtained through Eqn. 6.1 which is based upon a compressible conservation of energy analysis.

$$U_{ideal} = \sqrt{2\left(\frac{P_1}{\rho_1} - \frac{P_2}{\rho_2}\right)} \tag{6.1}$$

The SST k-ω RANS model turbulence model was used. Fuel compressibility was based upon the fuel properties provided by NIST and the ideal gas law was used to account for NCG compressibility. Fluid mixture properties were based upon a volume average of the liquid, vapor, and non-condensable gas components.

6.3.2 Results and Discussion

6.3.2.1 Hydraulic Characterization

The discharge, area, and velocity coefficients from the CFD simulations and from experiment are shown in Figs. 6.17-6.19. A slight degree of nozzle-to-nozzle variability is exhibited amongst the experimental data. This variability is likely due to manufacturing imperfections resulting in differences between the nozzles in terms of surface roughness as well as hole size and shape. Furthermore, the variability in C_d and C_a is compounded by inaccuracies in measurement of the nozzle diameter, whereas C_v depends purely on experimental measurement of the mass and momentum flux.

The discharge coefficients from the CFD simulations agree well with those from experiment. The trend of increasing C_d with increasing Reynolds number is captured for the n-dodecane simulations. However, this trend does not continue for flash-boiling cases. Here, although the injection pressures are lower, the Reynolds numbers are higher because n-pentane has a much lower viscosity than n-dodecane. The reason

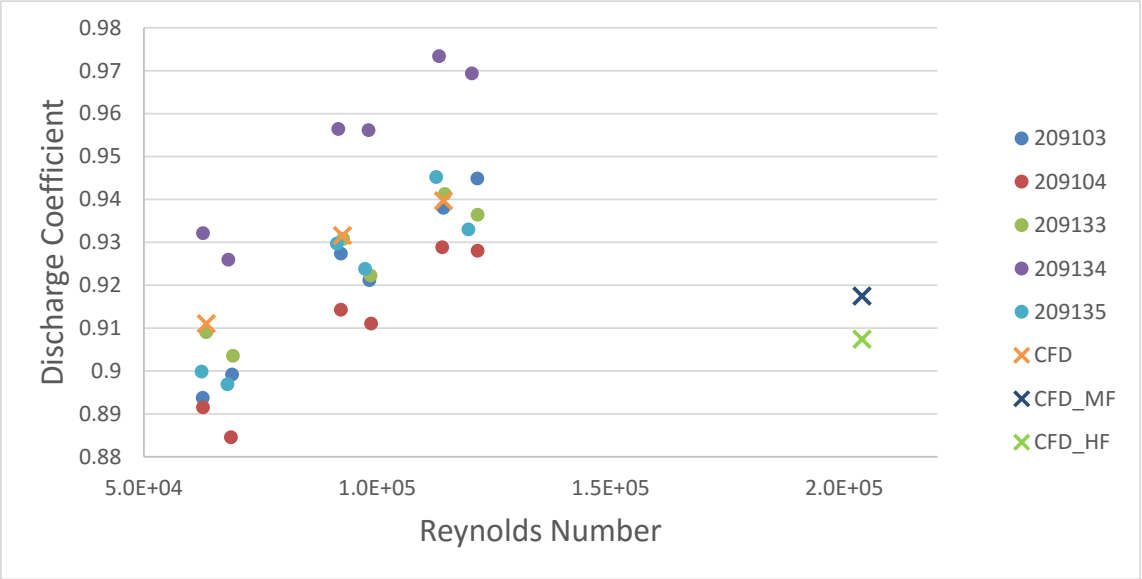

Figure 6.17: Coefficient of discharge plotted against Reynolds number. Experimental data from Payri et al. [144] labeled by nozzle serial number. The n-dodecane simulations labeled CFD, the mild-flashing simulation labeled CFD_MF, and hard-flashing CFD_HF.

these flash-boiling cases have lower C_d values becomes clear when analyzing their area coefficients.

For the flashing cases, area coefficients are significantly lower. This is due to the presence of vapor at the nozzle exit reducing the effective exit area, as seen in Fig. 6.20. Coefficient of area values for the n-dodecane simulations agree well with those from experiment. The slight trend of increasing C_a with increased Reynolds number is captured. This is the result of turbulent momentum exchange causing a more uniform exit velocity profile.

Finally, when considering the velocity coefficients, it can be seen that the n-dodecane cases agree well with experiment, matching the trend of increasing C_v with increasing Reynolds number. As turbulence becomes more and more developed with increasing Reynolds number, this trend is expected to plateau, as C_v cannot exceed unity without the system violating the conversation of energy. This plateau in the trend is observed here, with the flashing cases having high and essentially identical

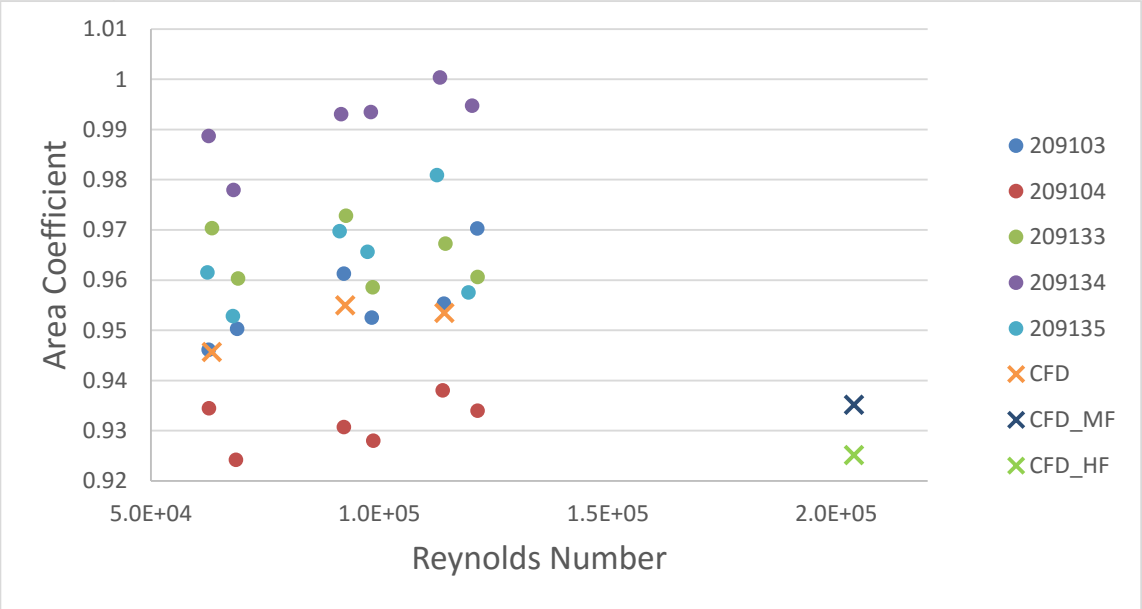

Figure 6.18: Coefficient of area plotted against Reynolds number. Experimental data from Payri et al. [144] labeled by nozzle serial number. The n-dodecane simulations labeled CFD, the mild-flashing simulation labeled CFD_MF, and hard-flashing CFD_HF.

velocity coefficients. The similarity in the flashing velocity coefficients is interesting because it shows that the reduced discharge coefficient of the hard-flashing case is entirely the result of area losses.

6.3.2.2 External Flashing

While diesel injection never occurs into low ambient pressures, it is interesting to observe the influence of external flashing on an axisymmetric, converging nozzle. The influence is observed in two ways. First, as seen in Fig. 6.20, it results in a small amount of vapor generation at the nozzle exit. This results in a reduction in the area coefficients. As expected, the reduction is more significant is the hard-flashing case. Second, the spray angle is shown to increase with a decrease in the P_a/P_s ratio. This is shown in Fig. 6.21.

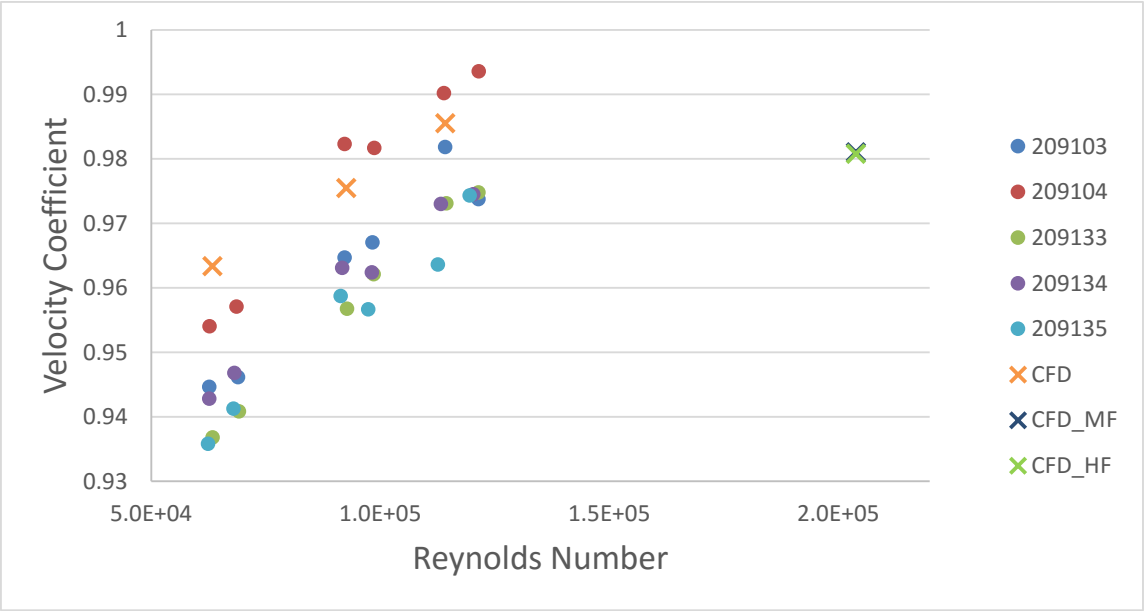

Figure 6.19: Coefficient of velocity plotted against Reynolds number. Experimental data from Payri et al. [144] labeled by nozzle serial number. The n-dodecane simulations labeled CFD, the mild-flashing simulation labeled CFD_MF, and hard-flashing CFD_HF.

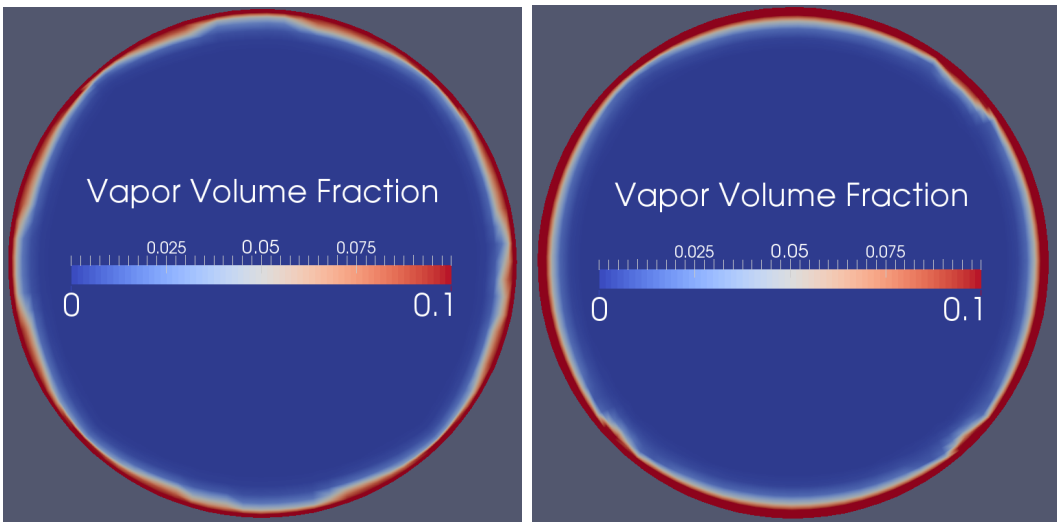

Figure 6.20: Steady-state vapor volume fraction at exit of nozzle for mild-flashing case (left) and hard-flashing case (right).

The spray angles observed here are essentially identical to those observed in the 2D parameter study conducted in section 7.1, with a value of 25° for the P_a/P_s ratio

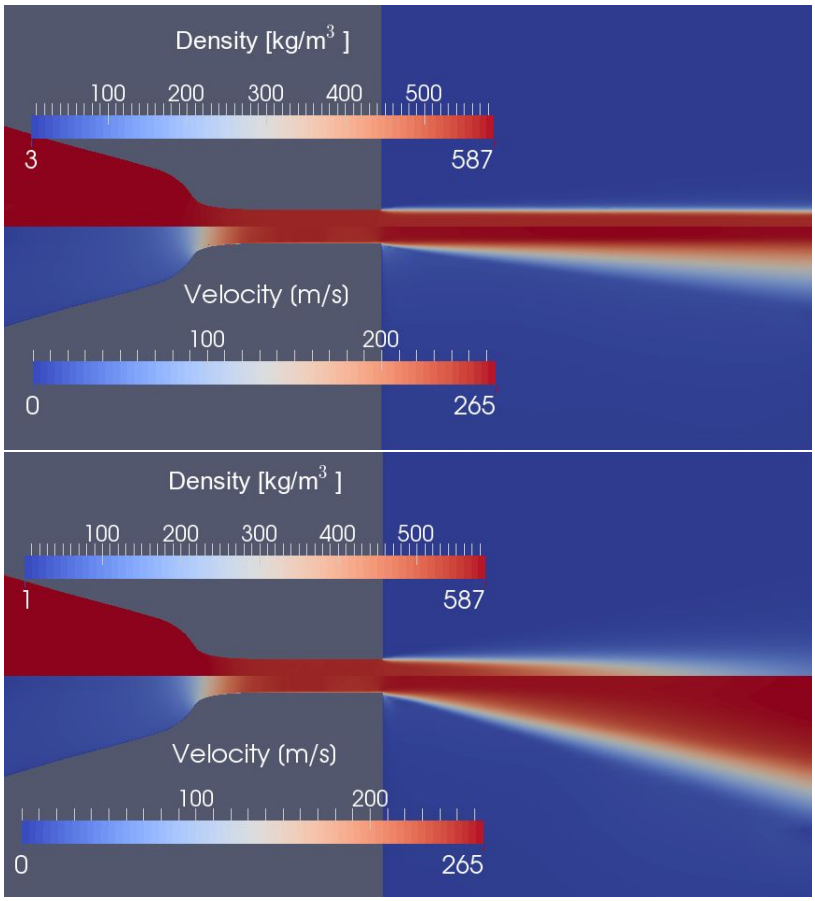

Figure 6.21: Influence of flash-boiling on spray D injection for mild-flashing case (top) and hard-flashing case (bottom).

of 0.3. This is an interesting result because it indicates that for for these types of axisymmetric nozzles, the diffusion of the spray is independent of the nozzle type and driven by the flash-boiling effects.

6.3.2.3 ROI and Momentum Flux

The rate of injection and rate of momentum flux from the four simulations can been seen in Figs. 6.22. Here it can be seen that the needle position has little to no effect on the magnitude of the mass and momentum flux beyond a lift of 100 μm. While the rate of swept volume by the needle is significant, 2 g/s for this nozzle, the

effect of this swept volume is felt less and less at the nozzle exit as the needle lift increases.

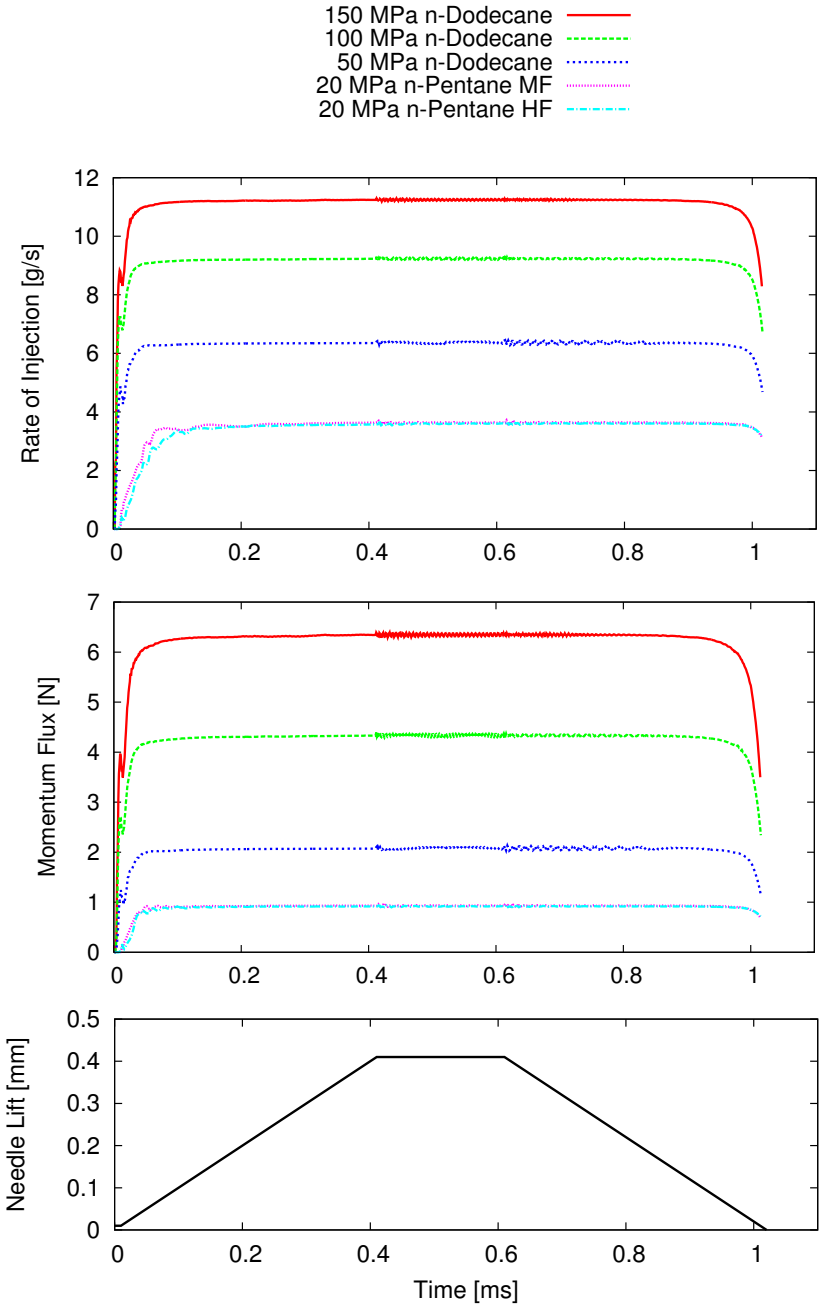

Figure 6.22: Rate of injection (top), rate of momentum flux (middle), and needle lift (bottom) for the four simulations.

The influence of the needle lift, however, should not be overlooked. At the very beginning of an actual injection event, for instance, the effects of this swept volume are fully felt at the nozzle outlet resulting in a brief but potentially significant back-flow into the nozzle. Furthermore, at the end of an injection event, the closing of the needle results in extremely low sac pressures as the momentum in the nozzle pulls against the now sealed injector seat, similar to the fluid hammer effect in pipe flow.

A very slight and high frequency oscillation in the rate of injection can be observed when the needle reaches peak lift at 410 μs. This oscillation then persists throughout the remainder of the simulations. This oscillation is caused by pressure waves initialized by the instantaneous change in needle velocity reflecting around the internal geometry. Such pressure waves likely exist in a physical injection process where the needle velocity can quickly change and with it the fundamental characteristics of the system.

6.3.2.4 Internal Flow

The seat region of spray D geometry was intentionally designed to mitigate the risk of internal cavitation damage. This was done by adding a divergence in the needle and nozzle walls directly after the seat. This divergence causes some interesting internal flow features at the beginning and end of the injection event.

Low needle lift causes fuel to flow past the needle seat at very high velocities. Upon reaching the divergence in the geometry, the CFD simulations predict that the fuel flow tends to stick to either the surface of the nozzle or the needle. This behavior is observed whenever the needle lift is less than 200 μm and can be seen in Fig. 6.23. The flow here is exhibiting the Coanda effect, which is the tendency of the fluid flow to remain attached to a convex surface. It is caused by a localized low pressure along the convex wall which is the result of momentum exchange between high speed jet and the low speed fluid near the convex surface. This low pressure then turns the

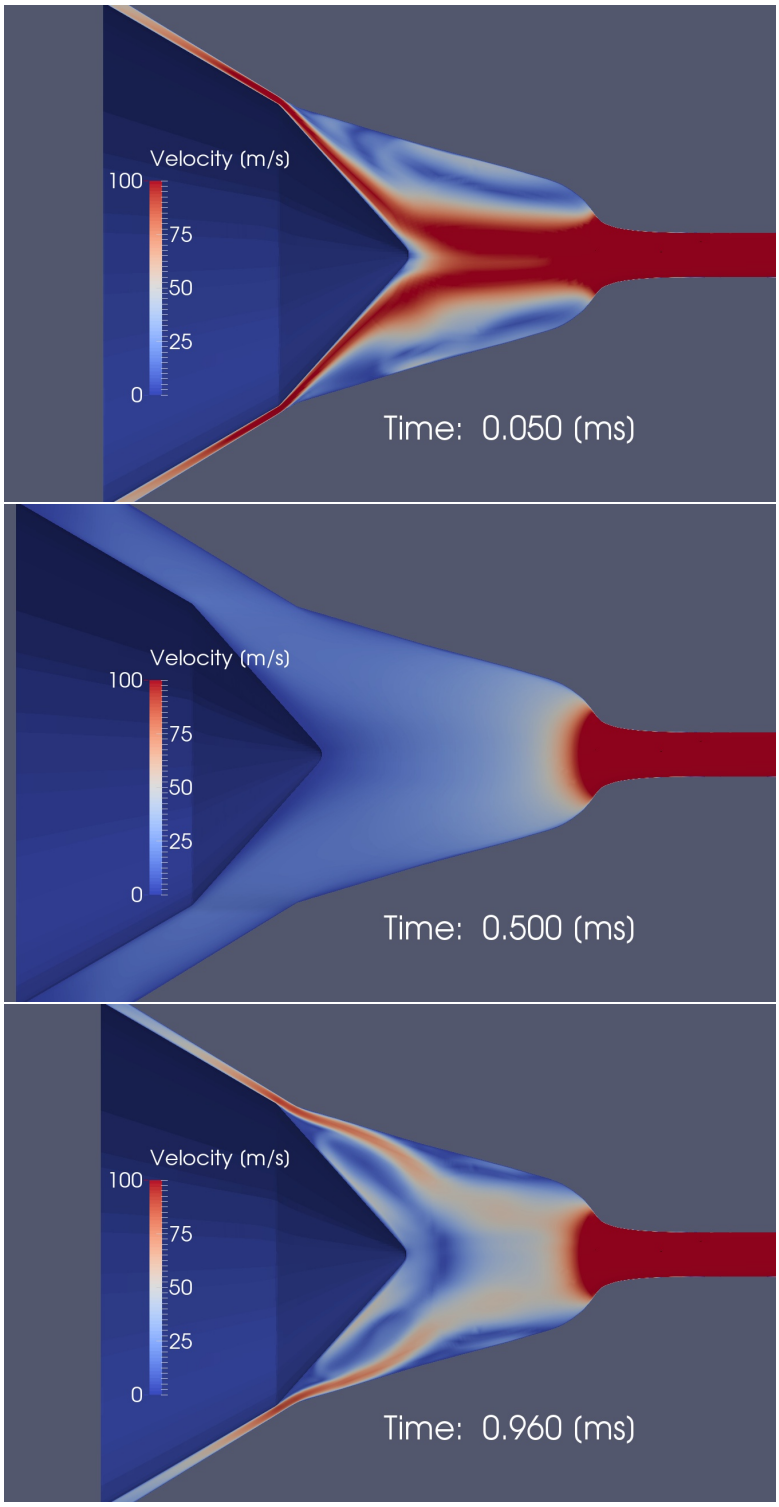

Figure 6.23: Coanda effect observed at low needle lift during the beginning (top) and end (bottom) of injection.

flow towards the wall, at which point a boundary layer develops and the flow becomes attached. As the needle lift increases, so does the speed of the upstream flow, resulting in boundary layer separation and the termination of the Coanda effect.

This interesting internal flow dynamic has no measurable effect on the external spray. This is because the long converging nozzle results in a fairly uniform exit condition. In a cavitating nozzle with sharp inlet corners, however, these internal dynamics may play a large role on the behavior of the spray. It has been shown that the directionality of the flow upstream of the sharp inlet corner can significantly influence the cavitation and turbulence which is generated in the nozzle [6]. An interesting outcome of a future study will be observing the influence of these internal flow dynamics on the ECN spray C injector, which shares the nozzle wall and needle topology, while having a sharp, cavitating inlet corner.

6.3.2.5 Fuel Temperature Analysis

Although upstream fuel temperature can be measured experimentally, it is difficult to characterize the temperature change which occurs as the fuel passes through the nozzle. These temperature changes may influence the characteristics of the spray; the study of Pei et al. suggests that fuel temperature has a profound impact on liquid length [148]. For this reason, a fuel temperature study was conducted, first through a thermodynamic conservation of energy analysis, and then through CFD simulations.

The steady-state mass flux averaged temperature of a fluid exiting a nozzle can be estimated through a simple thermodynamic conservation of energy analysis. Assuming that the nozzle walls are no-slip and adiabatic, the total energy entering the nozzle will be equal to the total energy exiting the nozzle. This total energy is comprised of internal energy, pressure-volume potential energy, and kinetic energy. Assuming negligible kinetic energy at the inlet yields Eqn. 6.2.

$$e_1 + p_1 v_1 = e_2 + p_2 v_2 + 0.5 U_2^2 \tag{6.2}$$

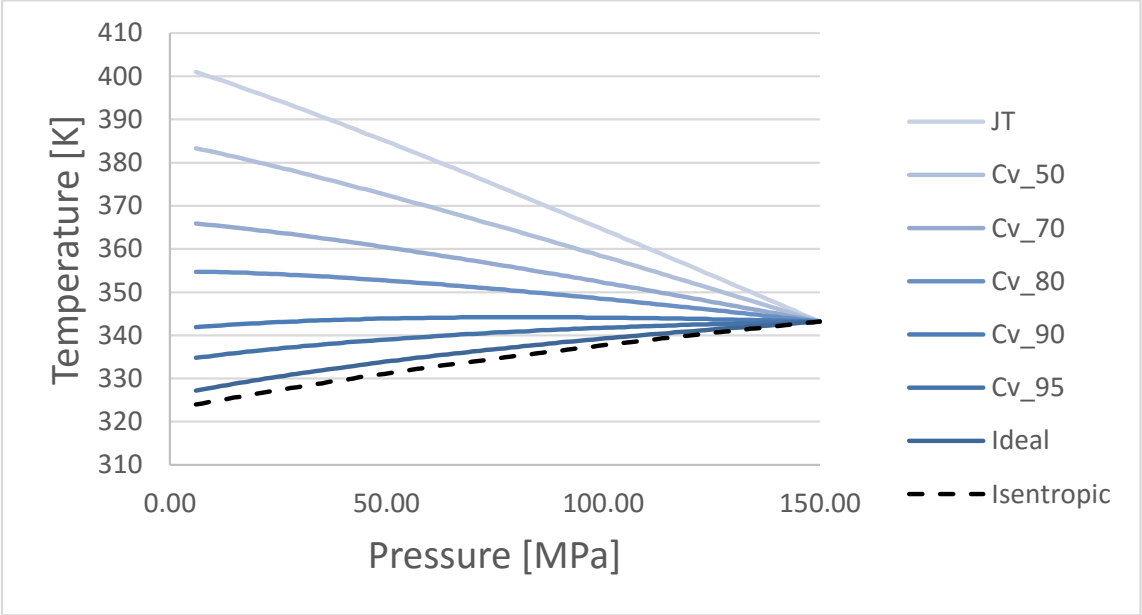

Figure 6.24: Temperature change of n-dodecane subjected to a pressure drop. Based upon a control-volume energy analysis of steady-state flow with no-slip, adiabatic walls and varying degrees of realized kinetic energy.

Using a highly accurate equation of state, such as the one developed by Lemmon and Huber [102], a range of expected fuel exit temperatures can be then be derived, as seen in Fig. 6.24. Here temperature changes across a 150 to 6 MPa pressure drop are shown for processes of varying efficiency. Efficiency is quantified here by a velocity coefficient, representing what percentage of the ideal velocity derived by Eqn. 6.1 is achieved. The JT curve stands for Joule-Thompson, which corresponds to the temperature change experienced through an adiabatic throttling process where none of the pressure drop is realized into kinetic energy. This is equivalent to a coefficient of velocity equal to zero. The ideal curve stands for the expansion process in which all of the pressure-volume potential energy is converted into kinetic energy and $e_1 = e_2$. A curve is also shown for isentropic expansion, showing that even the "ideal" path results in slight generation of entropy and increase in temperature.

The viscous heating effect shown by the JT curve can be quite significant, resulting in a 58 K increase across a 150 MPa pressure drop. An equivalent analysis for a 300 MPa pressure drop predicts a 116 K temperature rise. When a pressure drop is used to generate kinetic energy, as it is in a fuel injector, the temperature change can be much more mild and even decrease in some circumstances. This suggests that the bulk flow of the fuel in the center of the nozzle hole may experience a decrease in temperature compared to the inlet, while the slower regions of the flow near the boundary will experience a great deal of viscous heating and temperature increase.

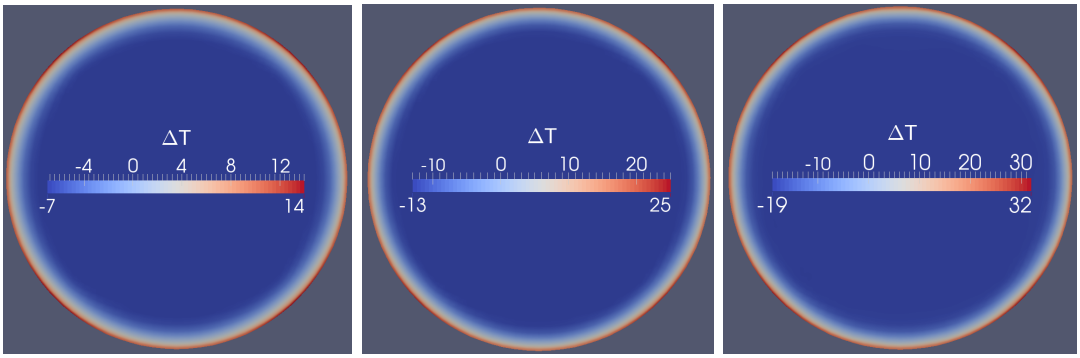

Figure 6.25: Temperature change at the nozzle exit for the 50 MPa (left) and 100 MPa (center) and 150 MPa (right) n-dodecane simulations.

The CFD simulations conducted confirm this analysis and provide insight into the magnitudes and locations of these temperature changes. As shown in Fig. 6.25, compared to the inlet fuel temperature, the nozzle exit temperature for the 150 MPa spray D simulation predicts a 32 K increase in the boundary layer and a 19 K decrease in the bulk flow, a 25 K increase in the boundary layer and 13 K decrease in the bulk flow are predicted for the 100 MPa case, and a 14 K increase in the boundary layer and 7 K decrease in the bulk flow are predicted for the 50 MPa case.

At the end of the injection event, as the needle closes, significant local heating of the fuel is observed in the seat region of the nozzle. This is shown in Fig. 6.26. This viscous heating effect will have an influence on vapor generation within the sac after

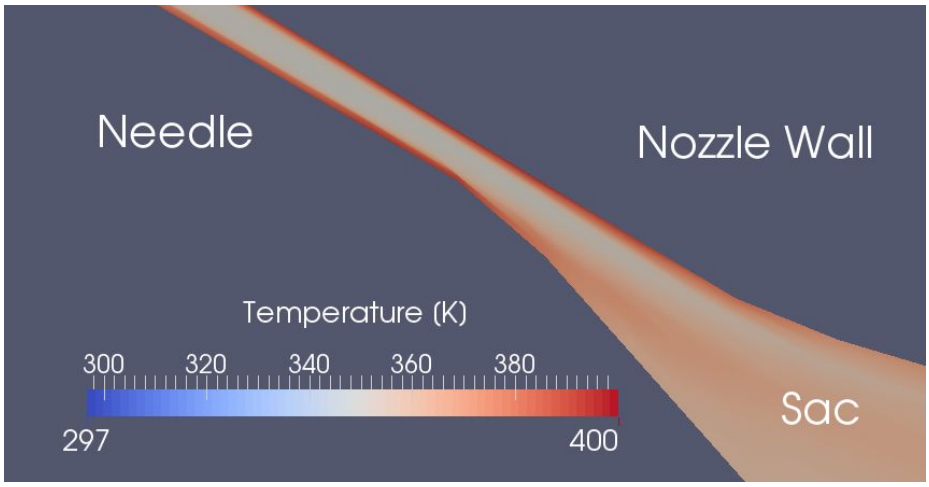

Figure 6.26: Temperature in the nozzle seat region at the end of injection for the 100 MPa target case.

the needle closes, with the hot regions of the fuel potentially dictating the location of vapor formation.

6.3.3 Summary

First, an analysis was conducted on velocity, discharge, and area coefficients using steady-state mass and momentum flux measurements from the CFD simulations and from the experimental data used in Ref. [144]. The agreement demonstrated between experiment and simulation was very good.

The influence of flash-boiling was then investigated through simulations of n-pentane into low ambient pressure. Flash-boiling is also shown to decrease C_d and C_a while having no influence on C_v. A P_a/P_s ratio of 0.8 is shown to have little influence on the spray angle, while a ratio of 0.3 dramatically increases the spray cone angle to a 25°. As will be shown in section 7.1, the influence of flash-boiling here is very similar to that observed in 2D axisymmetric, sharp inlet corner nozzles.

Rate of injection and momentum flux profiles were investigated for simulations with transient needle lift. Needle motion was found to have little influence on the ROI beyond 100 μm of lift. At needle lifts below 200 μm, the internal flow exiting the

needle seat region exhibits the Coanda effect, demonstrating a tendency to attach to either the wall of the nozzle or needle.

Finally, fuel temperatures at the nozzle exit and within the seat region of the nozzle at low lift are shown and a thermodynamic analysis was conducted to inform the CFD results. Significant viscous heating occurs at low needle lift at the end of injection, resulting in fuel temperatures in excess of 400 K. These heating effects would be increased at higher injection pressures.

6.4 Conclusions

The studies conducted with the $\Sigma - Y$ atomization model demonstrate that excellent density distribution, penetration, and velocity profile results can be obtained for a wide variety of injection conditions. The coupled internal/external investigation showed that modeling the internal flow provides only a marginal benefit when the injector is symmetric, non-cavitating, and highly turbulent. Under these conditions, the nozzle outlet flow can be approximated without actually simulating the internal flow. This is not the case, however, when the injector is cavitating or asymmetric, and here Eulerian CFD modeling is a powerful tool for linking the influence of internal flow to the external spray.

The simulations conducted on the spray D geometry illuminated the influence of transient needle motion on a converging diesel injector. They showed that the magnitude of the rate of injection and momentum flux are not influenced by the needle position once it lifts beyond 100 μm. Viscous heating is shown to create hot boundary layers along the nozzle walls during injection, and at low needle lift the viscous heating in the needle seat region is very high. A simple thermodynamic energy analysis in conjunction with an accurate equation of state is shown to be able to produce accurate mass flux averaged exit temperatures.

CHAPTER 7

CASE STUDIES: GASOLINE DIRECT INJECTION

In recent years there has been a trend in the automotive industry towards the use of GDI engines. This injection configuration allows for more control over the combustion process, which leads to increased fuel economy. While GDI engines have developed significantly since their inception, there is still work to be done. The desire to further reduce emissions and maximize fuel efficiency demands continued improvement.

The geometries of GDI injectors are typically quite elaborate; multi-hole stepped valve covered orifice (SVCO) injectors are common. This, in conjunction with the high injection pressures, leads to turbulent flows which often exhibit slight asymmetry and hole-to-hole variation as they leave the nozzle [22, 184]. Furthermore, as the liquid fuel is injected it can undergo phase change through cavitation, flash-boiling, and/or evaporation. Significant research has been done to understand the highly turbulent, cavitating, and evaporating sprays present in direct injection (DI) diesel engines, and while there is some overlap between diesel DI and GDI, it is the added factor of phase change through flash-boiling that makes GDI research especially challenging.

This chapter will cover two CFD studies conducted to investigate GDI injection. First, a 2D parameter study is discussed, addressing the influence of counterbore depth, flashing intensity, and injection pressure on simple axisymmetric geometries. Then, a detailed 3D SVCO geometry is considered at both mildly flashing and non-flashing conditions. Here the internal flow dynamics and their influence on the near-field spray are investigated.

7.1 2D Axisymmetric Parameter Study

Modern GDI injectors contain multiple nozzle holes. This means that each nozzle hole is typically asymmetric in regards to the upstream sac geometry and fluid flow. In order to simply the factors influencing the downstream spray, experiments and simulations are often conducted on single-hole axisymmetric geometries. This is the approach taken here. In order to better understand the influence of counterbore depth, (P_s/P_a) ratio, and pressure drop on direct injection sprays, a parameter study was conducted using a diffuse interface, Eulerian CFD solver.

7.1.1 Case Setup

Three axisymmetric nozzles were tested and they are displayed in Fig. 7.1. The nozzle hole diameter and counterbore diameter are 167 and 390 μm respectively. These dimensions are similar to that of the multi-hole ECN spray G SVCO nozzle. On each of these nozzles, 6 simulations were conducted. These are outlined in Table 7.1.

Figure 7.1: Three nozzles geometries tested with varying counterbore depths.

The simulated fuel was n-pentane at 84 °C. At this temperature, the saturation pressure is 407 kPa. The turbulence model used was the SST k-ω RANS model, and the simulations were run until they reached steady-state.

7.1.2 Results and Discussion

The results from the parameter study in terms of C_d vs. P_a/P_s ratio are shown in Fig. 7.2. It is interesting to observe that the curves for the 20 and 5 MPa pressure drop cases intersect, with the 20 MPa pressure drop simulations being more efficient

Table 7.1: Conditions for the 6 simulations conducted on each of the three axisymmetric geometries.

P_a/P_s [-]	ΔP [MPa]	U_{theo} [m/s]	ρ_a [kg/m^3]	P_a [kPa]
1.5	20	268	6.9	611
0.8	20	268	3.7	325
0.3	20	268	1.4	122
1.5	20	134	6.9	611
0.8	20	134	3.7	325
0.3	20	134	1.4	122

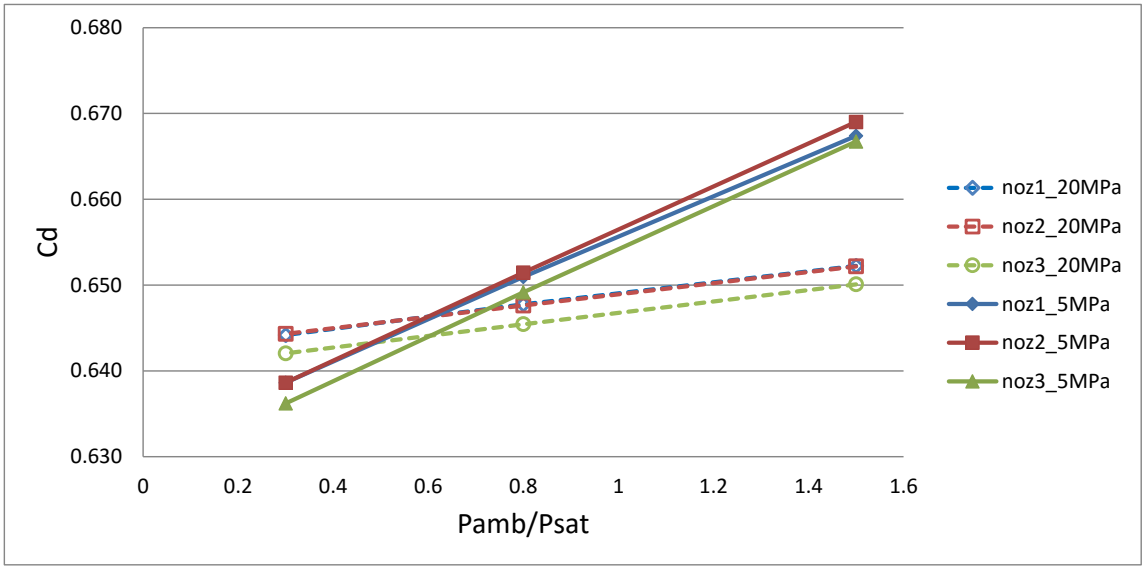

Figure 7.2: Coefficient of discharge plotted against the P_a/P_s ratio.

under hard-flashing conditions and less efficient in mild-flashing and non-flashing conditions.

Fig. 7.3 provides some insight into this result. Here C_d is plotted against the square root of the K_{cav} non-dimensional number. According to the one-dimensional cavitating flow model introduced by Nurick [131], one would expect the discharge coefficient to vary linearly with this term, as per equation, 7.1. Nurick's model assumes a constant contraction coefficient of 0.62 for round nozzles with a sharp inlet.

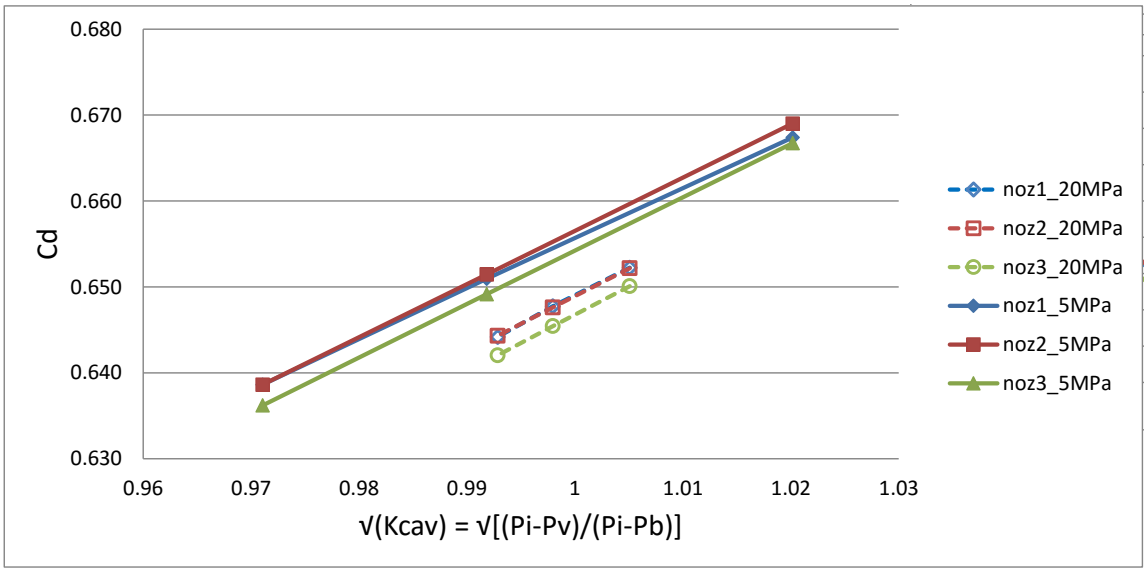

Figure 7.3: Coefficient of discharge plotted against $\sqrt{K_{cav}}$.

$$C_d = C_c\sqrt{K_{cav}} \tag{7.1}$$

It appears, however, that the contraction coefficient is neither constant nor equal to 0.62 for these simulations, but rather a function of the magnitude of the pressure drop. This is not surprising for two reasons. First, the flow here is flash-boiling. Second, the liquid flow in these simulations is largely isolated from the nozzle walls by the vapor generated at the inlet corner. The analysis conducted by Nurick assumed the flow was cavitating and that the liquid had re-attached to walls prior to exiting the nozzle [131]. His model therefore, do not apply to these simulations.

It should be noted that nozzle 3, which does not have a counterbore, has the lowest discharge coefficients. This is because the nozzle effectively has a larger l/d, allowing for greater re-attachment of the flow and more viscous loss.

The spray cone angle was calculated by determining the angle below which 95% of the fuel mass exits the domain. These results are shown in Fig. 7.4. Here it can be seen that the P_a/P_s ratio of 0.3 results in hard flashing and an increase in the spray

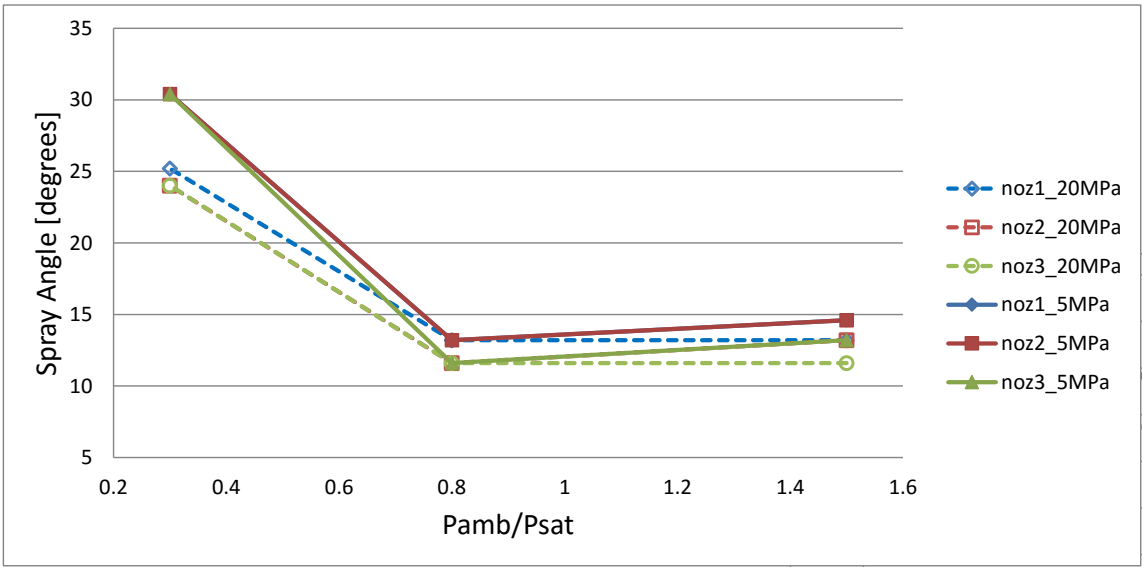

Figure 7.4: Spray cone angle plotted against P_a/P_s.

angle. This increase is more dramatic in the 5 MPa pressure drop cases, where flow velocities are lower and the acceleration due to flash-boiling is able to more effectively change the direction of the spray.

It is interesting to note that the spray angle changes very little from the 1.5 to 0.8 P_a/P_s ratio cases. This is because the decrease of P_a/P_s from 1.5 to 0.8 not only causes a mild flashing effect, but it also results in a decrease in ambient density. The decrease in ambient density serves to decrease the spray angle and the onset of flash-boiling serves to increase it. Under these conditions, the two competing effects appear to balance one another out.

An overview of the simulations conducted can be seen in Figs. 7.5 and 7.6. In Fig. 7.5, the influence of a change in back pressure can be seen as the 20 MPa pressure drop cases on nozzle 1 are shown with all three P_a/P_s ratios. Note that in all of these cases, ambient gas is ingested into the counterbore. Fig. 7.6 shows the hard-flashing, P_a/P_s of 0.3 cases under a pressure drop of 5 MPa. Here it can be seen that the counterbore has little influence on the spray angle. It is interesting to note, however, that the spray under these conditions contacts the counterbore of nozzle 1,

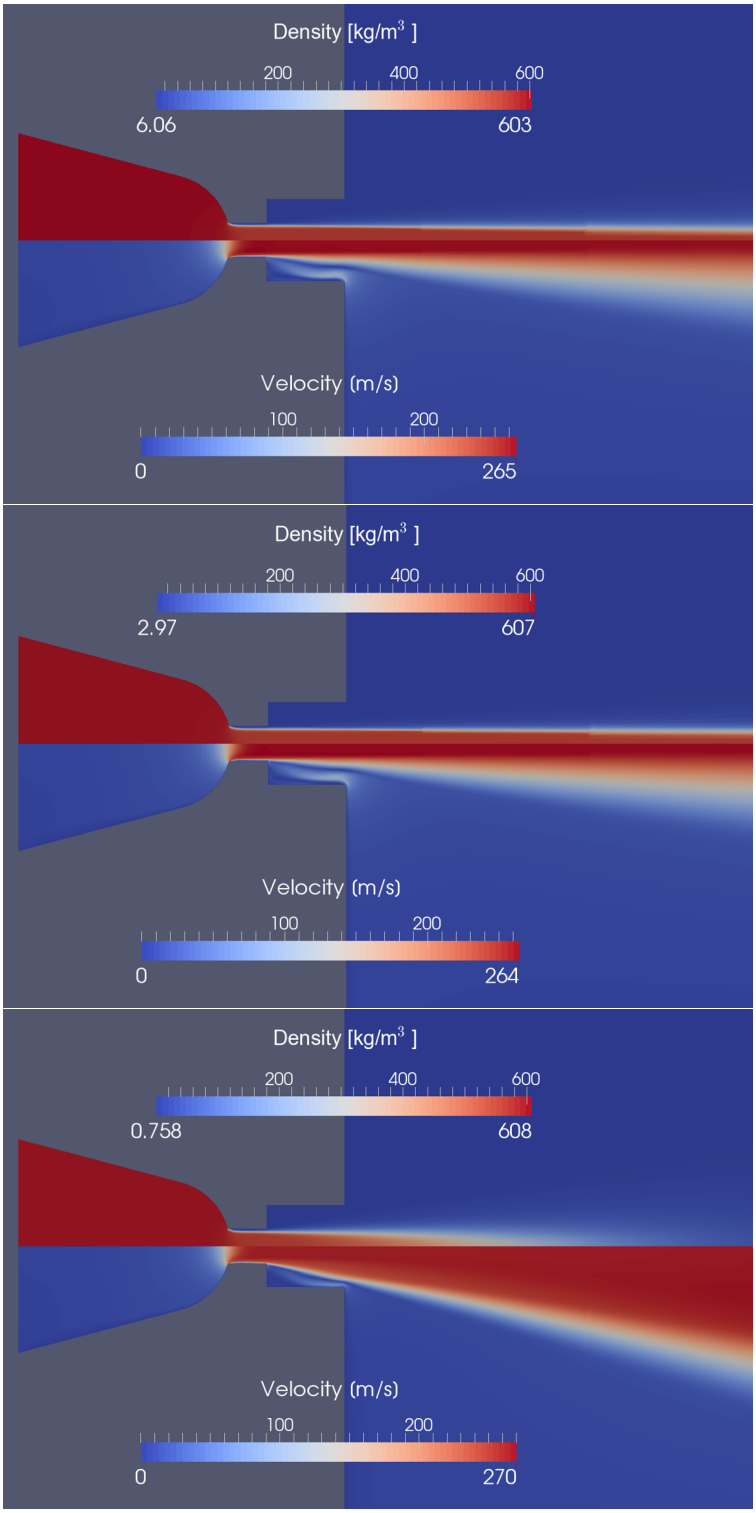

Figure 7.5: The three 20 MPa pressure drop cases on nozzle 1 for non-flashing (top), mild-flashing (middle), and hard-flashing (bottom) conditions.

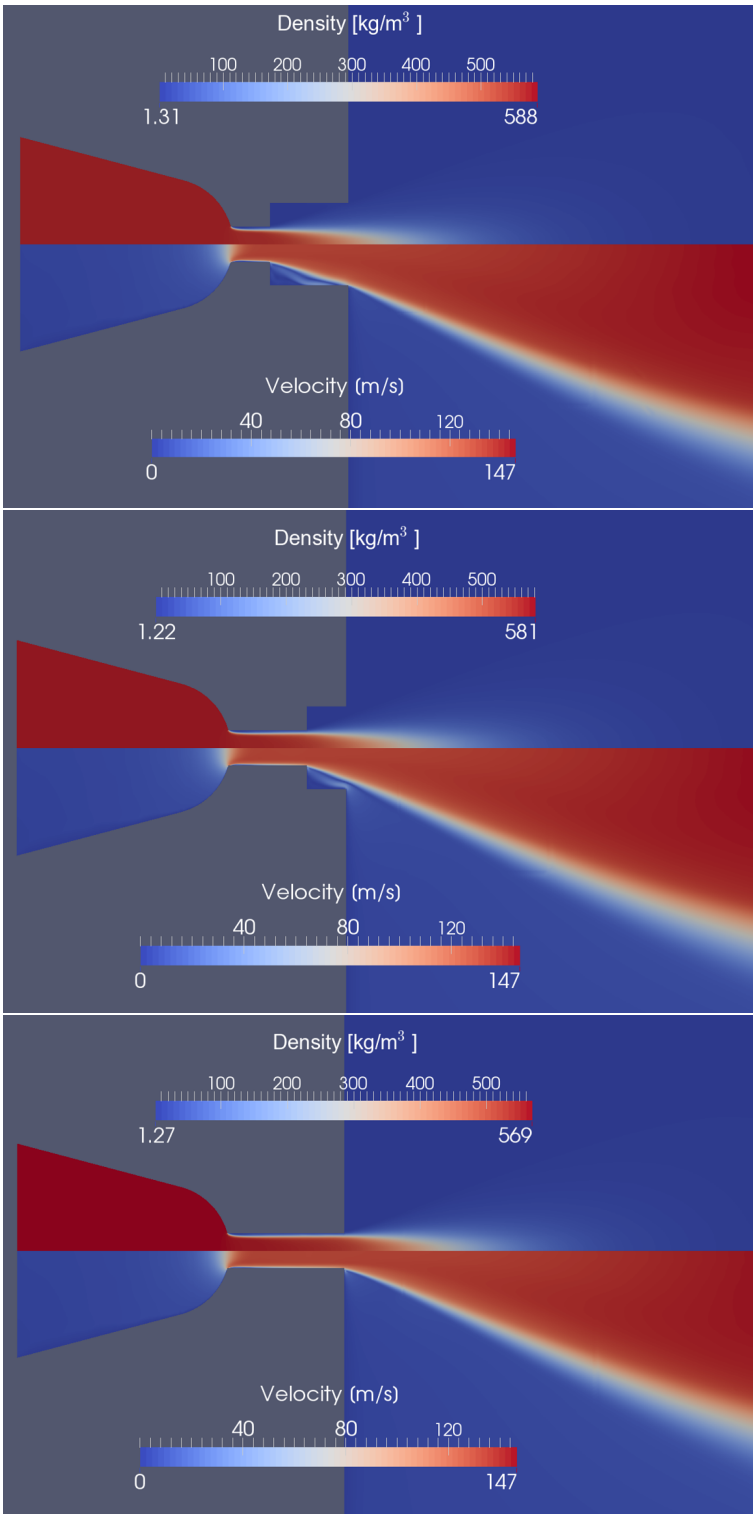

Figure 7.6: The 5 MPa pressure drop, hard-flashing cases on nozzles 1 (top), 2 (middle), and 3 (bottom).

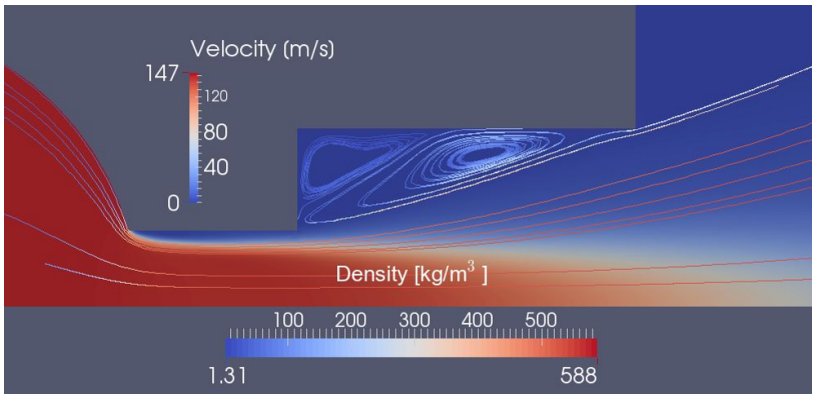

Figure 7.7: Recirculating flow observed in the in counterbore of nozzle 1 under hard-flashing conditions and a 5 MPa pressure drop.

resulting in recirculating vapor flow within the counterbore, as shown in Fig. 7.7. Predicting and preventing fuel contact with the counterbore may be an important step in preventing fouled nozzles as liquid fuel residue on the nozzle tip can result in carbon buildup.

7.1.3 Summary

This parameter study has shown the following:

- Flash-boiling increases the spray angle under hard flashing conditions.
- The influence of mild flashing is not seen in the near-field in terms of spray angle, as the change in ambient density serves to balance the flashing effect.
- A decreased in P_a/P_s results in a decrease in the discharge coefficient.
- Similar to what is expected from 1D cavitating flow analysis [131], a linear dependence of C_d on $\sqrt{K_{cav}}$ is shown. Under these conditions, however, C_c does not appear to be constant, but rather a function of Reynolds number.
- The presence of a counterbore has little influence on symmetric, sharp inlet nozzles.

7.2 Simulating the ECN Spray G Multihole Nozzle

In this section a computational study investigating the influence of transient needle motion on internal nozzle flow and near-field sprays for gasoline direct injection is described. The inclusion of transient needle motion makes this a novel CFD study in the application of GDI sprays. Both flashing and non-flashing conditions are simulated. Grid resolution within the nozzle holes and sac of the injector is significantly higher in this study than in the previously published diffuse interface GDI studies. This has allowed for excellent qualitative agreement with experimental imaging and quantitative agreement with experimental rate of injection, and it has elucidated the complex internal flow which is behind perturbations and oscillations in spray angle and mass flow rate.

7.2.1 Case Setup

7.2.1.1 Mesh

The mesh used for these simulations was based upon the nominal geometry and contained a 9 mm diameter outlet plenum. This is an 8 hole SVCO injector with 5 needle-guides, resulting in geometry which is symmetric across the xz-plane as can be seen in Fig. 7.8. The designed clearance between the needle and needle-guides is around 3 μm, however for this study the clearance has been expanded to 30 μm to prevent the zero thickness cells which would result from the needle wobble. It is certain that this clearance deviates from the nominal value, and this will be investigated in future work.

The total cell count was 1.44 million with a minimum cell size of $\sim$7 μm. No grid independence study was conducted, however, the cell count is comparable to or higher than that of other diffuse interface simulations reported in literature [121, 160, 161]. Furthermore, the mesh is significantly better resolved within the sac and nozzle hole regions than these studies; the grid spacing is roughly 10 μm and 7 μm in the sac

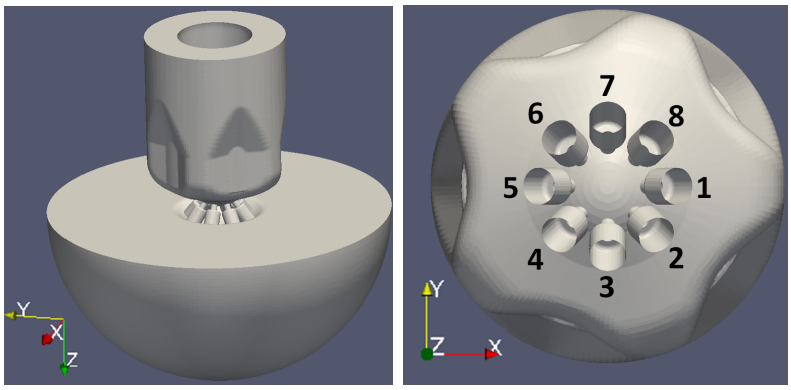

Figure 7.8: Nominal spray G nozzle geometry with 8 nozzle holes and 5 needle-guides. Simulated domain includes 9 mm diameter outlet plenum. Hole numbering and axes orientation based upon ECN convention [1].

and nozzle holes respectively, compared with the ∼30 μm and ∼15 μm reported by Saha et. al. [160], and ∼40 μm and ∼10 μm reported by Moulai et. al. [121]. Both of these works conducted a rate of injection (ROI) based grid independence study.

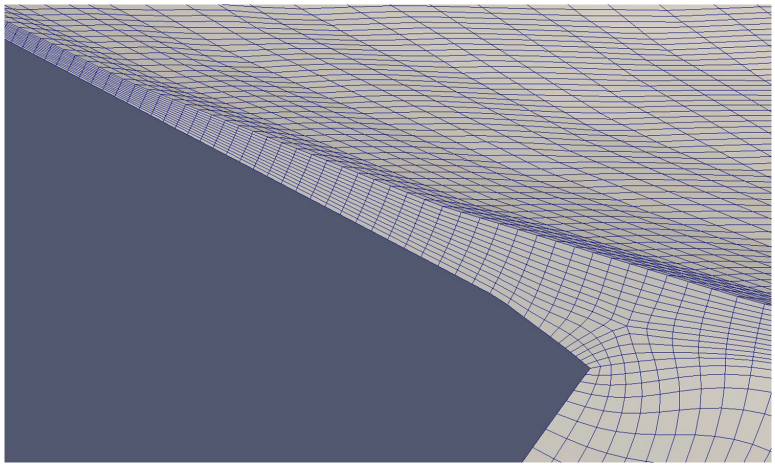

Figure 7.9: Cut plane of CFD mesh prior to needle lift. Anisotropic refinement can be seen in the narrow region between the needle and the nozzle.

The mesh was generated using GridPro meshing software which produced a high quality mesh and allowed for anisotropic refinement in the narrow 5 μm channel between the needle and the nozzle wall. This can be observed in Fig. 7.9. Without

anisotropic refinement, the cell count for this mesh would be closer to 18 million, with most of the cells located within the 5 μm narrow channel.

7.2.1.2 Needle motion

A realistic three-dimensional needle motion profile has been applied in the simulations from measurements made via time-resolved X-ray phase contrast imaging. The experiments were conducted at the 32-ID beamline of the Advanced Photon Source (APS) at Argonne National Laboratory [174]. The injector was placed in a pressurized chamber fitted with X-ray transparent windows. A polychromatic X-ray beam was passed through the nozzle, and the internal components of the injector were imaged on a scintillator screen, which was recorded using a conventional high-speed camera and 10× microscope with a spatial resolution of 1.9 μm/pixel and a temporal resolution of 8.33 μs. Further details regarding the experiment setup may be found in prior work [49, 85, 152, 199]. The motion of the needle was recorded at two orientations of the injector in two regions at the front and back of the check ball, as shown in Fig. 7.10. From 30 realizations of the needle motion at each location and orientation, the ensemble average three-dimensional motions were calculated using an image correlation algorithm.

The ensemble average needle lift and off-axis wobble profiles are shown in Figs. 7.11-7.12 respectively, using the ECN coordinate convention [1]. It can be seen that the needle wobbles in both the x and y directions, and at the same frequency. Analysis of the individual wobble profiles suggests that this may be occurring because the needle is influenced by fluid-structure interactions or that it may be physically contacting the needle guides. Due to the small magnitude of the wobble, the uncertainty in these measurements is relatively large. Further investigation is required to understand the physical mechanism of the wobble. Regardless, this wobble motion is fundamentally different from what is observed in diesel injectors, where the

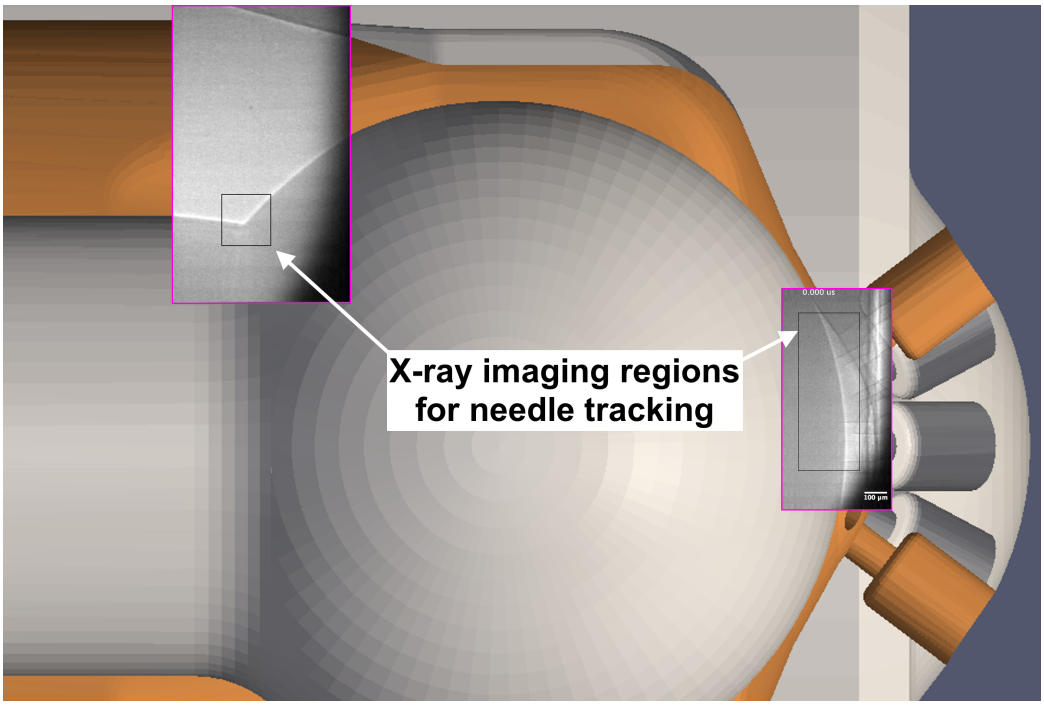

Figure 7.10: Cutaway of Spray G injector nominal geometry, with X-ray imaging regions overlaid. X-ray experiments conducted by Dr. Daniel Duke at Argonne National Lab.

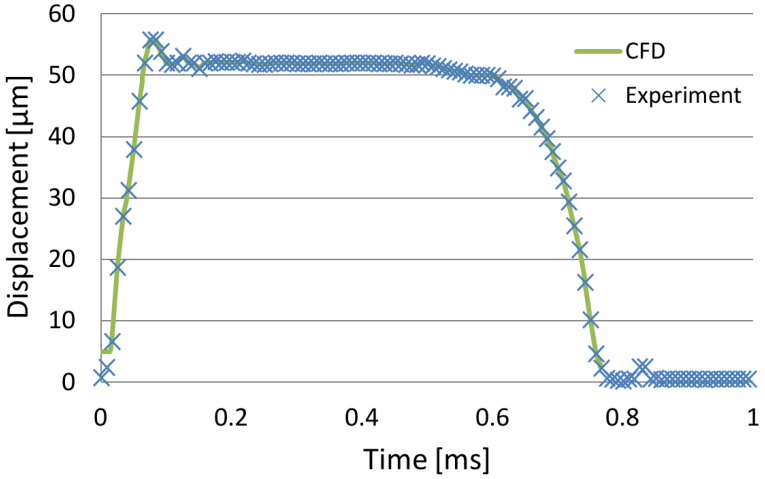

Figure 7.11: Ensemble-averaged needle lift (z-axis) profile from the X-ray data (blue Xs) and the lift profile used in the CFD simulations (green line). Notice that the CFD profile starts at 5 μm of lift.

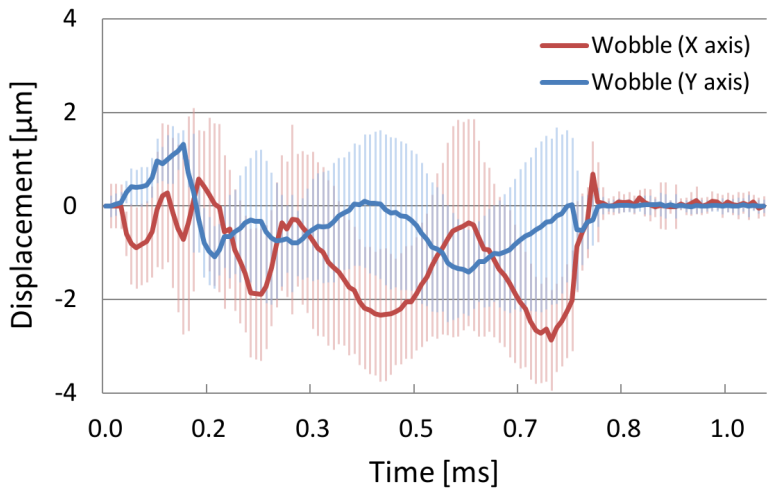

Figure 7.12: Ensemble-averaged needle wobble profile with 86% confidence interval bars. Data provided by and used with permission from Dr. Daniel Duke, Argonne National Lab.

wobble is purely mechanical oscillation [115], and wobble velocity and magnitude are significantly greater.

Since the simulations require a finite positive initial needle lift, the motion used in the simulations was modified accordingly. The needle position started at 5 μm of lift and remained stationary until 14 μs into the simulation. The time of 14 μs was chosen because this was the amount of time the experimental data indicated it would take to reach 5 μm of lift. After this point, the needle position followed the experimental lift and wobble profile generated by the experiment. The internal mesh moved with Laplacian smoothing. To isolate the effects of the needle wobble, simulations were also done only with lift.

7.2.1.3 Initial and boundary conditions

The simulations conducted for this study were based upon the engine combustion network (ECN) spray G and spray G2 operating conditions described in Table 7.2. The spray G condition is non-flashing due to its elevated back pressure and the spray G2 is mildly flashing.

Table 7.2: Non-flashing (spray G) and Flashing (spray G2) operating conditions defined by the ECN [1].

	Spray G	Spray G2
Fuel	Iso-octane	Iso-octane
Upstream Pressure	20 MPa	20 MPa
Fuel Temperature	90°C	90°C
Ambient Temperature	300°C	60°C
Ambient Density	3.5 kg/m^3	0.5 kg/m^3
Back Pressure	600 kPa	50 kPa
P_a/P_s	7.8	0.7
Injection Duration	780 μs	780 μs

The inlet boundary was modeled using a zero gradient boundary condition for velocity and a total pressure boundary condition for pressure. The outlet was modeled as zero gradient for velocity and an in-house transonic total pressure condition was used for pressure. Because the outlet velocities can be supersonic, a total pressure boundary condition is not appropriate. The transonic total pressure condition smoothly transitions from total pressure to zero gradient depending on the Mach number. This boundary condition increased the stability of the simulations.

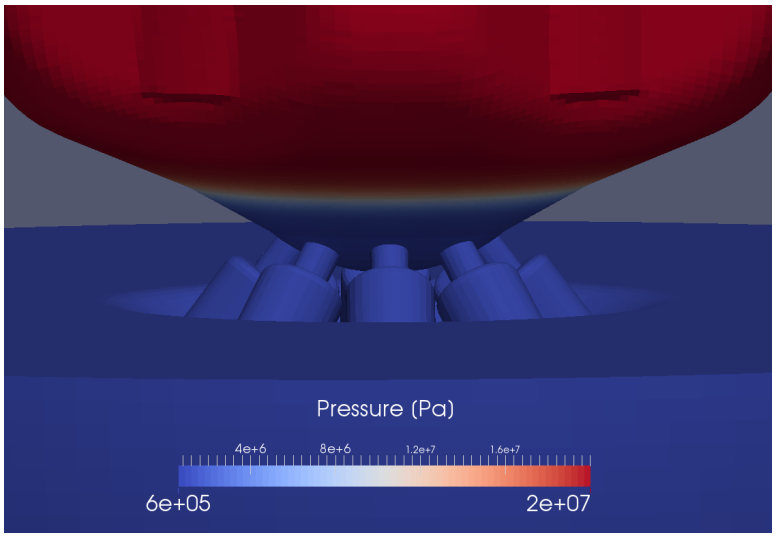

Figure 7.13: Pressure initial condition set with hyperbolic tangent.

As seen in Fig. 7.13, the internal pressure field was initialized using a hyperbolic tangent to drop the pressure in the seat region. The internal field for the non-condensable gas to fuel interface was set at the plane of minimum needle clearance.

Setting the internal fields in this way prevents spurious pressure waves from dominating the beginning portion of the simulation. It also allows for the initial density field to be calculated appropriately, so that the fuel begins with its compressed density of 646 kg/m^3. A comparable simulation which starts with the downstream pressure throughout the domain would result in an initial equilibrium fuel density of 632 kg/m^3, and much of the simulation would include unwanted effects related to the solver working to compress the upstream fuel.

7.2.1.4 Turbulence closure and model assumptions

Turbulence was modeled using the SST k-ω RANS model. This model is known to perform well in adverse pressure gradients and separating flow. Standard log-layer wall functions were used at the wall.

Compressibility of the fluid was a volume weighted average of the compressibility of the three phases, where gas and vapor compressibility were based upon the ideal gas law, and liquid compressibility was assumed to be linear.

The simulation was assumed to be isenthalpic. Throttling processes are often considered isenthalpic, since no work is done by the fluid.

7.2.2 Results and Discussion

7.2.2.1 Rate of injection

ROI profiles were generated for all four cases by integrating the mass flux across the outlet of the injector. These profiles were compared with experimental ROI measurements taken through the long-tube method. These data, in addition to the needle lift profile can be seen in Fig. 7.14. Excellent agreement was observed between

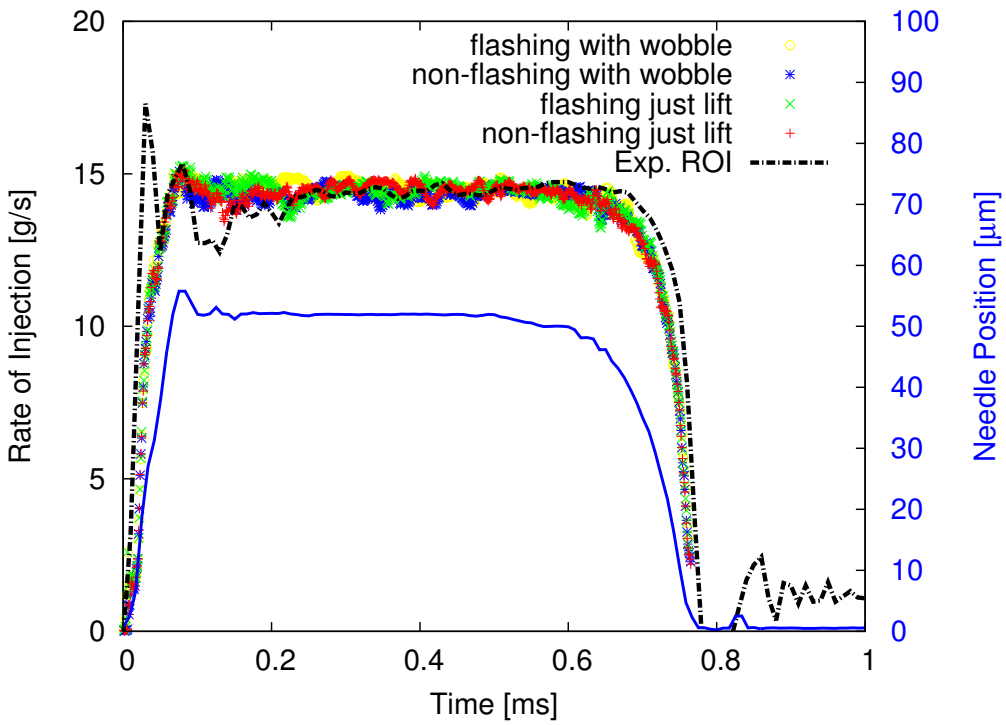

Figure 7.14: Simulated and experimental ROI with needle position vs. time. Experimental ROI obtained through the long-tube method and simulation ROI taken at the nozzle exit.

the simulation ROI profiles and experimental measurements and several interesting observations have been made.

First, in the early portion of the injection the experimental ROI profile is significantly more noisy than the profiles generated from the simulations. Such noise is commonly observed in ROI profiles generated through the long-tube method. It has previously been suggested that this noise does not represent actual fluctuations in the ROI, rather that the noise is due to vibrations in the experimental rig [115]. Our simulation results support this conclusion.

Next, the simulation ROI profiles follow the needle lift profile, even responding to the transient overshoot which occurs just as the needle reaches peak lift. The response to needle lift in the experimental profile is not as pronounced. This is partially due

Table 7.3: Total injected mass for the four CFD cases. Data are colored by magnitude.

	Spray G Just Lift [mg]	Spray G w/ Wobble [mg]	Spray G2 Just Lift [mg]	Spray G2 w/ Wobble [mg]
Hole 1	1.29	1.30	1.28	1.29
Hole 2	1.25	1.25	1.31	1.27
Hole 3	1.26	1.25	1.29	1.28
Hole 4	1.29	1.27	1.27	1.29
Hole 5	1.27	1.29	1.25	1.31
Hole 6	1.27	1.27	1.28	1.29
Hole 7	1.29	1.26	1.27	1.28
Hole 8	1.32	1.29	1.28	1.28
Total	10.24	10.17	10.24	10.29

to the previously mentioned noise, but it is also a consequence of the measurement occurring some distance downstream of the injector in the long-tube method.

Finally, fluctuations of similar magnitude and frequency are observed in all ROI profiles. Analysis of the CFD results reveals that these fluctuations are primarily a result of fuel vapor in the nozzle holes restricting the available exit area, as seen in Figs. 7.24 and 7.27 and described in section 7.2.2.6.

These results provide a quantitative validation of the simulations. They also provide insight into the ROI during the transient start of injection period which is difficult to obtain experimentally. Finally, they show that an accurate ROI profile can be obtained through CFD simulations using total pressure boundary conditions and transient needle lift to actuate injection.

7.2.2.2 Total injected mass

Total injected mass data was obtained by integrating the mass flux throughout the duration of the injection across the outlet of each nozzle hole. This yielded the data seen in Table 7.3. Results agree well with the 10 mg injected mass target specified by the ECN [1]. The hole-to-hole variation in total injected mass is small; on the order of 1-2%. No apparent dependence on the symmetry of the nozzle can be seen,

indicating that the nozzle symmetry is of little importance and that any significant and consistent variation in hole-to-hole injected mass observed experimentally is likely due to manufacturing imperfections in the nozzle. Finally, the needle wobble doesn't appear to influence the injected mass in a consistent way, an idea which will be explored in more detail in section 7.2.2.6.

7.2.2.3 Qualitative validation

The qualitative behavior of these simulations matches well with experiment in three ways.

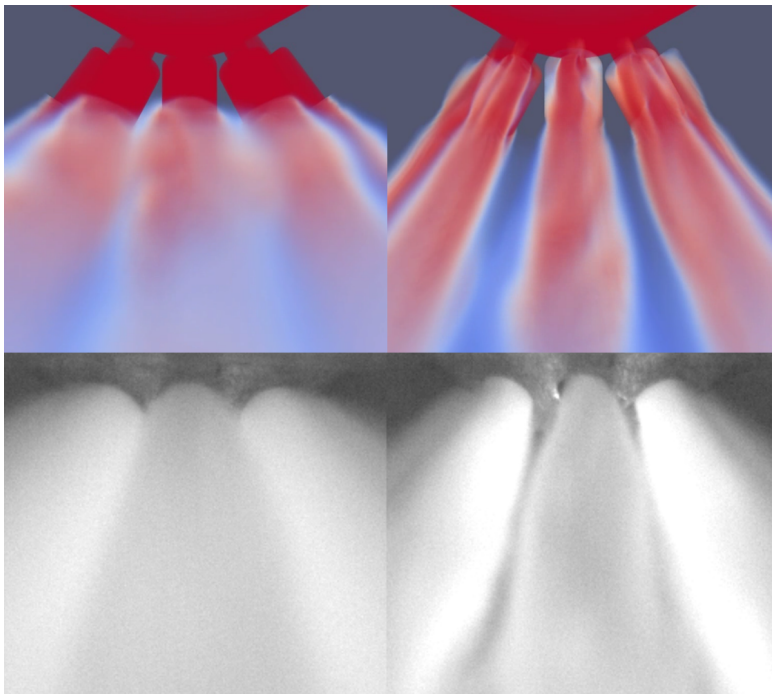

Figure 7.15: Flashing (left) and non-flashing (right) experimental images (bottom) and volume rendered fuel mass fraction from CFD (top) midway through injection. Uniform contact of fuel with counterbore is seen under flashing conditions, while non-flashing shows gaps in contact allowing ingestion of ambient gas. Experimental images provided by and used with permission of Dr. Scott Parrish, General Motors Research and Development.

First, the results for the non-flashing spray G condition predicted ingestion of ambient gas into the nozzle counterbores. In contrast to this, no ingestion of ambient gas

was predicted for the flashing spray G2 condition. This is due to flashing, expanding spray filling the counterbore and preventing ambient gas ingestion. As seen in Fig. 7.15, experimental imaging of flashing and non-flashing GDI injection has shown the

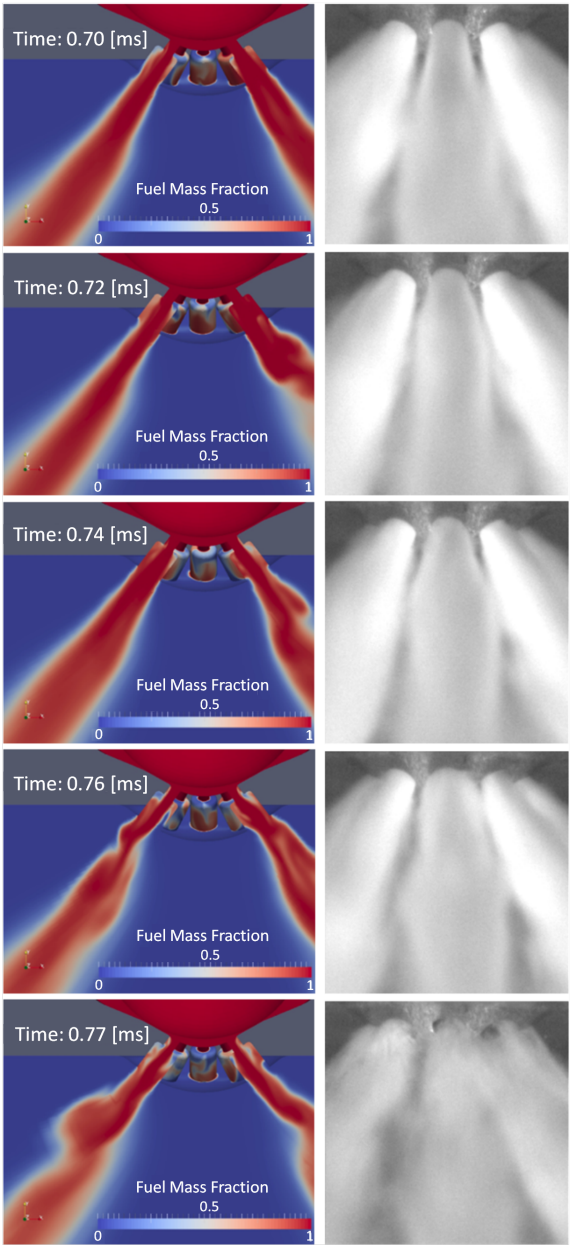

Figure 7.16: Simulated fuel mass fraction compared with experimental imaging at the end of non-flashing simulation. Note that the spray angle increases as flow is disrupted with the closing of the needle. Needle profile shown in Fig. 7.14.

same behavior. The flow pattern in these two conditions is fundamentally different. In non-flashing conditions, the ingestion of ambient gas effectively restricts the exit area of the counterbore, producing narrower spray cone angles. Conversely, in flashing conditions, the exit area of the spray is restricted by the counterbore walls. This has interesting implications for the design of the nozzle, as the geometry is restricting the expansion of the flashing jet. Furthermore, the contact of the spray with the counterbore walls is of particular interest as it can lead to tip wetting and, subsequently, increased emissions and carbon buildup on the injector walls [18].

Next, our simulations predicted an expansion and perturbation of the spray angle at the end of injection. This has been observed through experimental imaging as seen in Fig. 7.16 where the liquid mass fraction is compared with experimental images in the non-flashing condition. Such a perturbation appears to also lead to tip wetting, and the ability to predict this undesirable behavior in CFD simulations could be a helpful tool for fuel injector design.

Finally, when comparing animations from the flashing and non-flashing simulation results to experimental footage, it was found that the frequency and magnitude of the oscillations in the spray plumes match very well. These oscillations in the spray plumes were found to be the result of unsteady flow within the sac influencing the flow characteristics within the 8 holes. This conclusion will be described further in section 7.2.2.6.

7.2.2.4 Flash-boiling at low lift conditions

At low needle lift conditions at the end of injection, very low pressures occur within the injector in the narrow region between the needle and the nozzle wall. The pressure drop here is similar to what is seen in a convergent-divergent nozzle in subsonic or choked conditions. This low pressure causes fuel vapor to be generated as fuel rushes past the needle, as seen in Fig. 7.17.

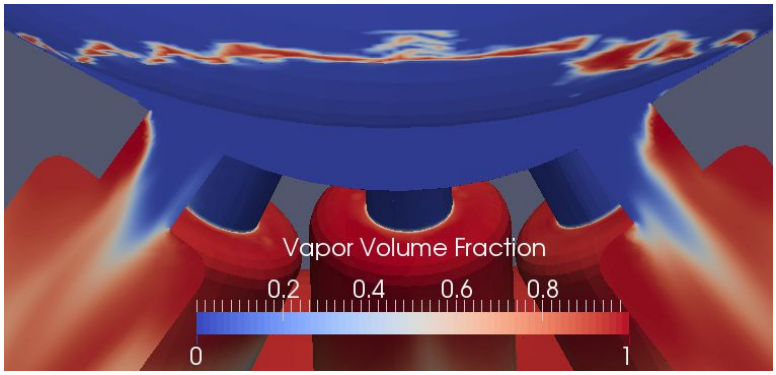

Figure 7.17: Vapor generated at low lift conditions near the end of injection, 0.765 ms after the start of injection in spray G2 simulation.

Vapor generation in this region may influence the post-injection condition of the sac, with the inevitable vapor collapse aiding in the ingestion of ambient gas. Furthermore, it is possible that cold fuel may cavitate in this region of the nozzle, potentially damaging the nozzle walls over time.

7.2.2.5 Needle wobble

Simulations were conducted with and without needle wobble to help isolate any influence the lateral motion of the needle may have had on the spray. While the hole-to-hole variation in mass flow rate did differ from case to case, the variations could not be tied to the needle wobble. A description of the analysis used to reach this conclusion follows.

In order to compare the motion of the needle wobble to the variations in mass flow rate, the center of mass flow was calculated on a set of faces which perpendicularly cut through the middle of each of the 8 nozzle holes. This calculation was done with the two surface integrals shown in Eqn 7.2.

$$\text{center of mass flow} = \frac{\text{first moment of mass flow rate}}{\text{mass flow rate}} = \frac{\iint_S \phi x_i \, dS}{\iint_S \phi \, dS} \tag{7.2}$$

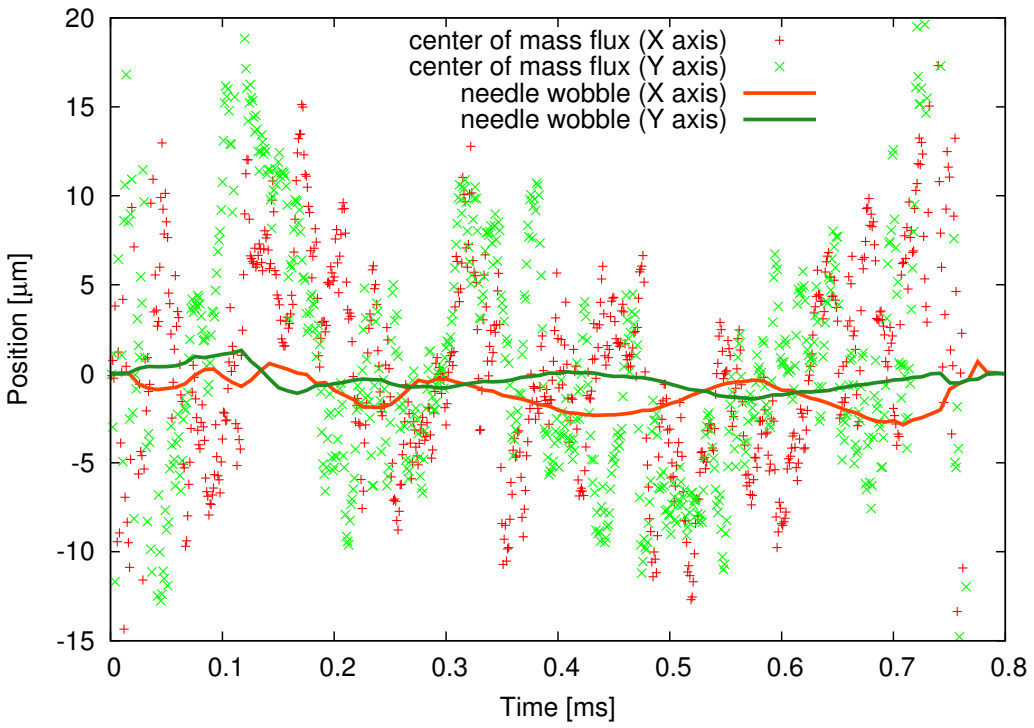

Figure 7.18: Center of mass flow and needle wobble plotted over time for the spray G with wobble simulation.

The center of mass flow rate among the 8 nozzle holes is plotted with the needle wobble in Fig. 7.18. Here it can be seen that the magnitude of the variation in the hole-to-hole mass flow rate far exceeds the magnitude of the needle wobble. Additionally, no significant correlation between the two paths could be found.

This was a somewhat unexpected result as previous works have shown that needle wobble can influence spray structure and mass flow rate in diesel injectors [9]. It is not, however, unexplainable as the spray G geometry differs significantly from that of a diesel injector. First of all, the magnitudes of the lift and wobble in GDI injectors are significantly less than in diesel injectors. This means that needle velocities are lower, with a peak wobble velocity of less than 0.2 m/s in this case. Next, the needle has a spherical tip. This means that the bottom portion of the needle surface is close to parallel to any wobble motion, and thus wobble does not displace any significant

volume of fluid in the nozzle sac. Finally, the magnitude of the wobble is small, around 3 μm. This small and slow wobble results in its most significant displacement of volume far upstream of the nozzle holes, and any influence this motion has on the flow is far overshadowed by the highly turbulent and complex flow which follows further downstream.

It should be noted that the full effect of the needle wobble in the needle-guide region may not be felt in these simulations, as needle to needle-guide clearance has been expanded beyond the nominal clearance to prevent zero thickness cells. Without experimentally measuring the actual needle to needle-guide clearance, it is difficult to estimate the significance of the dynamics in this region. Furthermore, the use of an ensemble averaged wobble profile may have reduced the effects.

7.2.2.6 Complex internal flow

As fuel moves past the needle it accelerates to roughly 140 m/s at full needle lift and close to 250 m/s at low lift. Upon reaching the location of the nozzle holes the fuel then either enters a nozzle hole or the nozzle sac. The viscous losses at this point are small, so the average static pressure in the center of the sac is close to the injection pressure, around 17 MPa. This means that the fuel entering the nozzle sac encounters a strong adverse pressure gradient. This adverse pressure gradient results in the generation of vortices and turbulence as the fuel contends for a path into one of the eight nozzle holes. Analysis of the simulation results reveals that these vortices are transient and interacting, resulting in a complex internal flow which produces hole-to-hole fluctuations in mass flow rate, slight oscillations and variation of the spray angle, consistent flash-boiling at the inlet corner of the nozzle holes, and intermittent string flash-boiling as vortices are entrained into the nozzle holes. Each of these features will be assessed in more detail within this section.

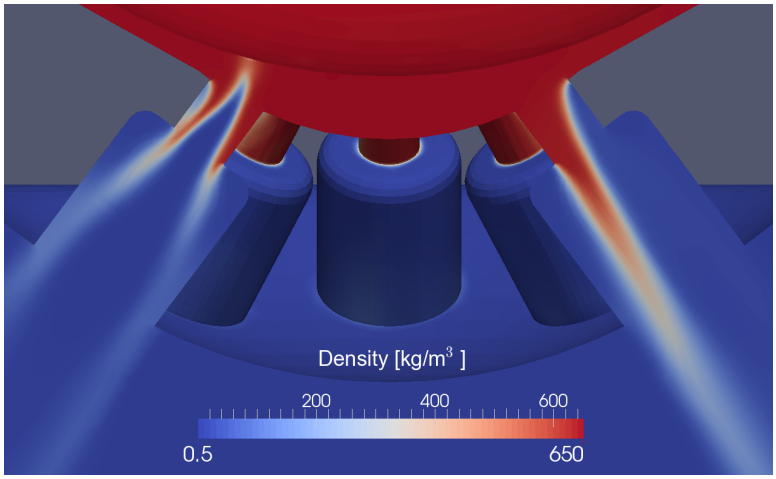

Figure 7.19: Density field 0.339 ms into simulation under flashing conditions. The influence of vapor generation at the inlet corner can be seen. The left nozzle hole is also generating vapor through string flash-boiling.

First, the inlet corners of each of the 8 nozzle holes consistently produces a sufficient pressure drop to generate substantial amounts of fuel vapor. As can be seen in Fig. 7.19, this occurs on the upstream side of the nozzle holes. Here high velocity fuel encounters the hole and a huge pressure drop results as the momentum of the fuel prevents it from following the sharp feature. Vapor generation here is aided by the fact that this simulation was conducted on the nominal geometry which contains sharp inlet corners. The nozzle hole on the left of Fig. 7.19 is also generating vapor through string flash-boiling, a phenomena which will be discussed in detail later in this section.

Next, the flow in the injector sac contains many transient and interacting vortices. These vortices are generated as high speed flow enters the sac from all directions and encounters a strong adverse pressure gradient. The low pressure regions of the nozzle holes continuously pull on the flow, inducing swirl and providing sinks into which the vortices drain. Three types of vortices were commonly observed in these simulations and can be seen with the aid of streamlines and isosurfaces of total pressure in Figs. 7.20 through 7.22:

- **Unterminated:** A vortex which simultaneously drains into two adjacent nozzle holes. The streamlines on Figs. 7.20 and 7.21 help show how this happens; the vortex is fed from the bottom by flow directly upstream of the vortex and fed from the top by sac flow. As the sac flow encounters upstream flow their momentum relative to the nozzle holes cancel out resulting in a vortex which then simultaneously drains into both holes. This type of vortex is semi-stable, typically lasting on the order of 10-20 μs.

- **Semi-terminated:** A vortex which drains into a single nozzle hole, with the other end terminating on the needle of the injector. This is seen in Fig. 7.22. These vortices are fed primarily by upstream flow and they are significantly more stable, lasting on the order of 40-80 μs.

- **Fully-terminated:** A vortex which does not feed into a nozzle hole, terminating on the nozzle wall and the bottom of the needle. This can be seen in the right center of Fig. 7.20. Such a vortex typically either dissipates within 5-10 μs or migrates to a nozzle hole and is re-energized.

The estimated timescales of these vortices were generated from animations of total pressure isosurfaces. It is common for vortices to move around, merge together, and/or split apart, thus transitioning sequentially from type to type.

The behavior of these vortices can be understood more with the help of examination of the helicity of the flow. Helicity is the dot product of the velocity with the vorticity. Thus, it is a signed scalar field which can be useful in determining the direction of the flow rotation. As seen in Fig. 7.23, it is common for two counter-rotating vortices to drain into a single nozzle hole. Co-rotating vortices, on the other hand are unstable and tend to either merge together or break each other apart. To gain a sense of the magnitude of the helicity observed in these simulations, consider that the square of the characteristic velocity (volume flow rate / exit area) divided by

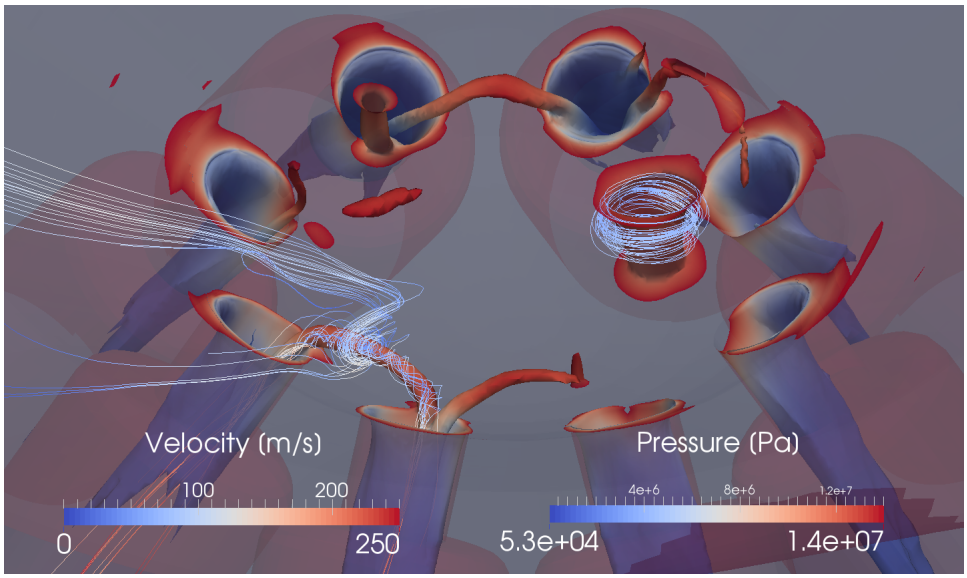

Figure 7.20: Isosurface of 14 MPa total pressure colored by static pressure with velocity streamlines colored by velocity magnitude. Taken midway through flashing simulation. Vorticies contained in the sac can be seen to terminate on a wall or they can be entrained into one or two nozzle holes.

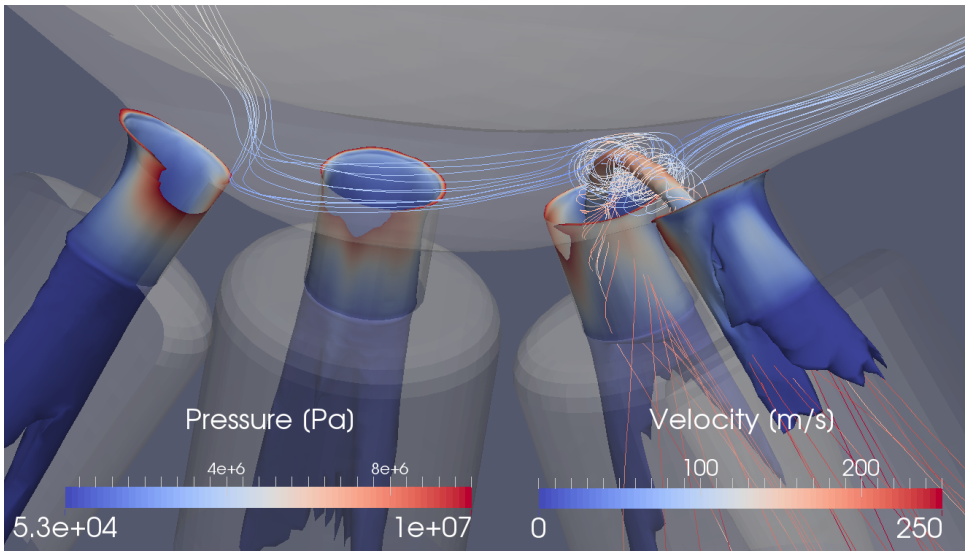

Figure 7.21: Isosurface of 10 MPa total pressure colored by static pressure with velocity streamlines colored by velocity magnitude. Taken midway through flashing simulation.

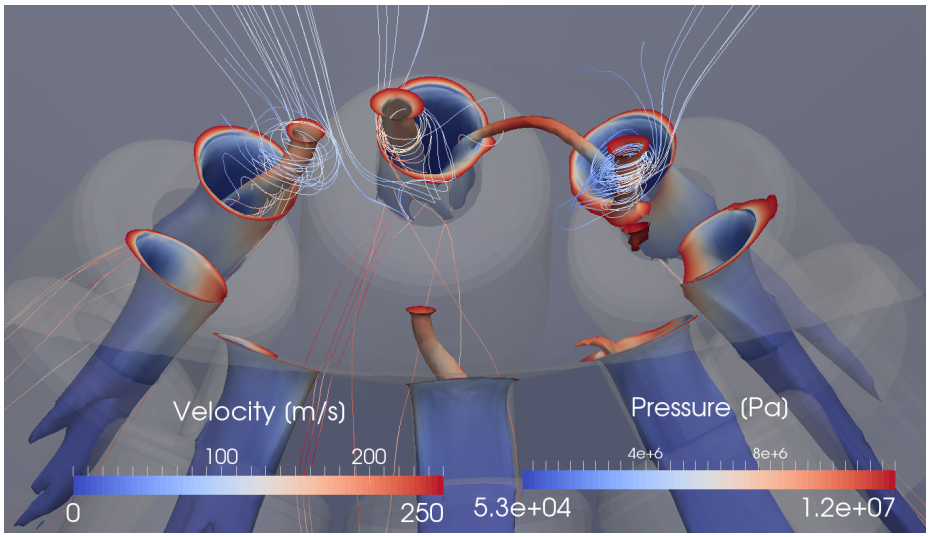

Figure 7.22: Isosurface of 12 MPa total pressure colored by static pressure with velocity streamlines colored by velocity magnitude. Taken midway through flashing simulation.

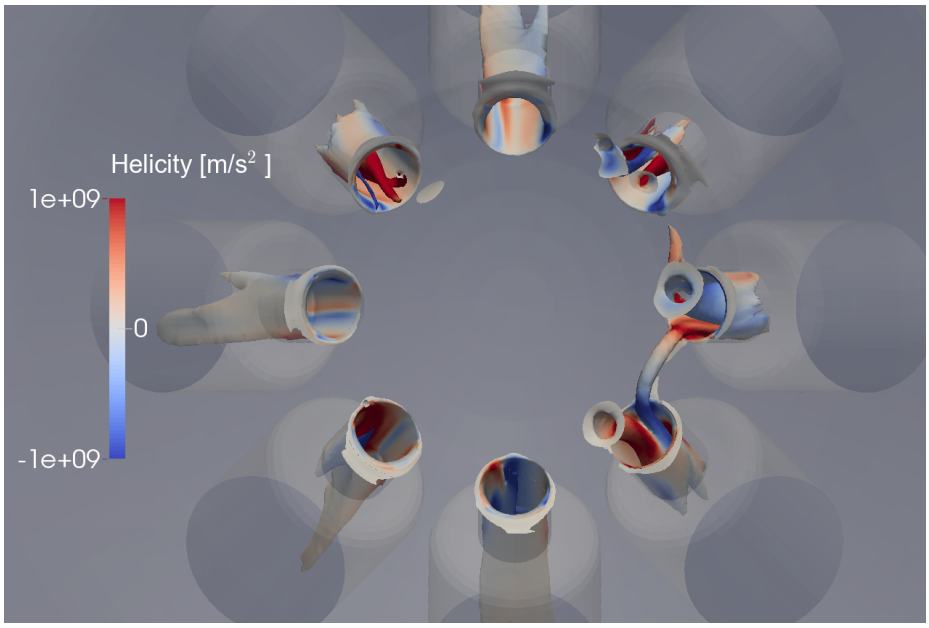

Figure 7.23: Isosurface of 14 MPa total pressure colored by helicity. Note that counter-rotating vortices often drain into the same nozzle hole. Taken midway through flashing simulation.

the hole diameter is about $10^8 m/s^2$. This means that the helicity values are indeed quite strong relative to the mean flow, on the order of +/- 10 times this characteristic normalizing value.

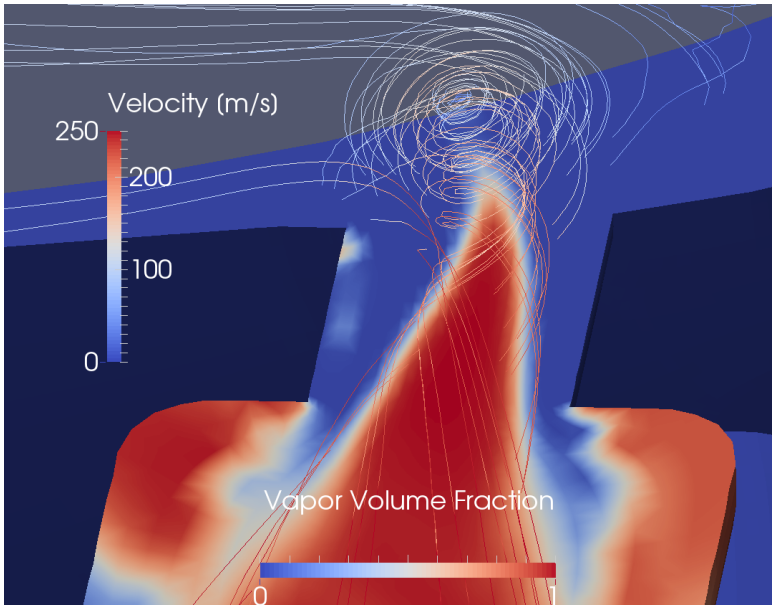

Figure 7.24: String flash boiling resulting from the swirling flow in the sac. Taken midway through flashing simulation. Streamlines are colored by velocity and the cut plane is colored by the vapor volume fraction.

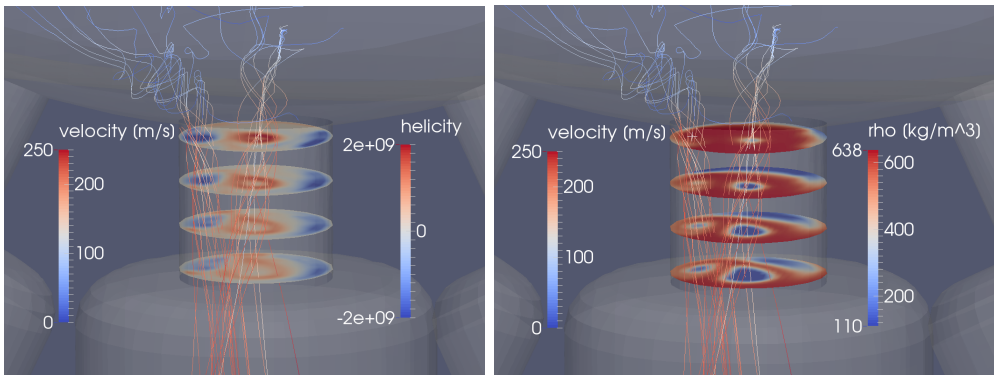

Figure 7.25: Two counter-rotating vortices being entrained into a single nozzle hole. Taken midway through non-flashing simulation. Streamlines are colored by velocity and the cut planes are colored by helicity on the left image and density on the right image.

As vortices are entrained into the nozzle holes, the simulation often predicts vapor generation at their core. A similar phenomena is commonly observed in other applications when strings of vapor are generated through cavitation. The vapor generation process here, however, is more appropriately described as flash-boiling because the fuel is hot and this is a thermal non-equilibrium process. String flash-boiling can be seen in Figs. 7.24 and 7.25 where a single vortex, or two counter-rotating vortices can result in a significant drop in flow density.

While string flash-boiling is similarly observed in both the spray G and spray G2 conditions, they behave differently in the near-field region. In the spray G2 condition, the lower back pressure allows for the vapor core to continue to expand in the near-field. In the spray G condition, the vapor collapses within and outside the counterbore and is displaced by non-condensable gas.

The swirling nature of the flow also has an influence on the vapor generated at the inlet corner. Observation of the successive density cut planes on the right image of Fig. 7.25, shows that the vapor generated at the inlet corner appears to be both compressed and transported by the swirling flow.

This complex internal nozzle flow results in perturbations and expansions of the spray angle. Fig. 7.26 shows the expansion of the spray angle caused by string flash-boiling. Here the nozzle hole on the left contains a large vortex and the hole on the right does not. Similar to a swirl atomizer, as the vortex exits the nozzle hole the angular momentum of the flow tears the jet apart. The counterbore walls then serve to geometrically restrict the expansion of the flow.

Finally, this complex internal nozzle flow also results in fluctuations in the mass flow rate. Mass flow rate and averaged density were calculated across a set of faces which perpendicularly cut through the middle of each of the 8 nozzle holes. These results are shown in Fig. 7.27. The oscillations in the average density are due to vapor generation at the inlet corner and vapor generation through string flash-boiling.

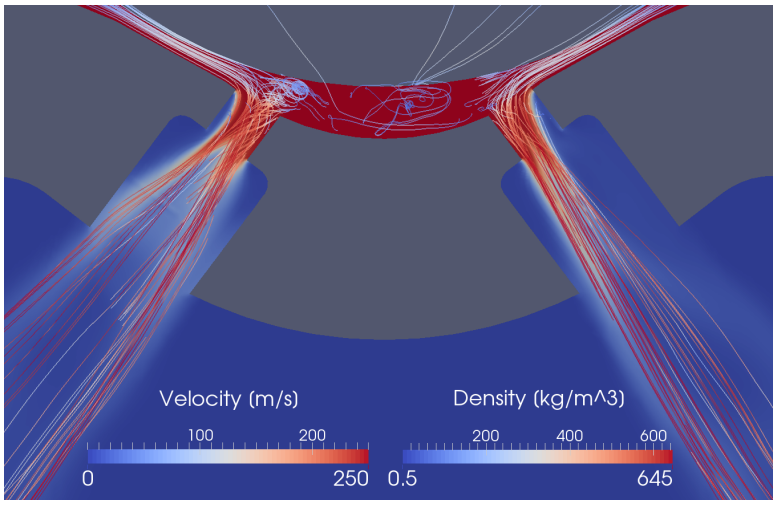

Figure 7.26: The expansion of the spray angle caused by string flash-boiling. Taken midway through flashing simulation. Streamlines are colored by velocity magnitude and the cut plane is colored by density.

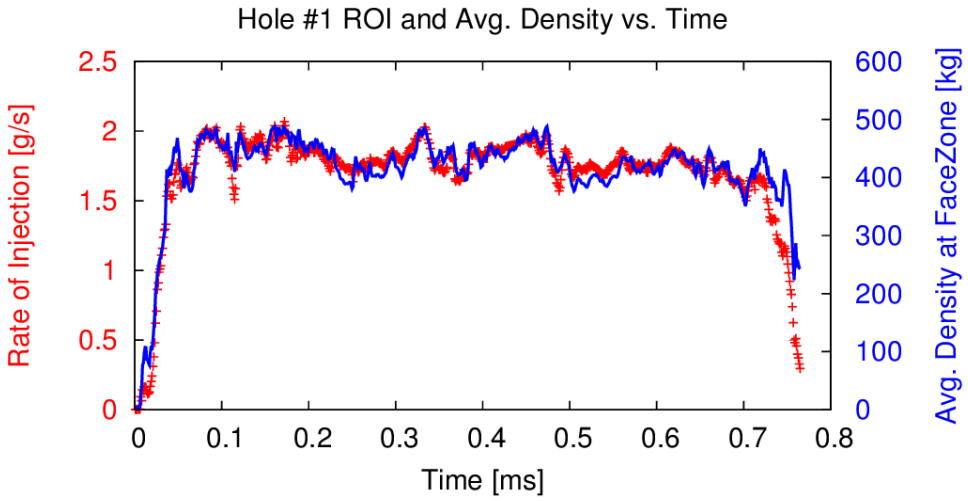

Figure 7.27: Rate of injection and average density across hole #1 cut plane.

These oscillations are clearly the dominating influence on fluctuations in the nozzle hole ROI and in the hole-to-hole variation in mass flow rate.

7.2.3 Summary

Spray G flashing and non-flashing injection has been simulated with transient needle motion. The primary results are summarized below:

- The results demonstrate the ability of CFD simulations to capture the rate of injection by prescribing the upstream pressure and lifting the needle with dynamic mesh motion.

- The results were qualitatively validated against experimental imaging, capturing spray angle expansion and perturbation due to the closing of the needle, predicting the presence or lack of ambient gas ingestion into the counterbore, and capturing the oscillation frequency in the spray plumes.

- At low lift conditions vapor generation is observed in the seat area as the fuel flows past the narrow region of the needle.

- Needle wobble is shown to have no measurable influence on the hole-to-hole variation in mass flow rate and spray structure. However, the needle to needle-guide clearance in these simulations may have been overestimated and the use of an ensemble averaged motion profile may have diminished the magnitude of the wobble. Further investigation may be justified as higher fidelity experimental characterization of the needle motion and needle-guide clearance becomes available.

- The complex flow contained within the fuel injector sac is analyzed and shown to contain transient interacting vortices which result in string flash-boiling, perturbations in spray angle and direction, and oscillations in mass flow rate.

- The oscillations in mass flow rate are ultimately attributed to the presence of vapor within the nozzle holes decreasing the average flow density.

7.3 Comparing counterbore flow behavior

It is interesting to note that the axisymmetric flash-boiling sprays from section 7.1 behaved very differently than the mild-flashing sprays from section 7.2. The difference in the flow dynamic is most noticeable when observing the initial spray expansion and with it the presence, or lack thereof, of ingestion of ambient gas into the counterbore. These flow patterns can be observed in Figs. 7.5 and 7.15. In both the mild- and hard-flashing axisymmetric cases that were subjected to a 20 MPa pressure drop, the spray did not come into contact with the counterbore. However, the mild-flashing spray G2 case, which also had a 20 MPa pressure drop, consistently demonstrated a uniform contact of the spray with the counterbore.

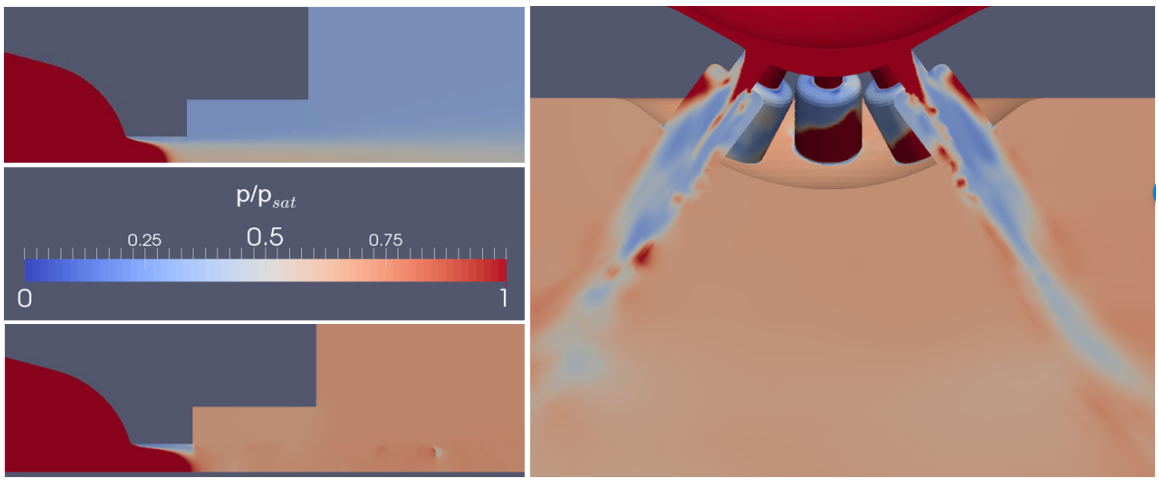

Figure 7.28: Local pressure to saturate pressure ratio for hard-flashing (top left) and mild-flashing (bottom left) axisymmetric simulations and mild-flashing spray G2 multi-hole simulation (right).

The difference in the flow fields is even more interesting when comparing the local to ambient pressure ratio within the counterbore and near-field region. This is shown Fig. 7.28. Note that the axisymmetric, mild-flashing simulation shown here is a new case with fuel, temperature, and pressure conditions that match the multi-hole spray G2 case. While all three flashing simulations demonstrate a similar pressure drop at the inlet corner, it is only in the multi-hole nozzle case that the pressure ratio

drops upon entering the counterbore. The axisymmetric cases both recover ambient pressure within the counterbore.

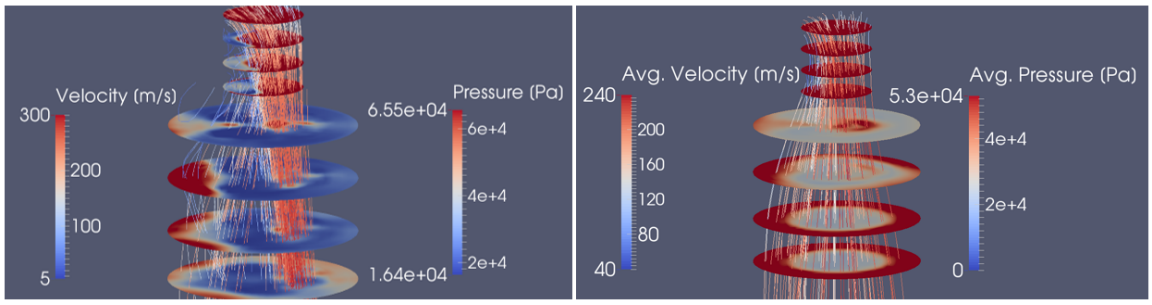

Figure 7.29: Cut-planes through one of the spray G2 nozzle holes, colored by pressure. Streamlines are colored by velocity. The left image is from 600 μs after SOI, the figure on the right is a time average from 200-600 μs.

This drop in pressure within the counterbore is likely the result multiple factors, one being the vorticity in the flow. Within the inner-hole of the nozzle, the area of the flow is constrained and the pressure on the edge of the flow can be high as it is supported by the surface of the hole. Upon entering the counterbore, these constraints are removed and the pressure within the jet decreases as the vorticity in the flow causes the spray to diverge. While the vorticity observed in this part of the simulation isn't strong enough to generate a string flash-boiling vortex in the inner-hole, it still is present; as described in section 7.2.2.6, the vortices in these simulations vary in their strength and duration, and it is common for multiple vortices to drain into the same hole. The divergence of the spray and the pressure response can be seen in Fig. 7.29. It is interesting to note that the jet would expand further if not for the counterbore walls. This, then, results in higher static pressures along the counterbore exit surface, further inhibiting the ingestion of ambient gas. The instantaneous flow field

The transient, asymmetric nature of the spray may also contribute to the low pressure ratio. While the instantaneous flow field may not contain sufficient vorticity

to drive such a dramatic pressure drop, the recovery of pressure takes time in a compressible flow. The transient nature of the jet will also help distribute momentum to the vapor which fills large volumes of the counterbore. This will further help prevent the ingestion of ambient gas.

The low pressure within the spray G2 jet could be recovered back to ambient pressure in two ways. First, there could be a negative divergence in the flow. This, however, cannot occur within the counterbore under these conditions because the momentum and area of the expanded jet do not allow for the ingestion of ambient gas. Second, the flash-boiling process could reach equilibrium, generating a greater volume of fuel vapor and bringing the local pressure to the saturated pressure. This, however, won't happen quickly because the flow timescales are smaller than the phase change timescales. This means that the recovery of the ambient pressure won't occur until the spray leaves the counterbore and is able to both mix with ambient gas and generate more vapor.

In contrast to this, the pressure is easily recovered in the axisymmetric cases. Here there is no vorticity in the flow and the only mechanisms driving the expansion of the jet are turbulent mixing and flash-boiling. These mechanisms, however, are not strong enough to expand the spray to the extent that it contacts the counterbore. This allows for the ingestion of ambient gas, which recovers the ambient pressure.

The pressure ratio response of the non-flashing spray G case is compared with the flashing spray G2 case in Fig. 7.30. The left nozzle hole of the spray G case is demonstrating a similar pressure drop behavior to what is observed in the spray G2 case. This pressure drop, however, is recovered to ambient about halfway down the counterbore. Here, it appears, that the relatively high ambient pressure (600 kPa) can quickly overcome the drop introduced at exit of the inner-hole. The ability to recover ambient pressure is aided here by the fact that there is significantly less volume occupied by vapor, allowing for easy ingestion of gas.

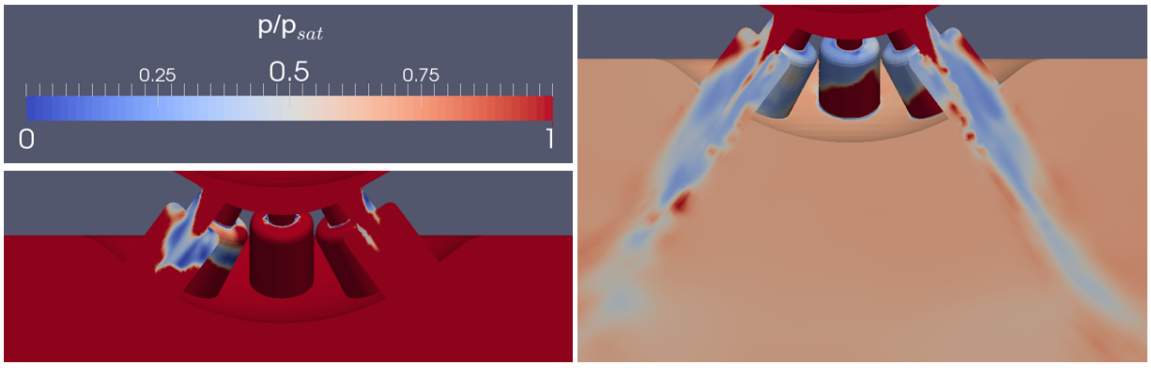

Figure 7.30: Local to saturated pressure ratio for the non-flashing spray G (left) and mild-flashing spray G2 (right) cases. Taken at 600 μs after SOI.

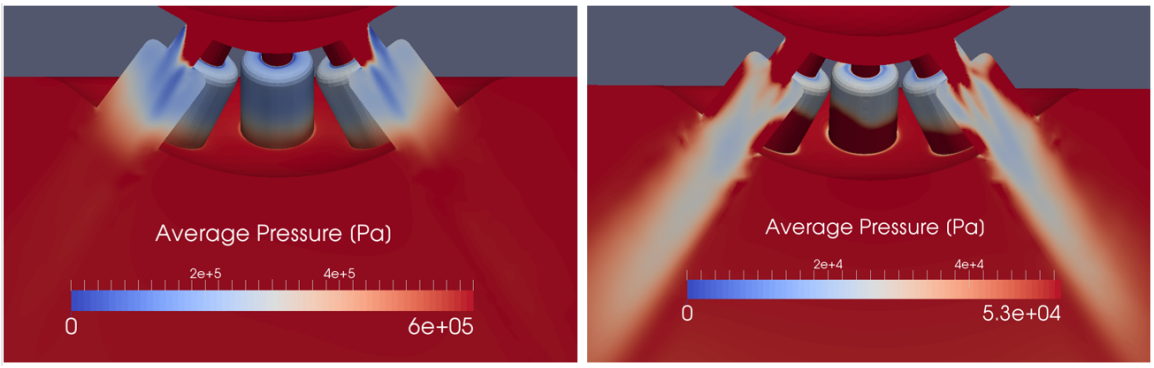

Figure 7.31: Time averaged pressure profiles of the non-flashing spray G (left) and mild-flashing spray G2 (right) cases. Taken from 200-600 μs after SOI.

Finally, in Fig. 7.31, the average pressure of the non-flashing spray G case is compared with the flashing spray G2 case. Here it can be seen that the ambient pressure isn't recovered in the flashing case until multiple counterbore diameters downstream. This further suggests that vorticity is driving the pressure drop, as the vorticity effects are expected to persists downstream.

7.4 Conclusions

While GDI sprays are typically much lower Reynolds number as compared with diesel DI, the added effect of flash-boiling significantly increases the complexity of

flow. Eulerian CFD modeling is a powerful tool for illuminating the complex flow dynamics behind these sprays. In this chapter, this has been demonstrated through a 2D axisymmetric parameter study as well as through 3D simulations on a complex multi-hole SVCO injector.

The parameter study investigated the influence of counterbore depth, pressure drop, and the P_a/P_s ratio. The significant effect of flash-boiling on spray angle at low P_a/P_s is shown. This effect is more pronounced in the near-field with the lower injection velocities associated with a smaller pressure drop. The counterbore is shown to have little effect on the axisymmetric spray, however fuel contact with the counterbore is predicted in the lowest velocity, hard-flashing case. Finally, the discharge coefficient of the nozzle is shown to be highly dependent on the Reynolds number as well as the flashing intensity.

The study conducted on the multi-hole SVCO injector consisted of a detailed analysis of internal nozzle and near-field flow in flashing and non-flashing conditions. Excellent agreement to experimental rate of injection (ROI) is achieved with transient needle motion and qualitative agreement to experimental imaging in the near-field is shown. Complex internal nozzle flow is analyzed and shown to result in string flash-boiling, perturbations and expansions of the spray angle, and oscillation in the ROI. The discovery and investigation of the complex internal flow in this micro-sac GDI injector is a novel and interesting result. The behavior of these sprays is absolutely dependent upon this internal flow and it can only be captured through 3D simulation with sufficient grid resolution within the sac region. The implications of these findings are significant as they explain the mechanism behind the perturbations and expansions of individual spray plumes.

Finally, the influence of the internal flow dynamics on flashing injection through a multi-hole SVCO nozzle is further highlighted by analyzing the pressure response within the counterbore and near-field spray and comparing it with that of the axisym-

metric simulations. For the multi-hole nozzle, the pressure within the counter-bore and near-field spray is significantly lower than the ambient pressure. For the axisymmetric simulations, the ambient pressure is recovered well within the counterbore. The difference in the behavior appears to be the result of the vorticity in the flow causing an expansion of the spray in the counterbore. Furthermore, the counterbore may play a role in delaying the recovery of the pressure by preventing the spray from mixing with ambient gas.

CHAPTER 8

SUMMARY AND CONCLUSIONS

8.1 Summary

The research presented in this dissertation was related to multiphase internal nozzle flow and external sprays. Beginning with a literature review of experimental studies, popular experimental techniques were described. While there are many experimental techniques which work well in the far-field region of an atomizing spray, the high optical density in the near-field spray and within the nozzle limit experimental characterization. Common experimental observations were discussed, showing that the nozzle geometry has significant impact on the spray characteristics, directly influencing the spray through factors such as turbulence level and internal vapor generation through cavitation. The influences of ambient conditions and flash-boiling were also discussed.

Next, common CFD approaches used to model multiphase internal nozzle flow and external sprays were covered. This included a description of high-fidelity sharp-interface approaches which attempt to model these flows based upon first principles. While these methods are extremely costly for high Reynolds and Weber number flows, they provide insight into the underlying physics behind the atomization process, and they can be used to validate engineering level CFD models. The widely used LE approach to spray modeling was then described, showing that spray characteristics can be well captured under many conditions. This approach, however, does not capture the influence of the internal flow, and therefore is inherently limited. Alternatively, solvers based on an Eulerian description of the multiphase flow can naturally couple

the internal flow with the external spray. An increase in the popularity of Eulerian based models was shown, with the diffuse interface single-field Eulerian approach demonstrating promise for predicting the influence of the internal nozzle flow on the external spray under highly atomizing conditions.

Developments and advancements applicable to these Eulerian solvers were then discussed. This included a new constraint on the turbulent mixing model, as well as the inclusion of the LHF vaporization model and the HRM non-equilibrium phase change model. Additionally, issues regarding thermodynamic and hydrodynamic consistency of compressible flows using a segregated solution approach were addressed, as were issues regarding dynamic mesh motion in a compressible solver. Finally, an efficient and effective way of accounting for high pressure thermodynamic properties was presented.

Applied case studies relating to diesel DI were then described in detail. The single-field Eulerian approach used here performed well, capturing spray characteristics such as the near-field and far-field density distributions, spray penetration, and velocity profiles with a moderate level of accuracy. In converging, axisymmetric diesel DI nozzles, modeling of the internal flow was shown to only marginally benefit the solution. Simulations including transient needle motion then demonstrated the influence of the needle on the rate of injection and on the localized internal fuel temperature. Transient needle motion was shown to result in a Coanda effect in the flow field around the needle and nozzle walls, however this flow field had little influence on the external spray.

Finally, applied case studies related to gasoline direct injection (GDI) were presented, including a 2D parameter study and a detailed analysis of internal and near-field flow through an SVCO nozzle. In the parameter study, counterbore depth, pressure drop, and the P_a/P_s ratio were varied. The significant influence of flash-boiling under a low P_a/P_s was shown. The simulations of flow through a multihole

SVCO nozzle produced excellent agreement to experimental rate of injection (ROI), with the injection event actuated with transient needle motion. Furthermore, excellent qualitative agreement to experimental imaging in the near-field was achieved. Complex internal nozzle flow was analyzed and shown to result in string flash-boiling, perturbations and expansions of the spray angle, and oscillation in the ROI.

8.2 Conclusions

The single-field multiphase Eulerian approach to internal nozzle flow and external spray modeling is a useful tool for both understanding and designing DI atomizers. Where experimental observations fall short in characterizing these regions, Eulerian models are well suited to provide high-fidelity insight into the behavior of the flow. This insight is of particular value in cavitating nozzles and in multihole nozzles where the complex internal flow can have a strong influence on the external spray.

The tools developed and described in this dissertation have allowed and and will continue to allow for insights to be drawn. Simulations with transient needle motion on GDI and diesel DI sprays can now be investigated in parallel with a compressible pressure equation. The turbulent mixing model is now significantly more stable with the addition of a realizability constraint. Accurate fuel temperatures can now be predicted across very large pressure drops with the extension of the fluid property class. Furthermore, the influence of non-equilibrium phase change can be modeled with HRM for the internal nozzle flow as well as the external spray.

Under high Reynolds and Weber numbers it has been shown that interfacial effects do not influence the large scale characteristics of the spray. Under these conditions, a diffuse interface approach is justified and it is recommended that the problem be treated as one of turbulent mixing. To do this, the $\Sigma - Y$ approach is very well suited, especially under the high ambient density conditions present in diesel engines. The use of high performance computing and the extremely scalable IMEX-RK3 imple-

mentation of $\Sigma - Y$ provides the ability to quickly produce a high-fidelity solution. Under more moderate Reynolds and Weber numbers, Eulerian models can still provide insight into the influence of the nozzle flow on the spray, however a transition of Lagrangian framework is recommended in the far-field.

The internal flow dynamics of axisymmetric, converging diesel nozzles do not have a large influence on the external spray. This is because the flow through the converging nozzle has a favorable pressure gradient which results in a relatively uniform exit profile. For injection through these types of nozzles, 2D external-only simulations appear to be sufficient. Capturing the influence of nozzle asymmetries and surface roughness and features would, however, require a high-fidelity 3D simulation.

The mean temperature change of fuel flowing through a DI nozzle is relatively small and can be predicted through a simple thermodynamic analysis using an accurate equation of state and the nozzle velocity coefficient to estimate the efficiency of the process. A higher C_v will result in a cooler mean flow, and for n-dodecane, C_v values above 0.9 may even experience a slight temperature drop. The typical temperature profile has a very thin, slowly moving warm region near the wall, and a large, quickly moving cool region in center of the nozzle hole. The overall influence of the temperature change on the spray is, therefore, expected to be minimal. At low needle lift, very warm localized fuel is observed in the needle seat region. The quantity of warm fuel, however, is small relative to the sac volume. This is because the time spent at low lift is very short and the flow rates experienced here are low. This localized warm fuel in the sac may dictate if and where vapor forms with the pressure drop that occurs upon needle closure.

The complex internal flow dynamics discovered in the study on GDI injection through the ECN spray G SVCO injector are very interesting. The large levels of vorticity inside the sac contribute to a highly transient injection process. The vorticity can be so strong, that it temporarily creates hollow-cone sprays in the injector. The

occurrence of these vortices is likely a consequence of the adverse pressure gradient as the flow enters the sac. The resulting perturbations in the spray are a likely contributor to tip-wetting, where there is a post-injection fuel residue on the nozzle surface. This is undesirable as over time it can lead to carbon build-up and nozzle fouling. Understanding the mechanism behind these perturbations might allow for them to be controlled in the next generation of GDI nozzles, resulting in more predictable, cleaner sprays.

8.3 Future Work

There is room for further evaluation and validation of the complex internal flow structures observed in the ECN spray G simulations. This could include a higher-fidelity simulation with an LES model. Validation through analysis of near-field plume angle fluctuation frequencies might be possible, as could validation through particle imaging velocimetry on transparent injectors of a similar geometry.

Although the internal flow features of the spray D injector had no influence on the external spray, it would be interesting to conduct a similar study on the nozzle's sharp inlet corner twin, the ECN Spray C nozzle. This nozzle has a very similar internal geometry and is, therefore, likely to demonstrate the same Coanda effect within the sac. As these interesting internal flow features encounter the cavitating sharp inlet corner, it is likely that an interesting effect will be observed.

In their current state, these Eulerian models are very powerful design tools and there is a lot of interesting work which could be done. In an effort to reduce tip-wetting, HRMFoam could be used to investigate various stepped hole shapes on a multihole GDI nozzle. It would also be interesting to try to design a multihole GDI injector which produces stable, non-fluctuating sprays. The influence of surface roughness related to manufacturing techniques could be further investigated. If

surface roughness is of benefit to flashing sprays, then HRMFoam could be used to quantify the ideal roughness size.

Finally, these models would benefit significantly from the ability to capture the influence of needle closure on the flow. A lot happens at the instant of closure. First, the sac pressure plummets as the momentum in the nozzle pulls against the sealed needle seat. This low pressure then results in vapor generation, or expansion of vapor which is already present. Next, upon vapor collapse, ambient air is then ingested into the nozzle. Modeling all of this would also require transitioning out of the diffuse interface approach and into a VOF approach. Both of these improvements may be effort well spent as the very-early and very-late moments of the injection are likely big contributors to engine emission. Once the needle closes and just after it opens, the flow velocities drop and with them the Reynolds and Weber numbers, resulting in large non-atomized fuel ligaments entering the combustion chamber.

BIBLIOGRAPHY

[1] Engine Combustion Network. *http://www.sandia.gov/ecn/index.php*.

[2] Aleiferis, P. G., and Van Romunde, Z. R. An analysis of spray development with iso-octane, n-pentane, gasoline, ethanol and n-butanol from a multi-hole injector under hot fuel conditions. *Fuel 105* (2013), 143–168.

[3] Amsden, A. A., O'Rourke, P. J., and Butler, T.D. KIVA-II a computer program for chemically reactive flows with sprays. *LA-11560-MS* (1989).

[4] Aori, Gele, Hung, David L. S., Zhang, Ming, Zhang, Gaomimg, and Li, Tianyun. Effect of nozzle configuration on macroscopic spray characteristics of multi-hole fuel injectors under superheated conditions. *Atomization and Sprays 26*, 5 (2016), 439–462.

[5] Ashely, S. Diesel cars come clean. *Mechanical Engineering 119*, 8 (1997), 52–57.

[6] Balewski, Benjamin, Heine, Barbara, and Tropea, Cameron. Experimental investigation of the correlation between nozzle flow and spray using laser doppler velocimeter, phase doppler system, high-speed photography, and radiography. *Atomization and Sprays 20*, September 2008 (2010), 57–70.

[7] Battistoni, M., Grimaldi, C., and Marianim, F. Coupled simulation of nozzle flow and spray formation using diesel and biodiesel for CI engine applications. *SAE International 2012-01-1267*.

[8] Battistoni, Michele, Duke, Daniel J, Swantek, Andrew B, Tilocco, F Zak, Powell, Christopher F, and Som, Sibendu. Effects of noncondensable gas on cavitating nozzles. *Atomization and Sprays 25*, 6 (2015), 453–483.

[9] Battistoni, Michele, Xue, Qingluan, Som, Sibendu, and Pomraning, Eric. Effect of off-axis needle motion on internal nozzle and near exit flow in a multi-hole diesel injector. *SAE Int. J. Fuels Lubr. 7*, 1 (2014), 167–181.

[10] Beau, P, Funk, M, Lebas, R, and Demoulin, F. Applying quasi-multiphase model to simulate atomization processes in diesel engines : modeling of the slip velocity. In *SAE 2005 World Congress & Exhibition* (2005).

[11] Beau, Pierre-Arnaud. *Modélisation de l'atomisation d'un jet liquide Application aux sprays Diesel*. PhD thesis, Université de Rouen, 2006.

[12] Beau, Pierre-Arnaud, Menard, T., and Lebas, R. Numerical jet atomization. part II: modeling information and comparison with DNS results. In *ASME Joint U.S. - European Fluids Engineering Summer Meeting* (2006).

[13] Befrui, B, Corbinelli, G, Hoffmann, G, Technical, Delphi, and Gillingham, Centre. Cavitation and hydraulic Flip in the outward-opening GDI Injector Valve-Group.

[14] Befrui, Bizhan, Corbinelli, Giovanni, Spiekermann, Peter, Shost, Mark, and Lai, Ming-Chia. Large eddy simulation of GDI single-hole flow and near-field spray. *SAE Int. J. Fuels Lubr. 5*, 2 (2012), 620–636.

[15] Beheshti, Novid, Burluka, Alexey a., and Fairweather, Michael. Assessment of ΣY liq model predictions for air-assisted atomization. *Theoretical and Computational Fluid Dynamics 21*, 5 (June 2007), 381–397.

[16] Belhadef, A., Vallet, A., Amielh, M., and Anselmet, F. Pressure-swirl atomization: modeling and experimental approaches. *International Journal of Multiphase Flow 39* (Mar. 2012), 13–20.

[17] Benajes, J., Pastor, J. V., Payri, R., and Plazas, a. H. Analysis of the influence of diesel nozzle geometry in the injection rate characteristic. *Journal of Fluids Engineering 126*, 1 (2004), 63.

[18] Berndorfer, Axel, Breuer, Stephan, Poick, Walter, and Von Bacho, Paul. Diffusion combustion phenomena in GDI engines caused by injection process. Tech. Rep. 2013-01-0261, SAE, 2013.

[19] Bianchi, GM, Minelli, F, Scardovelli, R, and Zaleski, S. 3D large scale simulation of the high-speed liquid jet atomization. *SAE Tech. Pap. 2007-01-0244* (2007).

[20] Bilicki, Z., and Kestin, J. Physical aspects of the relaxation model in two-phase flow. In *Proceedings of the Royal Society A: Mathematical, Physical and Engineering Sciences* (1990), vol. 428, pp. 379–397.

[21] Blessing, M., Konig, G., Kruger, C., Michels, U., and Schwarz, V. Analysis of flow and cavitation phenomena in diesel injection Nozzles and Its Effects on Spray and Mixture Formation. In *SAE 2003 World Congress & Exhibition* (2003).

[22] Blessinger, Matthew, Manin, Julien, Skeen, Scott A., Meijer, Maarten, Parrish, Scott, and Pickett, Lyle M. Quantitative mixing measurements and stochastic variability of a vaporizing gasoline direct-injection spray. *International Journal of Engine Research 16*, 2 (2015), 238–252.

[23] Blokkeel, G., and Borghi, R. A 3D Eulerian model to improve the primary breakup of atomizing jet. In *SAE Technical Paper* (2003).

[24] Blokkeel, G., Demoulin, F.X., and Borghi, R. Modeling of two-phase flows: an Eulerian model for diesel injection. In *Thermo- and Fluid Dynamic Process in Diesel Engines 2*. 2004, pp. 87–105.

[25] Caudwell, D R, Trusler, J P M, Vesovic, V, and Wakeham, W A. The viscosity and density of n-dodecane and n-octadecane at pressures up to 200 MPa and temperatures up to 473 K. *International Journal of Thermophysics 25*, 5 (2004), 1339–1352.

[26] Charalampous, G., Hadjiyiannis, C., Hardalupas, Y., and Taylor, A. Measurement of continuous liquid jet length in atomizers with optical connectivity, electrical conductivity and high-speed photography techniques. In *ILASS* (2010).

[27] Charalampous, G., Hardalupas, Y., and Taylor, A. Novel techniques for measurement of the continuous liquid jet core in an atomizer. *AIAA Journal 47*, 11 (2009), 2605–15.

[28] Chaves, H, and Ludwig, Ch. Characterization of cavitation in transparent nozzles depending on the nozzle geometry. In *ILASS-2005* (Nottingham, 2005).

[29] Chaves, Humberto, and Schuhbauer, Ingo. Cavitation in an asymmetric transparent real size VCO nozzle. In *Spray06, Workshop über Sprays* (Lampoldshausen, Germany, 2006).

[30] Chenadec, Vincent Le, and Pitsch, Heinz. A conservative framework for primary atomization computation and application to the study of nozzle and density ratio effects. *Atomization and Sprays 23*, 12 (2013), 1139–1165.

[31] Colarossi, Michael, Trask, Nathaniel, Schmidt, David P., and Bergander, Mark J. Multidimensional modeling of condensing two-phase ejector flow. *International Journal of Refrigeration 35*, 2 (Mar. 2012), 290–299.

[32] Dahms, Rainer N., Manin, Julien, Pickett, Lyle M., and Oefelein, Joseph C. Understanding high-pressure gas-liquid interface phenomena in diesel engines. *Proceedings of the Combustion Institute 34*, 1 (Jan. 2013), 1667–1675.

[33] Dahms, Rainer N., and Oefelein, Joseph C. On the transition between two-phase and single-phase interface dynamics in multicomponent fluids at supercritical pressures. *Physics of Fluids 25* (2013).

[34] Demoulin, Francois-Xavier, Reveillon, Julien, Duret, B., Bouali, Zakaria, Desjonqueres, P., and Menard, Thibaut. Toward using direct numerical simulation to improve primary break-up modeling. *Atomization and Sprays 23*, 11 (2013), 957–980.

[35] Demoulin, F.X., Beau, Pierre-Arnaud, Blokkeel, G., Mura, A., and Borghi, R. A new model for turbulent flows with large density fluctuations: application to liquid atomization. *Atomization and Sprays 17* (2007), 315–345.

[36] Desantes, J. M., Garcia-Oliver, J. M., Pastor, J. M., Pandal, A., Baldwin, E., and Schmidt, D. P. Coupled/decoupled spray simulation comparison of the ECN spray A condition with the $\Sigma - Y$ Eulerian atomization model. *International Journal of Multiphase Flow 80* (2016), 89–99.

[37] Desantes, J M, Payri, R, Salvador, F J, and Gimeno, J. Measurements of spray momentum for the study of cavitation in diesel injection nozzles. *SAE Technical Paper 2003-01-0703* (2003).

[38] Desantes, José M. Jose M., Hoyas, Sergio, Gil, Antonio, Khuong-Anh, Dung, Ravet, Frédéric Frederic, and Dung, Khuong Anh. A recent EulerianLagrangian CFD methodology for modeling direct injection diesel sprays. *International Journal of Computational Methods 11*, 3 (Sept. 2013), 1343012.

[39] Desantes, José María, Payri, Raúl, Gimeno, Jaime, and Marti-Aldaravi, Pedro. Simulation of the first millimeters of the diesel spray by an Eulerian spray atomization model applied on ECN spray A injector. *SAE Technical Paper* (2014).

[40] Desjardin, O, Moureau, V, Knudsen, E, Herrmann, M, and Pitsch, H. Conservative level set/ghost fluid method for simulating primary atomization. *Proc. Annu. Conf. Inst. Liq. Atom. Spray Syst. Am., 20th. ILASS Am., Pap. 34. Toronto: Inst. Liq. Atom. Spray Syst.* (2007).

[41] Desjardins, Olivier, Moureau, Vincent, and Pitsch, Heinz. An accurate conservative level set/ghost fluid method for simulating turbulent atomization. *Journal of Computational Physics 227*, 18 (Sept. 2008), 8395–8416.

[42] Desjardins, Olivier, and Pitsch, H. Detailed numerical investigation of turbulent atomization of liquid jets. *Atomization and Sprays 20*, 4 (2010), 311–336.

[43] Desjardins, Olivier, and Pitsch, Heinz. A spectrally refined interface approach for simulating multiphase flows. *Journal of Computational Physics 228*, 5 (Mar. 2009), 1658–1677.

[44] Desportes, A, Zellat, M, Desoutter, G, Abouri, D, Liang, Y, Raven, F., CD-adapco, and Renault. Validation and application of the Eulerian-Lagrangian spray atomization (ELSA) model for the diesel injection simulation. In *International Multidimensional Engine Users Meeting at the SAE Congress* (DETOIT, MI, 2010), pp. 1–10.

[45] Downar-Zapolski, P., Bilicki, Z., Bolle, L., and Franco, J. the non-equilibrium relaxation model for one-dimensional flashing liquid flow. *International Journal of Multiphase Flow 22*, 3 (1996), 473–483.

[46] Drew, D. A. Mathematical modeling of two-phase flows. *Annual Review of Fluid Mechanics 15* (1983), 261–291.

[47] Duke, Daniel J., Swantek, Andrew, Tilocco, Zak, Kastengren, Alan L., Fezzaa, Kamel, Neroorkar, Kshitij, Moulai, Maryam, Powell, Christopher, and Schmidt, David P. X-ray imaging of cavitation in diesel injectors. In *SAE 2014 World Congress & Exhibition* (Apr. 2014).

[48] Duke, D.J., Kastengren, A. L., Tilocco, F. Zak, and Powell, C.F. Synchrotron X-ray measurements of cavitation. In *ILASS-Americas 25th Annual Conference on Liquid Atomization and Spray Systems* (Pittsburgh, PA, 2013), no. May.

[49] Duke, D.J., Swantek, A.B., Tilocco, Z., Kastengren, A.L., Fezzaa, K., Neroorkar, K., Moulai, M., Powell, C.F., and Schmidt, D.P. X-ray imaging of cavitation in diesel injectors. *SAE Int. J. Engines 7*, 2 (2014), 1003–1016.

[50] Dukowicz, John. A particle-fluid numerical model for liquid sprays. *Journal of Computational Physics 35*, 2 (1980), 229–253.

[51] Dumouchel, Christophe. On the experimental investigation on primary atomization of liquid streams. *Experiments in Fluids 45*, 3 (June 2008), 371–422.

[52] Elgobashi, S. On predicting particle-laden turbulent flows. *Appl. Sci. Res. 52* (1994), 309–29.

[53] Faeth, G.M. Evaporation and combustion of sprays. *Progress in Energy and Combustion Science 9*, 1-2 (1983), 1–76.

[54] Faeth, G.M, Hsiang, L.-P, and Wu, P.-K. Structure and breakup properties of sprays. *International Journal of Multiphase Flow 21* (Dec. 1995), 99–127.

[55] Falgout, Z., Rahm, M., Wang, Z., and Linne, M. Ballistic imaging in the spray formation region for the ECN spray A. In *ILASS* (2013).

[56] FAME. Spray and Combustion Analysis. *http://www.fame-project.de/content/overview* (2014).

[57] Fath, A., Fettes, C., and Leipertz, A. Investigation of the diesel spray break-up close to the nozzle at different injection conditions. In *The Fourth International Symposium COMODIA 98* (1998), pp. 429–434.

[58] Fedkiw, Ronald P, Aslam, Tariq, Merriman, Barry, and Osher, Stanley. A non-oscillatory Eulerian approach to interfaces in multimaterial flows (the ghost fluid method). *Journal of Computational Physics 152*, 2 (July 1999), 457–492.

[59] Février, Pierre, Simonin, Olivier, and Squires, Kyle D. Partitioning of particle velocities in gassolid turbulent flows into a continuous field and a spatially uncorrelated random distribution: theoretical formalism and numerical study. *Journal of Fluid Mechanics 533* (June 2005), 1–46.

[60] Fox, R.O. A quadrature-based third-order moment method for dilute gas-particle flow. *Journal of Computational Physics 227*, 12 (2008), 6313–6350.

[61] Fox, R.O. Higher-order quadrature-based moment methods for kinetic equations. *Journal of Computational Physics 228*, 20 (2009), 7771–7791.

[62] Fox, R.O., Laurent, F., and Massot, M. Numerical simulation of spray coalescence in an Eulerian framework: direct quadrature method of moments and multi-fluid method. *Journal of Computational Physics 227*, 6 (2008), 3058–3088.

[63] Galland, PA, Liang, X., Wang, L., Breiasacher, K., L, L., Ho, P., and Al., Et. Time-resolved optical imaging of jet sprays and droplets in highly scattering medium. In *ASME Heat Transfer and Fluids Engineering Divisions* (1995).

[64] Garcia-Oliver, Jose M, Pastor, Jose M., Pandal, A., Trask, N., Baldwin, E., and Schmidt, David P. Diesel spray cfd simulations based on the $\Sigma - Y$ Eulerian atomization model. *Atomization and Sprays 23*, 1 (2013), 71–95.

[65] Gorokhovski, Mikhael, and Herrmann, Marcus. Modeling primary atomization. *The Annual Review of Fluid Mechanics* (2008).

[66] Grosshans, H., Berrocal, E., Kristensson, E., Szasz, R-C, and Fuchs, L. Correlating results from numerical simulation to SLIPI-based measurements for non-combusting diesel spray. In *ICLASS 2012, 12th Triennial International Conference on Liquid Atomization and Spray Systems* (2012).

[67] Gueyffier, D., Li, J., Nadim, A., Scardovelli, S., and Zaleski, S. Volume of fluid interface tracking with smoothed surface stress methods for three-dimensional flows. *Journal of Computational Physics 152* (1999), 423–56.

[68] Halls, B R, Radke, C D, Heindel, T J, Lohry, W F, Zhang, S, Meyer, T R, Lightfoot, M D, Danczyk, S A, Schumaker, S A, Force, Air, Directorate, Aerospace Systems, Roy, S, Energies, Spectral, Gord, J R, Kastengren, Alan L., Division, X-ray Science, and Engineer, Aerospace. Characterization of three-dimensional dense spray visualization techniques. In *AIAA Aerospace Sciences Meeting including the New Horizons Forum and Aerospace Exposition* (2013).

[69] Han, J., Lu, P., Xie, X., Lai, M., and Henein, N. Investigation of diesel spray primary breakup and development for different nozzle geometries. In *SAE Powertrain & Fluid Systems Conference & Exhibition* (2002).

[70] Hasse, C, and Peters, N. Eulerian spray modeling of diesel injection in a high-pressure / high temperature chamber. In *International Multidimensional Engine Modeling Users Group Meeting* (2001).

[71] Heilig, A, Kaiser, M, and Dinkelacker, F. Near nozzle high-speed measurements of the intact core for diesel spray. In *ICLASS 2012, 12th Triennial International Conference on Liquid Atomization and Spray Systems* (Heidelberg, Germany, 2012), pp. 1–8.

[72] Herrmann, M. A balanced force refined level set grid method for two-phase flows on unstructured flow solver grids. *Journal of Computational Physics 227*, 4 (Feb. 2008), 2674–2706.

[73] Hoehn, F. W., Rupe, J., and Sutter, J. Liquid-phase mixing of bipropellant doublets. Tech. rep., Jet Propulsion Labratory, Pasadena, California, 1972.

[74] Hoyas, Sergio, Gil, Antonio, Margot, Xandra, Khuong-Anh, Dung, and Ravet, Frederic. Evaluation of the EulerianLagrangian spray atomization (ELSA) model in spray simulations: 2D cases. *Mathematical and Computer Modeling 57*, 7-8 (Apr. 2013), 1686–1693.

[75] Hoyas, Sergio, Pastor, Jose M., Khuong-Anh, Dung, Mompo-Laborda, Juan Manuel, and CMT, Universidad Politecnica de Valencia. Application and evaluation of the Eulerian-Lagrangian spray atomization (ELSA) model on CFD diesel spray simulations. *SAE Technical Paper* (2011).

[76] Huang, Y. *Experimental Studies of Impulsively-Started Liquid-into-Gas and Gas-into-Gas Turbulent Jets*. Ph.d., Princeton, 2000.

[77] Idlahcen, S., Roze, C., Mees, L., Girosole, T., and Blaisot, J-B. Sub-picosecond ballistic imaging of a liquid jet. *Experiments in Fluids 52* (2010), 289–298.

[78] Islam, M. *Numerical and Experimental Investigations of High-Pressure Diesel Sprays*. Ph.d., Imperial College University of London, 2002.

[79] Iyer, Venkatraman, and Abraham, John. An evaluation of a two-fluid Eulerian-liquid Eulerian-gas model for diesel sprays. *Journal of Fluids Engineering 125*, 4 (2003), 660.

[80] Iyer, Venkatraman, and Abraham, John. Two-fluid modeling of spray penetration and dispersion under diesel engine conditions. *Atomization and Sprays 15*, 3 (2005), 249–270.

[81] Jasak, Hrvoje. *Error analysis and estimation for the finite volume method with applications to fluid flows*. Phd, University of London Imperial College of Science, Technology and Medicine, 1996.

[82] Johnson, K. S. Ford to Sell Improved EcoBoost Engine. *http://abcnews.go.com/Business/story?id=8139624* (2009).

[83] Kah, Damien, Laurent, Frédérique, Fréret, Lucie, Chaisemartin, Stéphane, Fox, Rodney O., Reveillon, Julien, and Massot, Marc. Eulerian quadrature-based moment models for dilute polydisperse evaporating sprays. *Flow, Turbulence and Combustion 85* (2010), 649–676.

[84] Karimi, Kourosh. *Characterisation of multiple-injection diesel sprays at elevated pressures and temperatures*. Phd, University of Brighton, 2007.

[85] Kastengren, A.L., Powell, C., Tilocco, F., Liu, Z., Moon, S., Zhang, X., and Gao, J. Correlation of split-injection needle lift and spray structure. *SAE Journal* (2011), 2011–01–0383.

[86] Kastengren, A.L., Powell, C.F., Liu, Z., and Wang, J. Time resolved, three-dimensional mass distribution of diesel sprays measured with x-ray radiography. In *The 2009 SAE World Congress* (Detroit, MI, 2009), pp. SAE Paper no. 2009–01–0840.

[87] Kastengren, Alan L., Powell, Christopher F., Liu, Zunping, Moon, Seoksu, Gao, Jian, Zhang, Xusheng, and Wang, Jin. Axial development of diesel sprays at varying ambient density. In *ILASS-Americas 22nd Annual Conference on Liquid Atomization and Spray Systems* (Cincinnati, OH, 2010), no. May.

[88] Kastengren, Alan L., Powell, Christopher F., Wang, Yujie, Im, Kyoung-Su, and Wang, Jin. X-ray radiography measurements of diesel spray structure at engine-like ambient density. *Atomization and Sprays 19*, 11 (2009), 1031–1044.

[89] Kastengren, Alan L., Tilocco, F. Zak, Duke, Daniel J., Powell, Christopher F., Zhang, Xusheng, and Moon, Seoksu. Time-resolved X-ray radiography of sprays from engine combustion network spray A diesel injectors. *Atomization and Sprays 24*, 3 (2014), 251–272.

[90] Kastengren, Alan L., Tilocco, F Zak, Powell, Christopher F, Manin, Julien, Pickett, Lyle M, Payri, Raúl, Bazyn, Tim, Termicos, C M T Motores, and Valencia, Universitat Politecnica De. Engine combustion network (ECN): measurements of nozzle geometry and hydraulic behavior. *Atomization and Sprays 22*, 12 (2012), 1011–1052.

[91] Kim, D, Desjardins, O, Herrmann, M, and Moin, P. The primary breakup of a round liquid jet by a coaxial flow of gas. *Proc. Annu. Conf. Inst. Liq. Atom. Spray Syst. Am., 20th, ILASS Am., Pap. 8. Toronto: Inst. Liq. Atom. Spray Syst* (2007).

[92] Kitchen, Tony. A Technical Overview of Common Rail Diesel Fuel Systems. *http://www.yildiz.edu.tr/˜sandalci/dersnotu/AKTraining.pdf*.

[93] Kralj, C. *Numerical Simulation of Diesel Spray*. Ph.d., Imperial College, University of London, 1993.

[94] Kristensson, E. *Structured Laser Illumination Planar Imaging (SLIPI); Applications for Spray Diagnostics*. Ph.d., Lund University, 2012.

[95] Lagumbay, Randy S. *Modeling and Simulation of Multiphase / Multicomponent Flows*. Ph.d., University of Colorado, 2006.

[96] Lai, M-C, Zheng, Y., Shost, M., Xie, X., Matsumoto, A., Wang, J., and Al., Et. Characterization of internal flow and spray of multihole DI gasoline spray using X-ray imaging and CFD. *SAE Technical Paper 2011-01-1881* (2011).

[97] Lai, M-C, Zheng, Y., Xie, X-B, Moon, S., Liu, Z., Gao, J., and Al., Et. Characterization of the near field spray and internal flow of single-hole and multi-hole sac nozzles using phase contrast X-ray imaging and CFD. *SAE Technical Paper 2011-01-0681* (2011).

[98] Lebas, R., Blokkeel, G., Beau, Pierre-Arnaud, and Demoulin, F.X. Coupling vaporization model with the Eulerian-Lagrangian spray atomization (ELSA) model in diesel engine conditions. *SAE Technical Paper 2005*, 724 (2005).

[99] Lebas, R., Menard, T., Beau, Pierre-Arnaud, Berlemont, A., and Demoulin, F.X. Numerical simulation of primary break-up and atomization: DNS and modelling study. *International Journal of Multiphase Flow 35*, 3 (Mar. 2009), 247–260.

[100] Lee, J., Madabhushi, R., Fotache, C., Gopalakrishnan, S., and Schmidt, David P. Flashing flow of superheated jet fuel. *Proceedings of the Combustion Institute 32*, 2 (2009), 3215–3222.

[101] Leick, P, Kastengren, A L, Liu, Z, Wang, J, and Powell, C F. X-ray measurements of mass distributions in the near-nozzle region of sprays from standard multi-hole common-rail diesel injection systems. In *ICLASS 2009, 11th Triennial International Conference on Liquid Atomization and Spray Systems* (Vail, Colorado, 2009), no. July.

[102] Lemmon, Eric W, and Huber, Marcia L. Thermodynamic properties of n-dodecane. *Energy and Fuels 18* (2004), 960–967.

[103] Lemmon, E.W., Huber, M.L., and McLinden, M.O. NIST standard reference database 23: reference fluid thermodynamic and transport properties-REFPROP, Version 9.1, *National Institute of Standards and Technology, Standard Reference Data Program*, Gaithersburg, 2013.

[104] Leroux, S., Dumouchel, C., and Ledoux, M. The stability curve of newtonian liquid jets. *Atomization and Sprays*, 6 (1996), 623–647.

[105] Linne, M., Paciaroni, M., Gord, J., and Meyer, T. Ballistic imaging of the liquid core for a steady jet in crossflow. *Applied Optics 44*, 31 (2005), 6627–34.

[106] Linne, M., Rahm, M., Falgout, Z., Wang, Z., Paciaroni, M., Matlok, S., and Al., Et. Correlation of internal flow and spray breakup for a fuel injector used in ship engines. In *The 8th US National Combustion Meeting* (2013).

[107] Linne, M., Sedarsky, D., Meyer, T., Gord, J., and Carter, C. Ballistic imaging of the flow in the interior of the near-field of an effervescent spray. *Experiments in Fluids 49*, 4 (2010), 911–23.

[108] Linne, Mark. Analysis of X-ray phase contrast imaging in atomizing sprays. *Experiments in Fluids 52*, 5 (Dec. 2011), 1201–1218.

[109] Linne, Mark. Imaging in the optically dense regions of a spray: A review of developing techniques. *Progress in Energy and Combustion Science 39*, 5 (Oct. 2013), 403–440.

[110] Linne, Mark, Paciaroni, Megan, Hall, Tyler, and Parker, Terry. Ballistic imaging of the near field in a diesel spray. *Experiments in Fluids*, 40, 6 (Feb. 2006), 836–846.

[111] Liu, Z., Im, K-S, Wang, Y, Fezzaa, K., Xie, X-B, Lai, M-C, and Al., Et. Near-nozzle structure of diesel sprays affected by internal geometry of injector nozzle: visualized by single-shot X-ray imaging. *SAE Technical Paper 2010-01-0877* (2010).

[112] Lückert, P., Waltner, A., Rau, E., Vent, G., and Schaupp, U. The new V6 gasoline engine with direct injection by Mercedes Benz. *MTZ 11* (2006), 67.

[113] Macian, V., Bermudez, V., Payri, R., and Gimeno, J. New technique for determination of internal geometry of a diesel nozzle with the use of silicone methodology. *Experimental Techniques*, 37 (2003), 39–44.

[114] MAN Diesel. Two-stroke Low Speed Diesel Engines. Tech. rep., 2009.

[115] Manin, Julien, Kastengren, Alan L., and Payri, Raúl. Understanding the acoustic oscillations observed in the injection rate of a common-rail direct injection diesel injector. *Journal of Engineering for Gas Turbines and Power 134*, 12 (Oct. 2012), 122801.

[116] Martinez, Lionel, Benkenida, Adlène, and Cuenot, Bénédicte. A model for the injection boundary conditions in the context of 3D simulation of diesel spray: methodology and validation. *Fuel 89*, 1 (Jan. 2010), 219–228.

[117] Martynov, Sergey. *Numerical Simulation of the Cavitation Process in Diesel Fuel Injectors*. Phd, University of Brighton, 2005.

[118] Ménard, T., Beau, Pierre-Arnaud, Tanguy, S., Demoulin, F.X., and Berlemont, A. Primary break-up: DNS of liquid jet to improve atomization modeling. *Computational methods in multiphase flows III* (2005), 343–352.

[119] Ménard, T., Tanguy, S., and Berlemont, a. Coupling level set/VOF/ghost fluid methods: validation and application to 3D simulation of the primary break-up of a liquid jet. *International Journal of Multiphase Flow 33*, 5 (May 2007), 510–524.

[120] Miranda, R, Chaves, H, and Obermeier, F. Cavitation in a transparent real size VCO injection nozzle. In *ICLASS 2003*.

[121] Moulai, Maryam, Grover, Ronald, Parrish, Scott, and Schmidt, David. Internal and near-nozzle flow in a multi-hole gasoline injector under flashing and non-flashing conditions.

[122] Naber, J., and Siebers, D. Effects of gas density and vaporization on penetration and dispersion of diesel sprays. *SAE Paper no. 960034* (1996).

[123] Nathan, G.J., Kalt, P.a.M., Alwahabi, Z.T., Dally, B.B., Medwell, P.R., and Chan, Q.N. Recent advances in the measurement of strongly radiating, turbulent reacting flows. *Progress in Energy and Combustion Science 38*, 1 (Feb. 2012), 41–61.

[124] Negro, S., and Bianchi, G. M. Superheated fuel injection modeling: an engineering approach. *International Journal of Thermal Sciences 50*, 8 (2011), 1460–1471.

[125] Neroorkar, K D, Gopalakrishnan, S, Schmidt, D P, and Grover, R O. Simulation of flash-boiling in pressure swirl injectors. In *ICLASS 2009, 11th Triennial International Conference on Liquid Atomization and Spray Systems*, (Vail, Colorado, 2009).

[126] Neroorkar, K.D., Mitcham, C.E., Plazas, A.H., Grover, R.O., and Schmidt, D.P. Simulations and analysis of fuel flow in an injector including transient needle effects. In *ILASS-Americas 24th Annual Conference on Liquid Atomization and Spray Systems* (San Antonia, TX, 2012), no. May.

[127] Neroorkar, Kshitij Deepak. *Modeling of Flash Boiling Flows in Injectors with Gasoline-Ethanol Fuel Blends*. Phd, University of Massachusetts - Amherst, 2011.

[128] Ning, Wei, Reitz, Rolf D., Diwakar, Ramachandra, and Lippert, Andreas M. An Eulerian-Lagrangian spray and atomization model with improved turbulence modeling. *Atomization and Sprays 19*, 8 (2009), 727–739.

[129] Ning, Wei, Reitz, Rolf D., Lippert, Andreas M., and Diwakar, Ramachandra. Development of a next-generation spray and atomization model using an Eulerian-Lagrangian methodology. In *International Multidimensional Engine Modeling Users Group Meeting* (Detroit, MI, 2007), no. April.

[130] Nourgaliev, R.R., and Theofanous, T.G. High-fidelity interface tracking in compressible flows: unlimited anchored adaptive level set. *Journal of Computational Physics 224*, 2 (June 2007), 836–866.

[131] Nurick, W. H. Orifice cavitation and its effect on spray mixing. *Journal of Fluids Engineering 98*, 4 (1976), 681–687.

[132] Olsson, Elin, and Kreiss, Gunilla. A conservative level set method for two phase flow. *Journal of Computational Physics 210*, 1 (Nov. 2005), 225–246.

[133] O'Rourke, Peter J. *Collective Drop Effects on Vaporizing Liquid Sprays*. Ph.d., Princeton University, 1981.

[134] O'Rourke, Peter J. The KIVA computer program for multidimensional chemically reactive fluid flows with fuel sprays. *Lecture Notes in Physics 241* (1985), 74–89.

[135] Oza, R.D., and Sinnamon, J.F. An experimental and analytical study of flash-boiling fuel injection. Tech. Rep. 830590, SAE, 1983.

[136] Paciaroni, M., and Linne, M. Single-shot two-dimensional ballistic imaging through scattering media. *Applied Optics 43*, 5100-9 (2004).

[137] Pai, Madhusudan G., and Subramaniam, Shankar. A comprehensive probability density function formalism for multiphase flows. *Journal of Fluid Mechanics 628* (June 2009), 181.

[138] Pandal, A., Pastor, J.M., García-Oliver, J.M., Baldwin, E., and Schmidt, D.P. A consistent, scalable model for Eulerian spray modeling. *International Journal of Multiphase Flow 83* (2016), 162–171.

[139] Parker, TE, Duran, S, and Porter, J. Ballistic imaging of sprays at diesel relevant conditions. In *ICLASS 2012, 12th Triennial International Conference on Liquid Atomization and Spray Systems* (Heidelberg, Germany, 2012).

[140] Parrish, Scott E., Zink, R. J., Sivathanu, Y., and Lim, J. Spray patternation of a multi-hole injector utilizing planar line-of-sight extinction tomography. In *ILASS Americas, 22nd Annual Conference on Liquid Atomization and Spray Systems* (2010).

[141] Pastor, José V., Javier López, J., García, José M., and Pastor, José M. A 1D model for the description of mixing-controlled inert diesel sprays. *Fuel 87*, 13-14 (2008), 2871–2885.

[142] Payri, F., Bermúdez, V., Payri, R., and Salvador, F.J. The influence of cavitation on the internal flow and the spray characteristics in diesel injection nozzles. *Fuel 83*, 4-5 (Mar. 2004), 419–431.

[143] Payri, R., Garcia, J., Salvador, F., and Gimeno, Jaime. Using spray momentum flux measurements to understand the influence of diesel nozzle geometry on spray characteristics. *Fuel 84*, 5 (Mar. 2005), 551–561.

[144] Payri, R, Gimeno, J, Cuisano, J, and Arco, J. Hydraulic characterization of diesel engine single-hole injectors. *Fuel 180* (2016), 357–366.

[145] Payri, R., Salvador, F. J., Gimeno, J., and Bracho, G. A new methodology for correcting the signal cumulative phenomenon on injection rate measurements. *Experimental Techniques 32*, 1 (2008), 46–49.

[146] Payri, R., Salvador, F.J., Gimeno, J., and Zapata, L.D. Diesel nozzle geometry influence on spray liquid-phase fuel penetration in evaporative conditions. *Fuel 87*, 7 (June 2008), 1165–1176.

[147] Payri, R., Salvador, F.J., Gimeno, Jaime, and Novella, R. Flow regime effects on non-cavitating injection nozzles over spray behavior. *International Journal of Heat and Fluid Flow 32*, 1 (Feb. 2011), 273–284.

[148] Pei, Yuanjiang, Davis, Michael J., Pickett, Lyle M., and Som, Sibendu. Engine Combustion Network (ECN): Global sensitivity analysis of Spray A for different combustion vessels. *Combustion and Flame 162*, 6 (2015), 2337–2347.

[149] Pickett, L., Manin, J., Kastengren, A., and Powell, C. Comparison of near-field structure and growth of a diesel spray using light-based optical microscopy and X-ray radiography. *SAE Int. J. Engines 7*, 2 (2014).

[150] POPE, S. B. An explanation of the turbulent round-jet/plane-jet anomaly. *AIAA Journal 16*, 3 (Mar. 1978), 279–281.

[151] Postrioti, Lucio, Bosi, Maurizio, Cavicchi, Andrea, AbuZahra, Fakhry, Gioia, Rita Di, and Bonandrini, Giovanni. Momentum flux measurement on single-hole GDI injector under flash-boiling condition. Tech. Rep. 2015-24-2480, SAE, 2015.

[152] Powell, C.F., Kastengren, A.L., Liu, Z., and Fezzaa, K. The effects of diesel injector needle motion on spray structure. *Journal of Engineering for Gas Turbines and Power 133*, 1 (2011), 012802–012802–9.

[153] Ramirez, A., Aggarwal, S., Kastengren, A., El-Hannouny, E., Longman, D.E., Powell, C.F., and Senecal, P.K. Development and validation of a primary breakup model for diesel engine applications. In *SAE 2009 World Congress & Exhibition* (2009).

[154] Reitz, R., and Bracco, F. *The Encyclopedia of Fluid Mechanics*. Gulf Publishing, Houston, TX, 1986.

[155] Reitz, Rolf D. Modeling atomization processes in high-pressure vaporizing sprays. *Atomization and Sprays 3* (1987), 309–337.

[156] Renardy, Y., and Renardy, M. PROST: a parabolic reconstruction of surface tension for the volume-of-fluid method. *Journal of Computational Physics 183* (2002), 400–21.

[157] Renault. The stratified charge engine. *http://www.renault.com/en/Innovation/eco-technologies/Documents_Without_Moderation/PDF%20ENV%20GB/Stratified-charge%20engine.pdf*.

[158] Roth, H., Gavaises, M., and Arcoumanis, C. Cavitation initiation, its development and link with flow turbulence in diesel injector nozzles. In *SAE 2002 World Congress & Exhibition* (2002).

[159] Rudolf, Pavel, Hudec, Martin, Zubík, Pavel, and Štefan, David. Experimental measurement and numerical modeling of cavitating flow in converging-diverging nozzle. In *EPJ Web of Conferences* (2012), vol. 25.

[160] Saha, Kaushik, Som, Sibendu, Battistoni, Michele, Li, Yanheng, Pomraning, Eric, and Senecal, P. K. Numerical investigation of two-Phase flow evolution of in- and near-nozzle regions of a gasoline direct injection engine during needle transients. *SAE International Journal of Engines 9*, 2 (2016), 2016–01–0870.

[161] Saha, Kaushik, Som, Sibendu, Battistoni, Michele, Li, Yanheng, Quan, S., and Senecal, P. K. Modeling of internal and near-nozzle flow for a GDI fuel injector. In *Proceedings of the ASME 2015 Internal Combustion Engine Division Fall Technical Conference* (2015).

[162] Salvador, Francisco Javier, Gimeno, Jaime, Pastor, José Manuel, and Martí-Aldaraví, Pedro. Effect of turbulence model and inlet boundary condition on the diesel spray behavior simulated by an Eulerian spray atomization (ESA) model. *International Journal of Multiphase Flow 65* (Oct. 2014), 108–116.

[163] Salvi, Joaquim, Fernandez, Sergio, Pribanic, Tomislav, and Llado, Xavier. A state of the art in structured light patterns for surface profilometry. *Pattern Recognition 43*, 8 (Aug. 2010), 2666–2680.

[164] Scardovelli, Ruben, and Zaleski, Stéphane. Direct numerical simulation of free-surface and interfacial flow. *Annual Review of Fluid Mechanics 31*, 1 (Jan. 1999), 567–603.

[165] Schmidt, David P. *Cavitation in diesel fuel injector nozzles by cavitation in diesel fuel injector nozzles*. Phd, University of Wisconsin, 1997.

[166] Schmidt, David P., Corradini, M. L., and Rutland, Christopher J. A two-dimensional, non-equilibrium model of flashing nozzle flow. In *Proceedings of the 3rd ASME/JSME Joint Fluids Engineering Conference* (San Francisco, California, July 1999).

[167] Schmidt, David P., Gopalakrishnan, S., and Jasak, H. Multi-dimensional simulation of thermal non-equilibrium channel flow. *International Journal of Multiphase Flow 36*, 4 (Apr. 2010), 284–292.

[168] Schmidt, J., Schaefer, Z., Meyer, T., Roy, S., Danczyk, S., and Gord, J. Ultrafast time-gated ballistic-photon imaging and shadowgraphy in optically rocket sprays. *Applied Optics 48*, 4 (2009), B137–44.

[169] Schwarz, Ch., Missy, S., Steyer, H., Durst, B., Schünemann, E., Kern, W., and Witt, A. The new BMW four and six-cylinder spark-ignition engines with stratified combustion. *MTZ 5* (2007), 68.

[170] Sedarsky, D., Gord, J., Meyer, T., and Linne, M. Fast-framing ballistic imaging of velocity in an aeraeted spray. *Optics Letters 34*, 18 (2009), 2748–2750.

[171] Sedarsky, M., Paciaroni, D., Linne, M., Gord, J., and Meyer, T. Velocity imaging at the fluid/gas interface of the liquid core in an atomizing spray. *Optics Letters 31*, 7 (2006), 906–908.

[172] Serras-Pereira, J., Van Romunde, Z., Aleiferis, P. G., Richardson, D., Wallace, S., and Cracknell, R. F. Cavitation, primary break-up and flash boiling of gasoline, iso-octane and n-pentane with a real-size optical direct-injection nozzle. *Fuel 89*, 9 (2010), 2592–2607.

[173] Sethian, J. a., and Smereka, Peter. Level set methods for fluid interfaces. *Annual Review of Fluid Mechanics 35*, 1 (Jan. 2003), 341–372.

[174] Shen, Q., Lee, W-K, Fezzaa, K., Chu, Y.S., De Carlo, F., Jemian, P., Ilavsky, J., Erdmann, M., and Long, G.G. Dedicated full-field X-ray imaging beamline at Advanced Photon Source. *Nuclear Instruments and Methods in Physics Research Section A: Accelerators, Spectrometers, Detectors and Associated Equipment 582*, 1 (2007), 77–79.

[175] Sher, Eran, Bar-Kohany, Tali, and Rashkovan, Alexander. Flash-boiling atomization. *Progress in Energy and Combustion Science 34*, 4 (2008), 417–439.

[176] Shi, Yu, and Reitz, Rolf D. Multi-dimensional modelling of diesel combustion: review. In *Modeling Diesel Combustion*, Mechanical Engineering Series. Springer Netherlands, Dordrecht, 2010, pp. 207–246.

[177] Shost, Mark A., Lai, Ming-Chia, Befrui, Bizhan, Spiekermann, Peter, and Varble, Daniel L. GDI nozzle parameter studies using LES and spray imaging methods. Tech. Rep. 2014-01-1434, SAE, 2014.

[178] Siebers, Dennis L. Liquid-phase fuel penetration in diesel sprays. *SAE Technical Paper* (1998).

[179] Siebers, Dennis L. Scaling liquid-phase fuel penetration in diesel sprays based on mixing-limited vaporization. *SAE Technical Paper* (1999).

[180] Som, S., Longman, D. E., Ramirez, A. I., and Aggarwal, S. K. A comparison of injector flow and spray characteristics of biodiesel with petrodiesel. *Fuel 89* (2010), 4014–4024.

[181] Sou, Akira, Ilham, Muhammad, Kenji, Maulana, Hosokawa, Shigeo, and Tomiyama, Akio. Effects of nozzle geometry on cavitation in nozzles of pressure atomizers. *Journal of Fluid Science and Technology 3*, 5 (2008), 622–632.

[182] Stahl, M., Gnir, M., Damaschke, N., and Tropea, C. Laser Doppler measurements of nozzle flow and optical characterization of the generated spray. In *ILASS-2005* (Orleans, France, 2005).

[183] Stahl, Martin, Damaschke, Nils, Tropea, Cameron, Gmbh, Robert Bosch, Platz, Robert Bosch, and Engineering, Electrical. Experimental investigation of turbulence and cavitation inside a pressure atomizer and optical characterization of the generated spray. In *ICLASS 2006* (Kyoto, Japan, 2006).

[184] Strek, Piotr, Schmidt, David, and Duke, Daniel. X-ray radiography and CFD studies of the spray G injector. In *SAE 2016 World Congress & Exhibition* (Detroit, MI, 2016).

[185] Subramaniam, Shankar. LagrangianEulerian methods for multiphase flows. *Progress in Energy and Combustion Science 39*, 2-3 (Apr. 2013), 215–245.

[186] Suh, Hyun Kyu, and Lee, Chang Sik. Effect of cavitation in nozzle orifice on the diesel fuel atomization characteristics. *International Journal of Heat and Fluid Flow 29*, 4 (Aug. 2008), 1001–1009.

[187] Sussman, M., Smith, K.M., Hussaini, M.Y., Ohta, M., and Zhi-Wei, R. A sharp interface method for incompressible two-phase flows. *Journal of Computational Physics 221*, 2 (Feb. 2007), 469–505.

[188] Sussman, Mark. A second order coupled level set and volume-of-fluid method for computing growth and collapse of vapor bubbles. *Journal of Computational Physics 187*, 1 (May 2003), 110–136.

[189] Suzzi, D. *Diesel Nozzle Flow and Spray Formation: Coupled Simulations with Real Engine Validation*. PhD thesis, Universität Stuttgart, 2009.

[190] Takaishi, T., Numata, A., Nakano, R., and Sakaguchi, K. Approach to high efficiency diesel and gas engines. *Mitsubishi Heavy Induesties, Ltd. Technical Review 45*, 1 (2008).

[191] Tillou, J., Michel, J.-B., Angelberger, C., Bekdemir, C., and Veynante, D. Large-eddy simulation of diesel spray combustion with exhaust gas recirculation. *Oil & Gas Science and Technology Revue dIFP Energies nouvelles 69*, 1 (Nov. 2013), 155–165.

[192] Trask, Nathaniel, Schmidt, David P., Lightfoot, Malissa, and Danczyk, Stephen. Compressible modeling of the internal flow in a gas-centered swirl-coaxial fuel injector. *Journal of Propulstion and Power 28*, 4 (2012).

[193] Tryggvason, G., Bunner, B., Esmaeeli, a., Juric, D., Al-Rawahi, N., Al., Et, Tauber, W., Han, J., Nas, S., and Jan, Y.-J. A front-tracking method for the computations of multiphase flow. *Journal of Computational Physics 169*, 2 (May 2001), 708–59.

[194] Unverdi, SO, and Tryggvason, G. A front-tracking method for viscous, incompressible, multi-fluid flows. *Journal of Computational Physics 100* (1992), 25–37.

[195] U.S. Energy Information Agency. International Energy Outlook, 2013.

[196] Vallet, A., Burluka, A. A., and Borghi, R. Development of a Eulerian model for the "atomization" of a liquid jet. *Atomization and Sprays 11* (2001), 619–642.

[197] Vallet, Ariane, and Borghi, Roland. Modélisation eulerienne de l'atomisation d'un jet liquide. *Comptes Rendus de l'Académie des Sciences - Series IIB - Mechanics-Physics-Astronomy 327*, 10 (Sept. 1999), 1015–1020.

[198] Van Romunde, Z., and Aleiferis, P.G. Effect of operating conditions and fuel volatility on development and variability of sprays from gasoline direct-injection multihole injectors. *Atomization and Sprays 19*, 3 (2009), 207–234.

[199] Viera, J.P., Payri, R., Swantek, A.B., Duke, D.J., Sovis, N., Kastengren, A.L., and Powell, C.F. Linking instantaneous rate of injection to X-ray needle lift measurements for a direct-acting piezoelectric injector. *Energy Conversion and Management 112*, C (2016), 350–358.

[200] Villermaux, Emmanuel, and Bossa, Benjamin. Single-drop fragmentation determines size distribution of raindrops. *Nature Physics 5*, 9 (July 2009), 697–702.

[201] Villiers, E., Gosman, AD, and Weller, HG. Large eddy simulation of primary diesel spray atomization. *SAE Tech. Pap. 2004-01-0100* (2004).

[202] Wang, Y., Liu, X., Im, K-S, Lee, WK, Wang, J., Fezzaa, K., and Al., Et. Ultrafast x-ray study of dense-liquid-jet flow dynamics using structure-tracking velocimetry. *Nature Physics 4* (2008), 305–9.

[203] Wang, YJ, Im, K-S, Fezzaa, K., Lee, WK, Wang, J, Micheli, P, and Al., Et. Quantitative x-ray phase contrast imaging of air-assisted water sprays with high weber numbers. *Applied Physics Letters 89* (2006).

[204] Warsi, Z.U.A. *Fluid Dynamics: Theoretical and Computational Approaches*, 3rd ed. CRC Press, 2005.

[205] Webster, L. The future of diesel in the US: analysis. *Popular Mechanics* (Sept. 2009).

[206] Wilcox, David C. *Basic Fluid Mechanics*, 4th ed. DCW Industries, Inc., 2010.

[207] Williams, F. A. Spray combustion and atomization. *Physics of Fluids 1*, 6 (Nov. 1958), 541.

[208] Xu, Min, Zhang, Yuyin, Zeng, Wei, Zhang, Gaoming, and Zhang, Ming. Flash boiling: easy and better way to generate ideal sprays than the high injection pressure. *SAE Int. J. Fuels Lubr. 6*, 1 (2013), 137–148.

[209] Xue, Q., Battistoni, M., Powell, C.F., Longman, D.E., Quan, S.P., Pomraning, E., Senecal, P.K., Schmidt, D.P., and Som, S. An Eulerian CFD model and X-ray radiography for coupled nozzle flow and spray in internal combustion engines. *International Journal of Multiphase Flow 70* (2015), 77–88.

[210] Xue, Qingluan, Battistoni, Michele, Som, Sibendu, Quan, Shaoping, Senecal, P. K., Pomraning, Eric, and Schmidt, David P. Eulerian CFD modeling of coupled nozzle flow and spray with validation against X-ray radiography data. *SAE International Journal of Engines 7*, 2 (Apr. 2014).

[211] Zeng, Wei, Xu, Min, Zhang, Gaoming, Zhang, Yuyin, and Cleary, David J. Atomization and vaporization for flash-boiling multi-hole sprays with alcohol fuels. *Fuel 95* (2012), 287–297.

[212] Zeng, Wei, Xu, Min, Zhang, Ming, Zhang, Yuyin, and Cleary, David J. Macroscopic characteristics for direct-injection multi-hole sprays using dimensionless analysis. *Experimental Thermal and Fluid Science 40* (2012), 81–92.

[213] Zhang, Gaomimg, Xu, Min, Zhang, Yuyin, Zhang, Ming, and Cleary, David J. Macroscopic characterization of flash-boiling multihole sprays using planar laser-induced exciplex fluorescence. part II: cross-sectional spray structure. *Atomization and Sprays 23*, 3 (2013), 265–278.

[214] Zhang, Ming, Drake, Michael C., and Peterson, Kevin. Simultaneous high-speed imaging of fuel spray, combustion luminosity, and soot luminosity in a spray-guided direct injection engine with different multi-hole fuel injectors. In *Proceedings of the ASME 2013 Internal Combustion Engine Division Fall Technical Conference* (Dearborn, Michigan, 2013).

[215] Zhao, Hongwu, Quan, Shaoping, Dai, Meizhong, Pomraning, Eric, Senecal, P. K., Xue, Qingluan, Battistoni, Michele, and Som, Sibendu. Validation of a three-dimensional internal nozzle flow model including automatic mesh generation and cavitation effects. *Journal of Engineering for Gas Turbines and Power 136*, 9 (Apr. 2014), 092603.